A QUANTITATIVE INVESTIGATION OF THE SOLAR MODULATION

OF COSMIC-RAY PROTONS AND HELIUM NUCLEI

Thesis by

Thomas Lee Garrard

In Partial Fulfillment of the Requirements

for the Degree of

Doctor of Philosophy

California Institute of Technology

Pasadena, California

1973

(Submitted June 19, 1972)

ii

ACKNOWLEDGMENT

My desire to express my gratitude to my advisor, Professor Rochus Vogt, far exceeds my meager prose ability. His technical support has been invaluable and his moral support is greatly appreciated. I can only say that I am very thankful for his guidance.

I have benefited greatly from the advice of Professor Edward Stone and I am please to acknowledge my debt to him.

Professors Stone and Vogt designed and constructed the pαe and OGO-6 instruments, with the assistance of Peter Wenzel and Steve Murray. This thesis would not have been possible without their work.

My fellow graduate students and friends, John Lupton and Alan Cummings, have contributed substantially to this thesis. I am very grateful for their aid.

Professors J. R. Jokipii and J. A. Earl (visiting Caltech from the University of Maryland) have been extremely helpful, as will be obvious to anyone familiar with the study of solar modulation.

I appreciate greatly the aid and advice of Dr. John Fanselow and of Gordon Hurford, James Brown, and Lawrence Evans - fellow graduate students.

William Althouse served as electronic engineer for the OGO-6 and pαe systems and William Blodgett for the accelerator telescope. Their very compentent work has been indispensable.

Special thanks go to Dr. R. Siegel at the Space Radiation Effects Laboratory and Mr. J. Vale and Mr. L. Hauser at the Lawrence Radiation Laboratory for their aid in the accelerator calibrations.

iii

To Toni Michele and her parents and grandparents

ABSTRACT

The differential energy spectra of cosmic-ray protons and He nuclei have been measured at energies up to 315 MeV/nucleon using balloon- and satellite-borne instruments. These spectra are presented for solar quiet times for the years 1966 through 1970. The data analysis is verified by extensive accelerator calibrations of the detector systems and by calculations and measurements of the production of secondary protons in the atmosphere.

The spectra of protons and He nuclei in this energy range are dominated by the solar modulation of the local interstellar spectra. The transport equation governing this process includes as parameters the solar-wind velocity, V, and a diffusion coefficient, $K(r,R)$, which is assumed to be a scalar function of heliocentric radius, r, and magnetic rigidity, R. The interstellar spectra, j_D, enter as boundary conditions on the solutions to the transport equation. Solutions to the transport equation have been calculated for a broad range of assumed values for $K(r,R)$ and j_D and have been compared with the measured spectra.

It is found that the solutions may be characterized in terms of a dimensionless parameter,

$$\psi(r,R) = \int_r^\infty \frac{V\, dr'}{K(r',R)} \ .$$

The amount of modulation is roughly proportional to ψ. At high energies or far from the Sun, where the modulation is weak, the solution is

determined primarily by the value of ψ (and the interstellar spectrum) and is not sensitive to the radial dependence of the diffusion coefficient. At low energies and for small r, where the effects of adiabatic deceleration are found to be large, the spectra are largely determined by the radial dependence of the diffusion coefficient and are not very sensitive to the magnitude of ψ or to the interstellar spectra. This lack of sensitivity to j_D implies that the shape of the spectra at Earth cannot be used to determine the interstellar intensities at low energies.

Values of ψ determined from electron data were used to calculate the spectra of protons and He nuclei near Earth. Interstellar spectra of the form $j_D \propto (W - 0.25m)^{-2.65}$ for both protons and He nuclei were found to yield the best fits to the measured spectra for these values of ψ, where W is the total energy and m is the rest energy. A simple model for the diffusion coefficient was used in which the radial and rigidity dependence are separable and κ is independent of radius inside a modulation region which has a boundary at a distance D. Good agreement was found between the measured and calculated spectra for the years 1965 through 1968, using typical boundary distances of 2.7 and 6.1 A.U. The proton spectra observed in 1969 and 1970 were flatter than in previous years. This flattening could be explained in part by an increase in D, but also seemed to require that a noticeable fraction of the observed protons at energies as high at 50 to 100 MeV be attributed to quiet-time solar emission. The turnup in the spectra at low energies observed in all years was also attributed to solar emission. The diffusion coefficient used to fit the 1965 *spectra is in*

reasonable agreement with that determined from the power spectra of the interplanetary magnetic field (Jokipii and Coleman, 1968). We find a factor of roughly 3 increase in ψ from 1965 to 1970, corresponding to the roughly order of magnitude decrease in the proton intensity at 250 MeV. The change in ψ might be attributed to a decrease in the diffusion coefficient, or, if the diffusion coefficient is essentially unchanged over that period (Mathews et al., 1971), might be attributed to an increase in the boundary distance, D.

viii

TABLE OF CONTENTS

LIST OF FIGURES

LIST OF TABLES

I. INTRODUCTION

The quantitative study of the effects of the interplanetary medium on the spectra of cosmic rays in their passage from interstellar space to the Earth is of great importance. Such a study can provide information on two very interesting subjects: the local interstellar spectra and the interplanetary medium.

The interstellar cosmic-ray spectra provide one of the most useful means of quantitatively testing models of astrophysical particle acceleration mechanisms, they provide direct material samples of astrophysical objects (e.g., supernovae, pulsars, etc.), and they carry information on the physical properties of the interstellar medium.

In penetrating the interplanetary medium the galactic cosmic rays serve as sensitive probes of this medium, thus allowing a study of the sphere of influence of a star, the Sun. In addition to its intimate connection with solar physics, the interplanetary medium is a very interesting example of a collisionless plasma and it is the plasma-like properties of this medium which lead to the modulation of the galactic cosmic rays.

The modulation of cosmic rays by the interplanetary medium is quantitatively determined by a transport equation. The physical model (Parker, 1963) upon which this equation is based represents the solar system as being filled with an expanding, fully ionized, and highly conducting plasma, the solar wind, which contains frozen-in, irregular magnetic fields. Cosmic rays are scattered from these irregularities

and execute a random walk in the solar wind. The particles are con-
vected outwards by the flow of the solar wind, diffuse inwards, and
are decelerated by the adiabatic cooling associated with the expansion
of the solar wind. The parameters required to define the transport
equation and its solution are the diffusion tensor, $\overline{\overline{\kappa}}$, which is
generally a function of radius and energy, the solar wind velocity, and
the interstellar energy spectrum, $j_D(T)$. The solar wind velocity has
been measured by a number of investigators over a considerable time
span (Gosling et al., 1971) and is reasonably well known. Jokipii
(1966, 1967, 1968) has shown that the diffusion coefficient may be
determined from measurements of the power spectra of the temporal
fluctuations in the magnetic field observed at a point in space, and
diffusion coefficients have been calculated from such measurements.
However, the so-far, limited scope of space exploration has not yet
allowed in situ measurements over sufficiently large regions of
frequency (energy), radius, or time to completely determine this
parameter.

A further problem lies in the fact that it has not been
possible to find an analytic solution to the transport equation for
reasonably realistic forms of the diffusion coefficient, $\kappa(r,T)$.
Several analytic approximations exist but it is difficult to judge to
what extent these approximations are valid.

In this thesis, we present numerical solutions of the transport
equation which have been calculated for a wide range of parameters. By
comparing the numerical and analytic solutions, we are able to set limits,
within which a given approximation is useful and outside of which it

breaks down.

We also present measurements made of the energy spectra of protons and He nuclei for each of the years 1966 through 1970, a significant fraction of the current solar cycle. These spectra were measured with instruments whose accuracy and reliability represent a considerable improvement over previous investigations. This improvement is due to extensive calibrations with particle accelerators and the first unambiguous measurements ever made of atmospheric secondary production. We make use of these spectra and the numerical solutions to the transport equation to place limits on the relations between the parameters, $\bar{\bar{\kappa}}$ and j_D, and to infer the radial and energy dependence of $\bar{\bar{\kappa}}$.

II. INSTRUMENT

The observations to be described in this thesis were made with two detector systems, which are physically very similar to each other. One instrument, the pαe system, was flown on high-altitude balloons; the other was on the OGO-6 satellite and will be referred to as the OGO-6 system. These instruments have been previously described (Althouse et al., 1967; Wenzel, 1968; Murray, 1970; Lupton, 1971) and their properties are briefly summarized here for the sake of completeness. The instrument which we shall discuss is the pαe instrument; some differences between it and the OGO-6 instrument are noted in section D of this chapter.

Each instrument includes two separate particle detectors, the "range telescope" and the "Čerenkov telescope." The range telescope (see section A) performs energy-loss and range measurements on charged particles. These measurements are used to determine the differential energy spectra of protons and He nuclei from about 1 to 315 MeV/nucleon and their integral fluxes above 315 MeV/nucleon. The Čerenkov telescope makes energy-loss and Čerenkov-radiation measurements which are used to determine integral intensities of protons and He nuclei above 400 MeV/nucleon. Both telescopes are sensitive to electrons and other charged particles as well as protons and He nuclei; however, in this work we are concerned only with protons and He nuclei and treat other particles as background.

A. The pαe Range Telescope

A cross section of the range telescope is shown in Figure II-1.
It consists of a stack of seven solid-state detectors, D1 through D7,
separated by absorbers, A2 - A6, and enclosed in a guard counter, D8. The
energy loss is measured in D1, D2, and D3 using 256-channel pulse-height
analyzers and in the range detectors, D4 - D7, using a multilevel discrim-
inator system which has only three possible states and therefore much
less resolution. The range of an incident particle is determined by
the number of detectors which are penetrated by the particle. D8 is
used in active anticoincidence to reject particles with trajectories
which leave or enter the side of the stack. Figure II-2 shows the
nominal response to protons and alpha particles. The average energy
loss in D1, D2, and D3 is plotted as a function of incident energy; and
the average energy necessary to reach each of the range detectors is
indicated.

D1 is a totally depleted silicon surface-barrier detector with
a thickness of 100μ and a diameter of 1.86 cm. The threshold of the D1
discriminator is set to trigger only if a particle has an energy loss
of more than 400 keV. Low-energy protons may have an energy loss of
several MeV in D1, while electrons with kinetic energies of more than
400 keV, which are relativistic and near minimum ionizing, will penetrate
D1 with an energy loss typically < 200 keV. Thus low-energy protons
can be easily distinguished from electrons.

D2 through D7 are lithium-drifted silicon detectors of about
1000μ depletion depth at 40V bias and a diameter of about 2.3 cm.
Absorber A2 is made of aluminum; A3 through A6 are made of a tungsten

alloy (Mallory 2000, $\rho = 18$ gm/cm^3). The absorber thicknesses are shown in Figure II-1. The absorber diameter is 2.41 cm.

D8 is 1 cm thick and made of NE-102 plastic scintillator material. It is housed in a thin-walled aluminum can which is painted white on the inside and is viewed by an RCA 4439 photomultiplier tube. The energy loss resolution of D8 is not critical since it serves only anticoincidence purposes. The discriminator threshold was set so that any charged particle penetrating more than about 3 mm of the scintillator at any point would give sufficient light to trigger the anticoincidence signal.

B. The pxe Čerenkov Telescope

This system, illustrated in Figure II-3, consists of two solid
state detectors, D1' and D2', in which we measure energy loss, and a
quartz Čerenkov radiator viewed by an EMI 9647QNB photomultiplier tube,
D3', with a guard counter, D4'. The quartz radiator is the window of
the phototube, thus guaranteeing good optical coupling. The upper
surface of the quartz is painted black so that a large fraction of the
light produced by backward moving particles is absorbed.

Figure II-4 shows the average energy loss of nuclei with $Z \leq 8$
in 1000μ of silicon plotted against their relative light output in
quartz. By using a bi-linear amplifier, we are able to resolve nuclei
up to oxygen. There is no Čerenkov light emitted by particles with
velocity less than $v = c/n$, where n is the index of refraction of quartz.
This velocity corresponds to an energy of about 350 MeV for protons.
The discriminator threshold is set at a level corresponding to 400-MeV
protons.

D1' and D2' are lithium-drifted silicon detectors similar to
D2 and D3. They are matched to each other and the associated amplifiers
are adjusted so that the average response of the two detector-amplifier
systems are equal. Only the smaller of the two signals is analyzed.
This selection helps to reduce the statistical fluctuations in the energy
loss (see Chapter IV).

C. The pαe Electronics

A simplified block diagram of the pαe electronic logic system is shown in Figure II-5. Each of the detectors is connected to an amplifier and a discriminator. The discriminators on the range detectors are composed of a low discriminator and a high discriminator. The discrimination thresholds are set so that the low discriminators will trigger on any charged particle which penetrates the detectors while the high discriminators will fire only for protons which have an energy of less than ~300 MeV at the top of the detector stack (or any particle with $Z > 1$). This feature aids in distinguishing electrons, muons, and interacting protons (see Appendix 1). The electronic logic uses the discriminator signals to decide if there is a valid event; and if so, which analog signals should be pulse height analyzed. The requirements for various events and the analyzed signals are listed in Table II-1. B is the "busy signal" which indicates the logic is occupied. After each event 210 msec are required to write the data onto magnetic tape; the busy signal blocks analysis of new events during this period.

Rate scalers count the number of $D2D3\overline{D8}$, $D1'D2'D3'\overline{D4'}$, D8, and D4' events. The rate scaling proceeds without regard to the busy signal and, hence, with negligible dead time (the discriminator-rate-scaler-system dead time is ~100 μsec; event rates are typically less than 10 events per second).

Figure II-6 shows the data word which is written on a (16 channel) magnetic tape for each analyzed event. PHA1 and PHA2 are the pulse heights of the two analyzed signals. The indicator bits and the range bits show which detectors fired and hence, which analog signals

were analyzed. The rate bits indicate the state of the highest-order bit of each of the four rate scalers. A particular scaler has counted a number of events equal to half its maximum capacity each time its rate bit changes. The average rate is determined by dividing that number by the time between bit changes. In addition to the data shown in Figure II-5, we also record time and temperature. The time signal is derived from an Accutron clock with a one minute period and is counted by a 4-bit scaler.

Signals Required for Analysis	Pulse-Height-Analyzed Signals
D1 $\overline{\overline{D8}}$ $\overline{B}$	D1, D2
$\overline{\overline{D1}}$ D2 D3 $\overline{\overline{D8}}$ $\overline{B}$	D2, D3
D1' D2' D3' $\overline{\overline{D4'}}$ $\overline{B}$ D1' > D2'	D2', D3'
D1' D2' D3' $\overline{\overline{D4'}}$ $\overline{B}$ D1' < D2'	D1', D3'

Table II-1 Requirements for analysis of an event and the analyzed sig-
nals. The "bar" implies logical complement.

D. The OGO-6 Instrument

This instrument has been described in previous reports (Althouse et al., 1967; Murray, 1970; Lupton, 1971). We mention here those differences from pαe which influence the data analysis.

OGO-6 has a third pulse-height analyzer. If the range detectors are not triggered, we record three pulse heights (D1, D2, and D3 or D1', D2', and D3'). If the range detectors are triggered, the D2 and D3 pulse heights are recorded.

OGO-6 readout is synchronous. The experiment returns a data word at fixed intervals with a flag bit to indicate whether it is a new event or a redundant readout of an old event. Synchronous readout means that the time is known with a resolution of a few milliseconds. The normal readout rate is about 7 events per second so that the dead time is slightly less than pαe.

There are 20 rates which are scaled, including $D2D3\overline{D8}$ and $D1'D2'D3'\overline{D4}'$ which are used to calculate the dead time correction.

All of the solid-state detectors in OGO-6 were surface-barrier detectors. The surface-barrier detectors have much smaller dead layers than the lithium-drifted detectors in pαe, which simplifies measurements of low-energy particles. (The low-energy particles seen by pαe are almost entirely atmospheric secondaries so that the dead-layer problem is not important.) There were also small variations in the diameters and thicknesses of the detectors between OGO-6 and pαe.

The D2 and D3 pulse-height analyzers in pαe and OGO-6 differed in resolution and dynamic range. The D2 and D3 analyzers in pαe had 256 channels with channel widths of about 33 keV; the channel width

of the OGO-6 analyzers was about 50 keV. The larger channel width of the OGO-6 analyzers allowed them to digitize the large energy losses of the low-energy protons without saturating at as low a level as the pαe pulse-height analyzers.

III. OBSERVATIONS

The criteria used in selecting the data for analysis are quite different for pαe and OGO-6.

Since the OGO-6 satellite was in a polar orbit within the Earth's magnetosphere, the OGO-6 data are selected on the basis of latitude, local time, etc., to ensure that we measure the interplanetary particle spectra, not that of geomagnetically trapped particles. Selection was also done on the basis of solar activity.

The pαe data discussed in this work were obtained from balloon flights made from Fort Churchill, Manitoba. A maximum pressure altitude of about 2-3 millibars (equivalent to ~2 gm/cm^2 residual atmosphere) was typical. Because of the problems of energy loss, absorption of primaries in the atmosphere, and the production of secondaries in the atmosphere, pαe proton spectra below 60 MeV are not presented in this work. This energy corresponds to a rigidity of 350 MV and it is clear (Isreal and Vogt, 1969; Fanselow and Stone, 1972) that at these rigidities we have access to the interplanetary spectra and need not concern ourselves with geomagnetic effects. It is also clear that the effects of the atmosphere on the spectra must be carefully considered.

A. Balloon Flights

A photobarograph was flown with the pɑe balloon gondola in order to determine atmospheric pressure and, hence, the amount of residual atmosphere above the experiment. The photobarograph consists of a camera system and a barometer, thermometer, and clock. A photograph is taken of these instruments at regular intervals to record the pressure and temperature as a function of time. These data allow us to construct an altitude curve -- a typical example is shown in Figure III-1. On the basis of this curve the flight is broken up into one or more "float" periods and several "ascent" periods. Ascent periods are chosen by a compromise between altitude resolution and counting statistics. An ascent period is typically ~10 minutes, very short compared to a typical float period of 10 hours. For this reason, data from all the ascent periods at a given altitude during one series of balloon flights (typically spread over a month's time) are added together in order to reduce statistical fluctuations.

Figure III-2 illustrates the large changes in counting rates due to changes in altitude. The rate of D2D3$\overline{\text{D8}}$ events, which are primarily due to protons of greater than 18 MeV kinetic energy, is plotted as a function of time and, hence, altitude (see again Figure III-1). The large excursions in the counting rates plotted in Figure III-2 emphasize the importance of correcting the data for atmospheric effects.

Table III-1 is a list of all the balloon flights pertinent to this thesis. All of these flights were made with the telescopes pointed upwards to observe the flux of particles impinging upon the Earth from interplanetary space.

Caltech Flight Number	Date of Launch	Length of Float Period (10^4 sec)	Nominal Altitude of Float (gm/cm^2)	Mt. Washington Neutron Monitor Counting Rate
66C2P	6/27/66	2.57	2.0	2366
66C4P	7/11/66	3.45	2.2	2355
66C5P	7/15/66	4.87	2.0	2368
67C1P	6/17/67	3.22	1.7	2280
67C3P	7/2/67	5.33	2.5	2262
68C1P	6/24/68	3.75	2.1	2194
68C2P	7/5/68	3.15	2.0	2232
69C1P	6/15/69	2.98	2.8	2043
69C2P	6/18/69	3.48	2.0	2053
69C3P	6/21/69	3.15	1.9	2087
69C5P	7/1/69	4.00	3.4	2110
70C1P	6/22/70	3.21	2.0	2076

Table III-1

List of pertinent balloon flights. The length of the float period and the altitude are nominal quantities, since the float period was often divided into smaller segments during which variations in the altitude were small compared to the variations over the entire float period. The quoted neutron monitor rate is an average over the entire float period and was calculated from hourly averages kindly supplied by Dr. J. A. Lockwood.

B. Satellite Data

The OGO-6 satellite is a polar orbiter which was launched on
5 June 1969 into an orbit with perigee height of 397 km, apogee height
of 1098 km, inclination of 82 degrees, and period of 99.8 minutes (OGO
Bulletin, 1969). The "Caltech Solar and Galactic Cosmic-Ray Experiment"
is mounted so that the telescopes always face radially away from the
Earth. In January of 1970 the mylar window which shielded the range
telescope from sunlight failed and detector D1, at the top of the tele-
scope, was commanded off. In August of 1970 the satellite's tape
recorder failed, essentially terminating the mission.

Figure III-3 is a plot of OGO-6 counting rates of several
different types of events as a function of time during one orbit, with
supplementary orbit data. These plots are routinely generated for all
OGO-6 data and contain curves not of interest here. We are primarily
concerned with the curves labeled D18 (D1$\overline{\text{D8}}$), D128 (D1D2$\overline{\text{D8}}$), D28
(D2$\overline{\text{D8}}$), D238 (D2D3$\overline{\text{D8}}$), and ILAT (invariant latitude). These events
represent, respectively, (roughly speaking) protons of 1 - 20 MeV,
protons of 3 - 20 MeV, protons of > 1 MeV + electrons of > .15 MeV,
and protons of > 18 MeV + electrons of $\gtrsim$ 1 MeV. All the data analyzed
to give the spectra presented later in this thesis are taken from
periods when the invariant latitude of the satellite was > 70° and the
aforementioned rate curves indicated that the satellite had left the
trapped-particle zones and was inside the geomagnetic cutoff region
for the low-energy protons (D1$\overline{\text{D8}}$ events). Data were also excluded if
the electron rate (D2$\overline{\text{D8}}$) was more than about one order of magnitude
higher than "normal" for that day in order to minimize the effect of any

slight contamination of proton fluxes by electrons.

IV. DATA ANALYSIS

We use very similar methods of data analysis for both pɑe and OGO-6. In each case we abstract the data and prepare a magnetic tape which contains the data in a format appropriate to a FORTRAN program. All further analysis is done using these tapes.

The rate-scaler data are converted to rates in order to make dead time corrections and are plotted as a function of time to aid in the process of selecting data for further analysis. The event-type and pulse-height data are used to identify (at least roughly) the species and energy of the particle which caused the event. See Table A1-1. The number of events corresponding to a given species and a given energy can be used to determine the intensity of particles of that species and energy.

A. Calculation of Spectra from Range-Telescope Data

When the data have been selected as described in the previous chapter, the event-type and pulse-height data are used to assign range telescope events to various "bins".[*] The number of counts in these bins is converted to a flux by multiplying by the inverse of a response matrix which is derived in Appendix 1 from theoretical calculation and accelerator calibrations.

The particle spectra are derived using the relation:

$$\vec{j} = \frac{\overline{\overline{R}}^{-1} \cdot \vec{N}}{\tau} \quad . \qquad (IV-1)$$

The variables in this equation will be identified and discussed briefly in this chapter and in more detail in Appendix 1. The vector $\vec{j}$ has components j_n where j_n is the particle intensity in the n'th energy interval which is centered at E_n and has a width ΔE_n. $\vec{N}$ has components, N_i, which are the number of counts in the i'th bin in a time τ. τ is the effective time, corrected for dead time and data loss. The response maxtrix $\overline{\overline{R}}$ involves the geometrical factor,[+] G, and the width of the

---

[*]An event is said to fall into a bin if it meets a set of criteria involving range, as determined by the discriminators of D1-D7, energy loss in D1, D2, and D3, and energy loss in D4-D7 as determined by the high discriminators.

[+]The geometrical factor G is used to normalize the count rate to unit area and unit solid angle. It is given by

$$G = \iint dA \, d\Omega$$

where dA is an element of detector area, projected in the direction of Ω, and $d\Omega$ is an element of solid angle. The limits of integration are determined by the coincidence requirements of the telescope and may be quite complicated (Sullivan, 1971).

energy interval, ΔE. It also takes into account statistical fluctua-
tions in energy loss and nuclear interactions in the absorbers, which
may cause a "false" range measurement.

The off-diagonal elements of $\bar{\bar{R}}$ are caused by the energy-loss
fluctuations and nuclear interactions. If these effects were negli-
gible $\bar{\bar{R}}$ would be diagonal and the diagonal elements would be given
simply by

$$R_{ii} = G_i \ \Delta E_i$$

In this case equation IV-1 would reduce to

$$j_i = \frac{N_i}{G_i \ \Delta E_i \ \tau} \qquad . \qquad \text{(IV-2)}$$

The evaluation of $\bar{\bar{R}}$ including the effects of energy-loss
fluctuations and nuclear interactions is complicated, but the process
has been carefully verified by extensive calibrations. The complexity
is due to the use of all the data available for an event, i.e., high-
resolution measurements of energy loss in D2 and D3 (and D1 for low-
energy events), range, and the high discriminators in D4 - D7. However,
by using all of this information, we are able to reduce the effects of
energy-loss fluctuations and use the energy-loss data to distinguish
interacting particles from particles which stop due to ionization
energy loss. Thus the non-diagonal elements of $\bar{\bar{R}}$ are small ($\overset{<}{\sim} 10\%$ of
the diagonal elements) and, by virtue of our extensive calibrations,
well known.

B. Calculation of Spectra from Čerenkov-Telescope Data

The Čerenkov-telescope data were assigned to bins on the basis
of light output in D3' and energy loss, as given by the lesser of the
pulse heights from D1' and D2'. The selection of the lesser of D1' and
D2' had the effect of eliminating a large part of the statistical
fluctuations in which the energy loss is much larger than average, thus
improving the resolution. With our resolution, particles of different
Z are clearly distinguished. Electrons and protons are not distinguished,
and about 10% of the $Z = 1$ events in polar data are due to electrons.
The bins for $Z = 1$ and $Z = 2$ particles were determined from flight data
for 1967 and were large enough to contain essentially all of the
appropriate particles.

No attempt was made in this work to unfold a differential
energy spectrum from the Čerenkov-telescope response. Integral fluxes
above 400 MeV/nucleon were determined for helium nuclei using the bins
mentioned above. The fact that the integral fluxes measured with the
Čerenkov telescope agree with those measured with the range telescope
gives additional confirmation to the interaction corrections described
in the preceding section and the appendices.

C. Corrections to the Proton Spectra for Atmospheric Effects

The flux of atmospheric secondary protons was calculated by a Monte Carlo program based on the interaction cross-sections given by Bertini and others (Alsmiller and Barish, 1968; Bertini, 1963; Bertini, 1966; Bertini, 1967; Bertini, 1969; Bertini and Guthrie, 1970) and was fit to the measured curves of proton intensity versus altitude for 1969, which included a point at the top of the atmosphere determined from the OGO-6 data. These calculations are described in more detail in Appendix 2. The simultaneous measurements, made in 1969 and 1970 in and above the atmosphere, represent the most extensive measurements of atmospheric secondaries made to date and enable us to place confidence in our calculated secondaries for the 1966-1968 data.

The first step in correcting the 1966-1968 proton data for atmospheric effects was to subtract the calculated intensity of secondary protons from the measured intensity to get the intensity of residual primaries at float altitude. These primary intensities were then multiplied by a factor which took into account attenuation of primaries by contraction of the energy interval due to energy loss in the atmosphere and by nuclear interactions in the atmosphere. The energy intervals given in the following chapter are energies at the top of the atmosphere.

D. Corrections to the Spectra of Helium Nuclei for Atmospheric Effects

There are not enough cross-section data available to allow a meaningful calculation of the production of secondary He nuclei by cosmic rays in the atmosphere. We do, however, have spectral measurements made both in and above the atmosphere. We shall present a simple model which allows us to use these measurements to justify our treatment of the spectra of He nuclei measured with $p\alpha e$.

The production of secondary He nuclei in the atmosphere may be analyzed in terms of two distinct but related processes: the fragmentation of heavy cosmic-ray nuclei ($Z > 2$) in interactions with air nuclei, and the release of He nuclei in the breakup of air nuclei in interactions with cosmic rays (both protons and heavier nuclei).

In either of these processes the He nucleus may be thought of as existing in the heavier nucleus before the interaction. It is released or fragmented from this heavier nucleus by the interaction. In either process it is unlikely that the He nucleus will change its velocity by a large amount since this would, in most cases, produce a breakup of the He nucleus itself. In the fragmentation process the He nucleus will, on the average, be produced with the same vector velocity as the heavy nucleus which was fragmented. In the release of He nuclei from the breakup of air nuclei, the He nucleus will tend to have small velocity or small energy, i.e., the spectrum of these nuclei will fall rapidly with increasing energy.

If we consider first the fragmentation process, we can say that the secondary He nuclei have the same velocity as the producing

nuclei; the interaction lengths of the heavy nuclei are roughly

independent of energy (Noon and Kaplon, 1955; Cleghorn et al., 1968);

and the spectra of the producing nuclei (mostly CNO) are roughly the

same as that of the primary He nuclei (Mason, 1971). Hence, the

spectrum of He nuclei will be unchanged in shape by the fragmentation

process.

The attenuation of He nuclei in the atmosphere is also

roughly independent of energy (Appa Rao et al., 1956; Lohrmann and

Teucher, 1959; Waddington, 1954; Willoughby, 1956), and the effective

interaction length for production of He nuclei (Waddington, 1960) is

roughly equal to the interaction length for attenuation. These two

effects will therefore have equal and opposite effects on the spectrum

and can be ignored. At the $p\alpha e$ float altitude (2-3 gm/cm^2) this

approximation is quite good compared to the approximately 20%

statistical accuracy of the $p\alpha e$ data.

The second process for creation of secondary He nuclei, re-

lease from air nuclei, should, as pointed out earlier, have a steeply

falling energy spectrum. Thus, the corrections for this effect should

be negligible at high energies. In Figure IV-1 we compare He nuclei

spectra measured in 1969 with $p\alpha e$ and OGO-6. On the basis of this

comparison (and a similar comparison in 1970) and the preceding

discussion, we conclude that the $p\alpha e$ He spectra may be used without

correction for atmospheric secondary production above about 70 MeV/

nucleion. Below this energy the spectra are contaminated by

secondaries and will not be considered further.

V. SPECTRA AND RATE PLOTS

Since the spectra presented in this chapter will be used to study long-term time variations of cosmic-ray spectra associated with the solar modulation process, it is important to separate the effects of long- and short-term variations. One of the most readily available tools in the study of cosmic-ray time variations is the neutron monitor. These ground-based instruments are sensitive to cosmic-ray nuclei of energy roughly $\gtrsim$ 1 GeV/nucleon. They are constructed with large geometrical factors (determined by area and solid angle) so that the normally small time variations at these energies are not obscured by the presence of statistical fluctuations. Figure V-1 shows the neutron-monitor counting rate as a function of time for the Deep River neutron monitor (Steljes, 1965-1970) which is located at a geomagnetic cutoff of 1.0 GV (Stoker and Carmicheal, 1971). The times of the $p\alpha e$ balloon flights are indicated by vertical lines and the periods for which OGO-6 spectra have been calculated are shown by heavy bars. The 11-year solar cycle is quite obvious in the neutron monitor rates. It is also clear that the $p\alpha e$ and OGO-6 data cover a significant fraction of this cycle.

Short-term solar activity, e.g., solar flares, will be observable at the high energies typical of neutron monitor sensitivity only if the activity represents a considerable enhancement over the normal activity. Strong flares may be associated with Forbush decreases; or, very rarely, cause increased neutron-monitor counting rates.

To aid in the task of recognizing short-term enhancements of solar activity we have prepared "monthly summary plots" which include

several indices of solar activity. These plots are presented in Figures V-2a through V-2f (Garrard, 1971). Similar plots were prepared for the summers (balloon season) of 1967 and 1968 (Evans, 1971) using data from OGO-4.

There is no indication of enhanced solar activity during the balloon flights made in 1967 and 1968. Fewer data are available for 1966 but the IMP-OGO G.M.-tube counting rates (Balasubrahmanyan and Venkatesan, 1969) show no evidence of unusual solar activity. Note that $p\alpha e$, by virtue of being beneath 2-3 gm/cm^2 of residual atmosphere, is not nearly as sensitive as OGO-6 to solar activity, which is typically strongest at low energies.

For the periods in 1969 and 1970 during which the balloon flights were made, there is clear evidence of short-term activity. For this reason, we have also analyzed OGO-6 data from other periods -- periods in which solar activity is lessened. The spectra in Figure V-3 and V-4 for 1969 and 1970 were calculated from these data.

Figures V-3 and V-4 are plots of the spectra measured in the years 1966 through 1970 on $p\alpha e$ and OGO-6. They represent data taken during what seem to be periods of low solar activity. Tables V-1 and V-2 are presentations of the same data in tabular form.

The He spectra presented represent only those energy regions where a clean and unambiguous particle identification can be made, and where atmospheric secondary contributions are thought to be negligible.

Over the energy range and time span covered by our measurements some significant discrepancies exist among the spectra of protons and

He nuclei published by other observers. These differences may result from genuine time variations, or they may be due to uncertainties in corrections for instrumental effects or atmospheric secondary contributions. Our own detector systems have been extensively and fully calibrated on particle accelerators, and our corrections for atmospheric secondary contributions (see Chapter IV, sections C and D, and Appendix 2) have been directly verified by measurements made in and above the atmosphere. The reliability of our (generally small) corrections justifies confidence in the accuracy of our spectra. Spectra previously published by other observers will be considered in our discussion of solar modulation (for purposes of extending coverage, etc.) if they are in satisfactory agreement with our data. This should eliminate problems of time variations and minimize differences due to instrumental effects.

Protons

Range	Energy	Intensity	Flight Number
		1966	
R4	68-95	1.05 ± .10	66C2P,66C4P,66C5P
R4	95-125	1.10 ± .09	"
R4	125-166	1.25 ± .08	"
R5	166-242	1.32 ± .07	"
R6	242-321	1.46 ± .09	"
R7	>321	2597 ± 51	"
		1967	
R4	68-95	0.40 ± .08	67C1P,67C3P
R4	95-125	0.53 ± .08	"
R4	125-166	0.80 ± .07	"
R5	166-242	0.62 ± .05	"
R6	242-321	0.89 ± .08	"
R7	>321	2069 ± 51	"
		1968	
R4	70-96	0.29 ± .08	68C1P,68C2P
R4	96-126	0.44 ± .08	"
R4	126-167	0.57 ± .07	"
R5	167-243	0.60 ± .06	"
R6	243-322	0.76 ± .08	"
R7	>322	1794 ± 53	"

Range	Energy	Intensity	Days of Year
		1969	
R2	3.3-5	33 ± 1	220-253/1969
R2	5-7	5.4 ± .3	"
R2	7-9	1.4 ± .2	"
R2	9-15.0	0.37 ± .05	"
R2	15-18.5	0.26 ± .05	"
R3	18.5-25	0.20 ± .03	"
R3	25-35	0.10 ± .02	"
R3	35-46.6	0.11 ± .02	"
R4	46.6-78.6	0.16 ± .01	"
R4	78.6-112	0.21 ± .02	"
R4	112-156	0.24 ± .02	"
R5	156-235	0.27 ± .02	"
R6	235-315	0.30 ± .03	"
R7	>315	1399 ± 27	"
		1970	
R3	18.5-25	1.04 ± .13	
R3	25-35	0.30 ± .06	157-165/1970
R3	35-46.6	0.16 ± .04	"
R4	46.6-78.6	0.16 ± .03	"
R4	78.6-112	0.15 ± .03	"
R4	112-156	0.24 ± .03	157-165&171-175/1970
R5	156-235	0.20 ± .02	"
R6	235-315	0.17 ± .04	"
R7	>315	1419 ± 42	"

Table V-1. The proton intensity (in $[p/m^2 \text{ sec sr MeV}]$) is given as a function of energy (in MeV) at the top of the atmosphere. The "Range" notation is explained in Chapter IV and Appendix 1. The balloon flights are described in Table III-1.

Helium Nuclei

Range or Cerenkov	Energy	Intensity	Flight Number or Days of Year
		1966	
R4	68-11	0.14 ± .02	66C2P,66C4P,66C5P
R5	166-242	0.28 ± .03	"
R6	242-321	0.24 ± .03	"
R7	>321	200 ± 15	"
C	>400	239 ± 3	"
		1967-68	
R4	68-111	0.13 ± .01	67C1P,67C3P,68C1P,68C2P
R5	166-243	0.15 ± .02	"
R6	243-321	0.14 ± .02	"
R7	>321	199 ± 13	"
C	>400	180 ± 2	"
		1969	
R2	5-18.5	0.059 ± .013	220-253/1969
R3	32-46.6	0.035 ± .008	"
R4	46.6-78.6	0.044 ± .007	"
R4	78.6-112	0.061 ± .009	"
R5	156-235	0.087 ± .010	"
R6	235-315	0.089 ± .015	"
R7	>315	163 ± 10	"
C	>400	175 ± 2	"
		1970	
R3	32-46.6	0.045 ± .014	157-165&171-175/1970
R4	46.6-78.6	0.030 ± .009	"
R4	78.6-112	0.052 ± .014	"
R5	156-235	0.076 ± .015	"
R6	235-315	0.106 ± .026	"
R7	>315	148 ± 11	"
C	>400	188 ± 2	"

Table V-2

The intensity of He nuclei (in $[p/m^2$ sec sr MeV/nucleon] is given as a function of energy [in MeV/nucleon] at the top of the atmosphere. The "Range" notation is explained in Chapter 4 and Appendix 1. The letter "C" implies that the measurement was made with the Čerenkov telescope. The balloon flights are described in Table III-1.

VI. SOLAR MODULATION

A. Statement of the Problems

  The study of the solar modulation of the cosmic-ray intensity is important because it can furnish evidence on the interstellar spectra of charged particles and also, for the information it provides on the properties of the interplanetary medium. The physics governing the propagation of particles through the interplanetary medium is thought to be well understood. It is discussed in detail in a review paper by Jokipii (1971) and is very briefly reviewed in section B of this chapter. The transport equation which describes the motion of cosmic rays in the solar wind is adequately represented by

$$\vec{\nabla} \cdot (\vec{V}U) - \frac{\vec{\nabla} \cdot \vec{V}}{3} \frac{\partial}{\partial T} (\alpha TU) - \vec{\nabla} \cdot (\bar{\bar{\kappa}} \cdot \vec{\nabla}U) = 0 \qquad (VI-1)$$

where U is the number of particles per unit volume per unit energy with kinetic energy T (U = $4\pi j/\beta c$ where j is the intensity and βc is the particle velocity), V is the solar-wind velocity, $\alpha(T)$ is a parameter given by

$$\alpha(T) = \frac{\partial \ln T}{\partial \ln p} = \frac{W + m}{W}, \qquad (VI-2)$$

p is the particle momentum, m is the particle rest energy, W the total energy, and $\bar{\bar{\kappa}}$ is the particle diffusion tensor. The three terms in equation VI-1 represent, respectively, convection, adiabatic deceleration, and diffusion of charged particles in the interplanetary medium. No general, analytic solutions have been obtained.

  A list of outstanding problems which will be discussed in this

chapter includes:

1) The Diffusion Tensor It is generally accepted that the diffusion
   coefficient can be written as a function of particle velocity,
   magnetic rigidity, and position, and further, that it should be at
   least roughly in agreement with the values computed from measurements
   of the power spectra of the fluctuations in the interplanetary
   magnetic field observed at a point in space. However, the power-
   spectra measurements are far from complete. They have been made only
   near Earth and over a limited frequency (frequency is related to
   particle rigidity, or momentum per unit charge) interval. The un-
   certainties in the measurements and the uncertainties in the
   connection between the power spectra and the diffusion coefficient
   are large compared to the year-to-year changes in $\bar{\bar{\kappa}}$ needed to produce
   the measured particle modulation.

2) The Outer Boundary of the Modulating Region The simplest way to
   explain the characteristic exponential decay with time of the intensity
   of particles from solar flares is to postulate the existence of a
   boundary beyond which the diffusion coefficient is infinite. This
   model of a sharp boundary is clearly an idealization and will be
   investigated in the light of its effect on solar modulation.

3) The Flux at the Boundary This flux, $j_D(T)$, is the boundary condition
   under which the transport equation is to be solved. The high-energy
   interstellar cosmic-ray spectra are known to resemble a power law with
   a slope given by

$$\gamma = + \frac{d \ln j}{d \ln T} \approx -2.65 .$$

The shape of the interstellar spectrum at lower energies is unknown and is of considerable interest for astrophysics. Some investigators have argued that the spectrum must be flat at lower energies, but the evidence is not conclusive and the question is of sufficient importance that further investigation is clearly warranted.

4) The Analytic Approximations The regions of applicability of various analytic approximations to the solution of the transport equation are of considerable practical interest. In particular the "force-field" approximation has been widely used in the discussion of high-energy data and several investigators have stated that it seems useful at energies far lower than one might expect. The "j = AT" solution seems to agree with the low-energy data but there is a question of how far it can be extended.

5) Solar Emission A certain fraction of the spectrum of low-energy protons near Earth may be of solar origin. The extent to which solar emission dominates the spectra of low-energy protons has been debated in the literature and will be considered further.

     In this chapter we will briefly review the analytic approximations which are most frequently used in explaining the data and we shall rederive some of the formulae in a form which makes them somewhat simpler in appearance and, perhaps, easier to understand. Then we will show results based on numerical solutions to the "full" transport equation and compare these to the analytic approximations. In this manner, we can study the extent to which the approximations really represent valid solutions to the transport equation for various reasonable

assumptions for the radial and rigidity dependence of the diffusion coefficient, interstellar spectra, etc. This discussion is intended to show the properties of the transport equation and we will make reference to the measured spectra presented in the previous chapter only to put restrictions on what we call "reasonable" assumptions. Finally, in the last two sections of this chapter, we will show how the spectra are related to the values and functional forms of the parameters and compare our numerical solutions with the measured spectra.

B. Background Physics

Our understanding of solar modulation is based on the pioneering work of Parker (1963) in describing the physics of the interplanetary medium and the transport of particles in that medium. Parker showed that the solar corona, at a temperature of $\sim 2 \times 10^6$ K, is dynamically unstable and expands outward from the Sun with supersonic velocity. This "solar wind" is a highly ionized plasma and has been observed with spacecraft-borne plasma detectors. The fact that it is ionized means that it is conducting; thus, magnetic field lines from the Sun which pass through the corona are "frozen-in" and are swept out into interplanetary space with the solar wind. The radial expansion of the wind, combined with the rotation of the Sun, fills interplanetary space with a magnetic field which has, on the average, the shape of an Archimedes' spiral. Irregular fluctuations are superimposed on the average field. These fluctuations may be analyzed as magnetohydrodynamic waves which are being convected outward with the solar wind since the wave velocity ($\overset{<}{\sim}$ 50 km/sec) (Jokipii, 1971) is much less than the wind velocity ($\sim$400 km/sec) (Gosling et al., 1971). Charged particles whose gyroradius in the interplanetary field is roughly the same as the wavelength of a fluctuation will undergo resonant scattering. This scattering causes the particles to execute a random walk through the medium. Under these circumstances outward convection of the particles with the solar wind will produce a radial gradient, leading to diffusion in the opposite direction. Another important effect is the adiabatic deceleration of particles. That is, since the cosmic rays are contained in the expanding

solar plasma, they are cooled as it expands. Inclusion of all these effects leads to the transport equation, VI-1.

Jokipii (1966; 1967; 1968) has derived relations between the diffusion coefficient, $\bar{\bar{\kappa}}$, and the power spectrum of the interplanetary magnetic field so that the diffusion coefficient cannot be treated as a free parameter. Also, the propagation of particles produced in solar flares is described by a time-dependent transport equation of the same form as equation VI-1, giving still more information on the parameters.

The long-term variations in the parameters, especially $\bar{\kappa}$, produce a corresponding variation in the cosmic-ray spectrum and are the source of the 11-year cycle in cosmic-ray intensities which we call solar modulation.

C. Review and Restatement of the Analytic Approximations to the Transport Equation

We shall assume for simplicity that radial symmetry applies and that the solar wind velocity is independent of radius, r. Then the transport equation, VI-1, becomes

$$\frac{V}{r^2} \frac{\partial}{\partial r} (r^2 U) - \frac{2V}{3r} \frac{\partial}{\partial T} (\alpha T U) - \frac{1}{r^2} \frac{\partial}{\partial r} (r^2 \kappa \frac{\partial U}{\partial r}) = 0 \qquad (VI-3)$$

where κ is a scalar quantity (the κ_{rr} component of the diffusion tensor $\overline{\overline{\kappa}}$).

1. The Diffusion-Convection Approximation

If we ignore adiabatic deceleration and the Compton-Getting effect, we are left with an outward current of particles (or streaming) due to convection which must be balanced by an inward streaming due to diffusion:

$$VU = \kappa \frac{\partial U}{\partial r}$$

This is the diffusion-convection approximation, which has the solution

$$U(r,T) = U(\infty,T) \exp \left\{ - \int_r^\infty \frac{V}{\kappa} dr' \right\} \qquad (VI-4a)$$

of, if we assume a boundary at distance D, beyond which V/κ is zero,

$$U(r,T) = U(D,T) \exp \left\{ - \int_r^D \frac{V}{\kappa} dr' \right\} \qquad (VI-4b)$$

$$= U(D,T) e^{-\psi} \qquad (VI-4c)$$

The quantity ψ,

$$\psi(r,T) = \int_r^D \frac{V \, dr'}{\kappa(r',T)} , \qquad (VI-5)$$

will be seen to be the determining parameter in all of the high-energy

approximations and in the numerical solution at high energies (i.e.,

where ψ is small). We shall refer to it as the modulation parameter or

simply the "modulation." Note that here, and in what follows, we make

the assumption of a boundary at a finite distance D for convenience

only; it is not necessary.

The diffusion coefficient is assumed to have the usual form,

$$\kappa = \frac{\beta c \lambda}{3} ,$$

where λ is a mean-free path and βc^* is particle velocity. If we assume

that λ is separable into a function of heliocentric radius, r, and

magnetic rigidity, R, i.e.,

$$\lambda \propto g(r) \ f(R),$$

so that

$$\kappa = \beta \ g(r) \ f(R), \qquad\qquad (VI-6)$$

and if we assume that temporal variations in $f(R)$ are negligible, then

the diffusion-convection model implies that

$$\frac{U(r,T,t_1)}{U(r,T,t_2)} = \exp \left\{ - \frac{\eta_1}{\beta f(R)} + \frac{\eta_2}{\beta f(R)} \right\}$$

---

*
  The speed of light, c, is taken to be 1 but is sometimes written to
  make the dimensional nature of a given quantity more obvious.

where

$$\eta_i = \int_r^D \frac{V dr'}{g(r')} = \beta f(R) \psi \tag{VI-7}$$

at a time t_i.

We then define

$$M_{12} = \beta \, \ell n \, \frac{U(r,T,t_1)}{U(r,T,t_2)} = \frac{-\eta_1 + \eta_2}{f(R)} = \frac{-\eta_{12}}{f(R)} \quad . \tag{VI-8a}$$

M_{12} is the relative modulation function and can be determined from spectral measurements made near Earth (Ormes and Webber, 1968) which implies that the shape of $f(R)$ can be determined in the same way. Note that we may also define an absolute modulation function

$$M_1 = \beta \, \ell n \, \frac{U(r,T,t_1)}{U(D,T)} = -\frac{\eta_1}{f(R)} \tag{VI-8b}$$

Hsieh (1970) has shown how possible changes in the shape of $f(R)$ with time may be taken into account. Note that the function M_1 above relates the spectrum at Earth to the spectrum at the boundary at a given energy, T. We shall show later that, at low energies, the spectrum at Earth is essentially independent of the spectrum at the boundary, so that the modulation function is not meaningful at these energies.

2. The Power-Series Approximation

Parker (1965) calculated that a low energy particle might lose almost all of its energy before reaching the Earth; at these energies diffusion-convection is clearly not a good approximation. Goldstein et al. (1970b) have also discussed this feature on the basis of numerical solutions to the transport equation. Experimentally,

Murray et al. (1971) have noted that a feature of particles emitted in a solar flare decreased in energy with time. Mason (1972) concluded from the similarity in the shapes of the spectra of Carbon and Helium nuclei that there must be large energy losses for low-energy particles traversing the interplanetary medium. Jokipii (1971) has found a power series solution to the full transport equation, VI-3, which includes adiabatic deceleration on the assumption that $\frac{rV}{\kappa}$ and the modulation, ψ, are small. This solution may be written as

$$U(r,T) = U(D,T) \left[1 - \frac{2-\alpha\gamma}{3} \psi \right] \qquad (VI-9)$$

where $\gamma = \frac{d\ell n j}{d\ell n T}$ and $j = \frac{\beta c U}{4\pi}$ is the differential particle intensity. The spectral index, γ, is evaluated at the boundary. The parameter α was defined in equation VI-2. In this limit the radial gradient is given by

$$\frac{1}{U} \frac{\partial U}{\partial r} = \frac{1}{j} \frac{\partial j}{\partial r} = \frac{2-\alpha\gamma}{3} \frac{V}{\kappa} \qquad (VI-10)$$

Note that the diffusion-convection equation can be forced to give the same results if we change the diffusion coefficient by the factor $\frac{2-\alpha\gamma}{3}$. Thus, it is not possible to distinguish the power series solution from the diffusion-convection solution unless κ is known.

3. The Force-Field Approximation

Gleeson and Axford (1968) have found another approximation which is useful if the amount of modulation (ψ) is small. They make use of the quantity S which is the radial streaming (particle current density per unit energy) and is defined by the relation:

$$S = VU - \kappa \, \frac{\partial U}{\partial r} - \frac{V}{3} \frac{\partial}{\partial T} (\alpha TU) \tag{VI-11}$$

(Forman, 1970). Equation VI-3 may be rewritten in terms of S as

$$\frac{1}{r^2} \frac{\partial}{\partial r} (r^2 S) = - \frac{V}{3} \frac{\partial^2}{\partial r \partial T} (\alpha TU) \tag{VI-12}$$

A substitution of equation VI-9 into equation VI-11 will yield $S = 0$ if we assume that ψ is small and that $\gamma(r) \approx \gamma(D)$, i.e., that the spectral index is not changed by the modulation. Under these conditions, VI-11 may be solved as a first order equation for U or j. This method is known as the force-field approximation. The equation is most easily solved if we assume that κ is separable (equation VI-6). The solution is

$$\frac{j(r,W)}{W^2 - m^2} = \frac{j(D, W+\Phi)}{(W+\Phi)^2 - m^2} = \frac{j_D (W+\Phi)}{(W+\Phi)^2 - m^2} \tag{VI-13}$$

where W is the total energy of a particle and m is its rest energy. Φ may be thought of as the energy loss in diffusing to a radius r from the boundary. Φ may be energy dependent and is determined from the diffusion coefficient. Jokipii (1971) has shown that this "force-field" solution is equivalent to the solution VI-9 for small ψ.

4. The j = AT Approximation

      Rygg and Earl (1971) have recently suggested an approximate solution which is useful at low energies where the modulation is large and the effects of adiabatic deceleration are dominant. If the diffusion term (containing $\kappa \frac{\partial U}{\partial r}$) in equation VI-3 is considered to be small compared to the other terms then we get (Fisk and Axford, 1969)

$$\frac{V}{r^2} \frac{\partial}{\partial r} (r^2 U) - \frac{2V}{3r} \frac{\partial}{\partial T} (\alpha TU) = 0 \qquad (VI-14)$$

Rygg and Earl (1971) solved this equation under the assumption that α is constant, i.e., $\alpha = 2$, by

$$U(r,T) = T^{3/\alpha-1} \mathcal{F}(rT^{3/2\alpha})$$
$$= T^{1/2} \mathcal{F}(rT^{3/4}) \qquad (VI-15)$$

where $\mathcal{F}$ is an arbitrary function to be determined by the boundary condition. They suggest as a boundary condition that $U(To,r) = $ constant $= U(To,D)$ at some boundary energy To (i.e., no modulation for $T \geq To$). Then the solution is

$$U(r,T) = (T/To)^{1/2} U(To,D)$$
$$\text{or} \quad j(r,T) = AT \qquad (VI-16)$$

where A is a constant and non-relativistic kinematics is used.

5. Approximate Solutions of the Transport Equation in Terms of Phase- Space Density

The preceding discussion was given in terms of particle number density or intensity and kinetic energy since those quantities are closely related to the experimentally measured quantities and because the original papers were written in those terms. In the following section we shall summarize much of that discussion in terms of the more natural variables, the phase-space density, F, and the momentum, p. This approach will allow us to clarify some of the important points in these derivations.

The phase-space density is the number of particles per unit

volume (d^3rd^3p) in the six-dimensional $\vec{r}, \vec{p}$ phase space and is defined
in this work as

$$F = j/p^2 \tag{VI-17}$$

where j is the intensity.

We shall discuss only the force-field approximation and the
j = AT approximation in this section. The diffusion-convection solution
(equation VI-4) or the power-series solution (equation VI-9) may be
rewritten in terms of phase-space density by simply replacing U by F.

In order to analyze the force-field approximation we must first
consider the streaming, or a related quantity, the anisotropy, in terms
of phase-space density. For cosmic rays, which are almost isotropically
distributed in direction, we may represent the intensity as a function
of direction by

$$j(\theta) = j \cdot (1 + \delta \cos \theta)$$

where the $\theta = 0$ direction is selected to be in the direction of maximum
intensity. The coefficient δ is the anisotropy. It is related to the
streaming, S, by (Jokipii, 1971)

$$\delta = \frac{3S}{\beta cU}$$

$$= \frac{3}{4\pi} \frac{S}{j} = \frac{3}{4\pi} \frac{S}{p^2 F} \tag{VI-18}$$

In the interplanetary medium there are two effects which give rise to
spatial currents and hence anisotropies; one is the Compton-Getting
effect, which is obtainable from the Lorentz transformation from the

solar-wind rest frame to the frame of the Sun (or Earth or spacecraft), and the other is diffusion. Forman (1970) gives the anisotropy due to the Compton-Getting effect as

$$\delta_{CG} = \frac{V}{\beta c} \frac{d \ln F}{d \ln p} \qquad (VI-19)$$

Diffusion causes a current

$$S_\kappa = -\kappa \frac{\partial U}{\partial r}$$

or an anisotropy

$$\delta_\kappa = -\frac{3}{\beta c} \frac{\partial \ln U}{\partial r} = -\frac{3}{\beta c} \frac{\partial \ln F}{\partial r}$$

The total anisotropy can be written as

$$\delta = \delta_{CG} + \delta_\kappa$$

$$= -\frac{V}{\beta c} \left(\frac{\partial \ln F}{\partial \ln p} + \frac{3\kappa}{V} \frac{\partial \ln F}{\partial r} \right) \qquad (VI-20)$$

The total streaming follows from equations VI-18 and VI-20:

$$S = -\frac{V}{\beta c} \frac{4\pi}{3} p^2 F \left(\frac{\partial \ln F}{\partial \ln p} + \frac{3\kappa}{V} \frac{\partial \ln F}{\partial r} \right) \qquad (VI-21)$$

If we make the approximation that $S = 0$ (see section VI.C.3) we get

$$\frac{\partial \ln F}{\partial \ln p} + \frac{3\kappa}{V} \frac{\partial \ln F}{\partial r} = 0 \qquad (VI-22)$$

We can solve easily for the gradient at any given position and energy:

$$\frac{1}{F} \frac{\partial F}{\partial r} = \frac{1}{j} \frac{\partial j}{\partial r} = \frac{1}{3} \frac{\partial \ln F}{\partial \ln p} \frac{V}{\kappa}$$

$$= \frac{2 - \alpha\gamma}{3} \frac{V}{\kappa} \qquad (VI-23)$$

(equations VI-17 and VI-2 were used to evaluate $\partial \ln F / \partial \ln p$). In this equation γ is evaluated at r rather than at the boundary as in equation VI-10 and is not known unless the spectrum is known, but the equation is

still interesting for two particular reasons:

1) The resemblance to equation VI-10, which is based on the power-series solution, is striking.

2) If F is independent of p it will also be independent of r (in the force-field approximation). Thus F = constant (or j = AT) is, in a certain sense, a special case of the force-field approximation.

In order to solve equation VI-22 analytically, we need to assume that κ is a separable function of radius and rigidity (as before),

$$\kappa = \beta f(R) g(r) \qquad (VI-6)$$

Then equation VI-22 can be written

$$\left[\frac{p}{\beta f(R)} \right] \frac{\partial F}{\partial p} + \left[\frac{3g(r)}{V} \right] \frac{\partial F}{\partial r} = 0 \qquad (VI-24)$$

An equation of this form can be solved in terms of contour lines, along which F is constant. In this case the equation of the contour lines is

$$\int_0^p \frac{\beta' f(R')}{p'} \, dp' + \int_r^D \frac{V}{3g(r')} \, dr' = \text{constant} \qquad (VI-25)$$

or $Q(p) + \phi(r) = \text{constant}$, where

$$Q(p) = \int_0^p \frac{\beta' f(R')}{p'} \, dp'$$

and

$$\phi(r) = \int_r^D \frac{V}{3g(r')} \, dr' \qquad (VI-26)$$

If we specify the momentum, p_D, at which the contour intercepts the boundary D, then the constant is given by $Q(p_D) + \phi(D) = Q(p_D)$, since $\phi(D) = 0$. If W and W_D are the total energies corresponding to p and p_D

then we can define the spectral shift parameter Φ as

$$\Phi(r,W) = W_D - W(r)$$

$$= W_D - \left[(p(r))^2 + m^2 \right]^{1/2} \qquad (VI-27)$$

where the momentum, $p(r)$, is given by the countour line equation

$$Q(p(r)) + \phi(r) = Q(p_D)$$

or

$$p(r) = Q^{-1}\left[Q(p_D) - \phi(r) \right]$$

We can reconstruct the example given by Gleeson and Axford (1968) if we let $f(R) = R = p/|Ze|$. Then

$$Q(p) = \int_0^P \frac{\beta'(p'/|Ze|)}{p'} \, dp'$$

$$= \frac{1}{|Ze|} \int_m^W dW' = \frac{W - m}{|Ze|}$$

$$W(r) = W_D - |Ze| \, \phi(r)$$

$$\Phi = W_D - W(r) = |Ze| \, \phi = |Ze| \int_r^D \frac{V}{3g(r')} \, dr'$$

Thus, in this case, the modulation has the same form as if there were a heliocentric electric field given by $\int_r^D \frac{V}{3g(r')} \, dr'$ as noted by Gleeson and Axford (1968).

There are several problems with the force-field approximation: 1) It ignores adiabatic deceleration. It is based on equation VI-21,

which we derived from the Compton-Getting effect and diffusion.

2) It requires very small anisotropy, i.e., if we are to set S = 0 in equation VI-21 or, equivalently, δ = 0 in equation VI-19, then we must have $\delta \ll \frac{V}{\beta C} \sim 10^{-3}$. While the assumption of zero streaming is consistent with equation VI-10 (the power-series solution), the region of validity of these approximations is unclear.

3) It is not a unique solution. The j = AT approximation also predicts zero streaming. We shall present an example of a solution which gives zero streaming and satisfies the boundary condition at r = D (which j = AT does not do).

In order to construct this example we must use the transport equation to rewrite equation VI-21. In equation VI-12 we wrote the transport equation in terms of S, T, and U. A change of variables to S, p, and F yields

$$\frac{1}{r^2} \frac{\partial}{\partial r} (r^2 S) = - \frac{V}{\beta c} \frac{4\pi}{3} \frac{\partial^2}{\partial r \partial p} (p^3 F) \qquad (VI-28)$$

If we substitute for S using equation VI-21 we get

$$\frac{V}{r^2} \frac{\partial}{\partial r} (r^2 F) - \frac{2V}{3r} \frac{1}{p^2} \frac{\partial}{\partial p} (p^3 F) - \frac{1}{r^2} \frac{\partial}{\partial r} (r^2 \kappa \frac{\partial F}{\partial r}) = 0$$

or

$$\frac{\partial F}{\partial r} - \frac{2p}{3r} \frac{\partial F}{\partial p} - \frac{1}{r^2} \frac{\partial}{\partial r} (r^2 \frac{\kappa}{V} \frac{\partial F}{\partial r}) = 0 \qquad (VI-29)$$

Note that considerable cancellation takes place between the term due to the Compton-Getting effect and the adiabatic deceleration term, since they have the same form in a spherical geometry. It is worthwhile to emphasize the point that although the Compton-Getting term and the

adiabatic deceleration term have the same form, they represent different physical effects. Both terms must be included in a complete solution. We repeat that equation VI-20 for δ or equation VI-21 for S contains no specific reference to adiabatic deceleration; this effect enters through the quantity F which is correctly determined from the transport equation. If we perform the divergence operation indicated on the left hand side of equation VI-28 and use equation VI-18 to relate S and δ, we find

$$\delta = -\frac{r}{2} \frac{V}{\beta CF} \left(\frac{1}{p^2} \frac{\partial^2}{\partial p \partial r} (p^3 F) - \frac{\partial}{\partial r} (F\delta)\right)$$

If we now substitute equation VI-20 into the right-hand side of the above equation and simplify, we get

$$\delta = -\frac{V}{\beta C} \frac{3r}{2F} \frac{\partial}{\partial r}(F - \frac{\kappa}{V} \frac{\partial F}{\partial r}) \qquad (VI-30)$$

(Fisk and Axford, 1969). If we set $\delta = 0$ in equation VI-30 and integrate twice we get a solution

$$F(r,T) = e_1(p) + e_2(p) \exp\left\{-\int_r^D \frac{V}{\kappa} dr'\right\}$$

$$= e_1(p) + e_2(p)e^{-\psi}$$

where $e_1(p)$ and $e_2(p)$ are constants of integration. We see that we have two unknown constants and only one boundary condition, which is $F(r,T) \rightarrow F(D,T)$ as $r \rightarrow D$. As an example, we can use equation VI-10 to determine the gradient at the boundary. This relation can be used as the second boundary condition and the solution is then

$$F(r,T) = F(D,T) (1 + \frac{2-\alpha\gamma}{3} (e^{-\psi} - 1)). \qquad (VI-31)$$

We emphasize that this solution is not being offered as a serious

"contender" for a useful analytic approximation to the full solution
to the transport equation; it is given as an example that $S = 0$ is an
insufficient condition to determine the solution to the transport
equation. It is interesting to note the striking similarity to the
power-series solution, equation VI-9.

The reason that the solution VI-31 is different from the force-
field approximation, equation VI-13, is that it includes the effects
of adiabatic deceleration while the force-field solution does not. The
force-field solution is based on the definition of the streaming,
equation VI-11 or the equivalent VI-21, which includes only the Compton-
Getting effect and the diffusive current. The solution VI-31 is based
on VI-30 which includes the adiabatic deceleration term since it was
derived using the full transport equation VI-28. (In fact, since the
Compton-Getting term and the adiabatic deceleration term have the same
form, some cancellation occurs and the terms remaining are those we
would associate with diffusion-convection.)

Now consider the $j = AT$ solution. If, as before, the term
involving $\kappa \frac{\partial F}{\partial r}$ is dropped from equation VI-29, then

$$r \frac{\partial F}{\partial r} - \frac{2p}{3} \frac{\partial F}{\partial p} = 0 \tag{VI-32}$$

This equation is of the same form as equation VI-24 and similarly has
a solution in terms of contour lines. The equation of the contour
lines is given by

$$\int_1^r \frac{dr'}{r'} + \int_1^p \frac{dp'}{2p'/3} = \text{constant}$$

or

$$rp^{3/2} = \text{constant},$$

i.e.,

$$F(rp^{3/2}) = \text{constant} \tag{VI-33}$$

The solution is the same as equation VI-16 except that we have not used the approximation that α is constant. Again, if we impose the boundary condition that $F(r,p_o) = F(D,p_o)$, i.e., is independent of radius, then the solution is

$$F = \text{constant}$$

or

$$j = A\,p^2 \approx AT \qquad\qquad (VI-34)$$

Note that this solution depends critically on the boundary condition imposed. If $F(r,p_o)$ is allowed to depend on r, or if p_o is allowed to depend on r, then $F(r,p)$ will not necessarily be constant. Thus, we cannot argue on this basis that $j = AT$ is a necessary solution for large modulation.

6. Summary

We have considered the four most commonly used approximations to the complete solution of the transport equation. Using the phase space density instead of the number density or intensity as the dependent variable we have pointed out the strengths and weaknesses of each of these approximations, in so far as we are able to do so without having the complete solution for comparison. These strengths and weaknesses are summarized below:

1) Diffusion-Convection. This model neglects adiabatic deceleration and also neglects that part of the Compton-Getting term which has the form $\frac{V}{3}\frac{\partial}{\partial T}(\alpha TU)$. It is not a good approximation at any energy but can be made to agree with the improved approximations 2) and 3) by adjusting the diffusion coefficient.

2) Force-Field Approximation. This model includes the full Compton-
    Getting effect but still neglects adiabatic deceleration. It, also,
    can be fit to the observational data at some energies and radii
    where it is no longer a valid approximation to the solution to
    the transport equation by adjusting the diffusion coefficient.

3) Power Series Solution. Here adiabatic deceleration is included but
    the assumption of small rV/κ and small modulation limits its
    applicability to high energies.

4) $j = AT$. This model applies in the opposite limit, that of large
    modulation. One must assume $\kappa \frac{\partial F}{\partial r}$ is small; also, and with less
    justification, one must impose the somewhat artificial boundary
    condition that $F(r, p_o) = $ constant.

D.   Numerical Solution of the Transport Equations

A numerical calculation of the solution to the "full transport equation," equation VI-3, has several advantages over the approximate solutions discussed in the preceding section. In particular, a numerical solution can be calculated which is valid for all values of energy and radius of interest, if the necessary parameters (diffusion coefficient as function of rigidity and radius, interstellar spectra, etc) are given; indeed, one may use the numerical solution to test the validity or relevance of an analytic approximation under a given set of circumstances. Furthermore, numerical solutions can easily be calculated on a computer for a variety of different functional dependences of $\lambda(R,r)$; whereas a new analytic solution would presumably be necessary for each different $\lambda(R,r)$.

In order to get solutions valid for a larger range of parameters and to investigate the dependence of the solution on the parameters, we have calculated a number of numerical solutions to equation VI-3, the "full transport equation." This has been done using the Crank-Nicholson implicit finite-difference technique as suggested by Fisk (1968, 1971). The transport equation is replaced by a finite-difference equation and, given the boundary conditions at some large energy, T_b, at $r = D$, and at $r = 0$, we can calculate the solution at all points r and T inside the boundaries. The boundary conditions are unknown, indeed, some of them contain significant physical information. They are treated in the following manner:

1) $T = T_b$. We can pick some T_b which is large enough that the modula-

tion is small, hence $U(r,T_b) = U(D,T_b)$ for all r.

2) $r = 0$. We transform the equation so that the dependent variable is $\sqrt{r}$ U which we require to be zero at $r = 0$ in order to eliminate source-like solutions (Fisk, 1971). The necessity of factoring out the $\sqrt{r}$ dependence means that the solutions are not valid for small r ($\lesssim 0.2$ A.U. typically).

3) $r = D$. The spectrum in interstellar space is unknown, and is one of the quantities which we hope to investigate. Various assumptions are made and the resulting spectra at Earth are compared with the measurements.

E. Discussion of Properties of the Numerical Solution: Comparison
    with Analytic Approximations

Figure VI-1 shows a typical numerical solution to the transport
equation compared to the measured proton spectrum near Earth for the
year 1968. The upper curve is the input spectrum, i.e., the assumed
interstellar proton spectrum which is used in the numerical solution
as a boundary condition. The lower curve is the calculated spectrum
at Earth and the points indicate the measurements. Except at the lowest
energies the agreement is quite good. We shall argue later that the
discrepancy at low energies indicates the existence of quiet-time solar
emission. At this point we wish only to claim that the good agreement
over the relevant range of energies indicates that the parameters used
are not unreasonable. We will investigate the properties of the
numerical solution to the transport equation using parameters at least
roughly the same as those used in Figure VI-1.

1) Diffusion coefficient. We expect the energy dependence to be roughly
    that given by Jokipii and Coleman (1968) or Lupton (1971). Thus

$$\kappa \; \alpha \; \beta \begin{cases} R^{\nu_1} & R > R_o \\ R^{\nu_2} & R < R_o \end{cases} \tag{VI-35}$$

where R is magnetic rigidity and $\nu_1 \sim 1$ to 2, $\nu_2 \sim 0$ to 0.5 and
$R_o \sim 1000$ MV. The radial dependence is even more uncertain and we
have considered, among others, the four shapes shown in Figure VI-2.
The results of Jokipii and Coleman (1968) indicate that, within the
precision of their measurements, the radial dependence of κ is not
pronounced between 1.0 and 1.5 A.U. The results of Lupton (1971)
imply that the diffusion coefficient does not decrease inside 1 A.U.

On the basis of recent results, Sari (1972) claims that the diffusion coefficient varies roughly as $r^{-2.7}$ between 1.0 A.U. and 0.8 A.U.

2) Boundary. The boundary distance was generally taken to be only a few A.U. (~3 A.U.) on the basis of solar particle studies but more distant boundaries were also considered.

3) Interstellar Spectra. In this section most of the calculations assume a total-energy power-law spectrum at the boundary, $j_D \propto W^{-2.65}$. In the next section we find that the interstellar spectrum $j_D \propto (W-0.25m)^{-2.65}$ yields better fits to the observational data. The slight difference in these two input spectra does not affect the results reported here.

We have, of course, also investigated the behavior of the numerical solution in cases where the parameters were varied significantly from these, but these parameters seem to provide a reasonable "point of departure."

Figure VI-3 is identical to Figure VI-1 except that the ordinate is now phase-space density instead of intensity. The phase-space density is important for the reasons discussed in the previous paragraphs, i.e., it seems to be a "natural" variable. Since both the force-field solution and the j = AT solution are expressed in terms of contour lines and since it is of interest to study the solution at all radii, not merely at 1 A.U., we have generated contour plots of the solution.

Figure VI-4 serves as an introduction to these contour plots. Figure VI-4a is a plot of the phase-space density, $F(r,T)$, as a function

of kinetic energy, T, at a fixed radius of 1 A.U. Figure VI-4b is a
plot of F(r,T) versus radius at a fixed energy of 50 MeV. Figure VI-4c
is a perspective plot of F(r,T) versus r and T. The two heavy lines
indicate the radial and energy cross-sections which are shown in the
upper plots. Contours of constant phase-space density may be drawn on
the surface illustrated and projected onto the radius-energy plane.
Figure 5 shows four such contour plots. Each contour line represents
a constant change in the logarithm of F or, equivalently, a change in
F by a constant factor (of 1.5). A kinetic-energy power law would
show up as equal line spacing. A region where F is roughly constant will
show up as a low density of lines.

Such a feature is displayed fairly strongly in Figure VI-5a
less strongly in Figure VI-5b. The difference between these plots is in
the radial dependence of κ -- Figure VI-5a is based on a diffusion
coefficient which is independent of radius; Figure VI-5b is based on
a diffusion coefficient proportional to $(2 + r^3)/3$. (This form was
selected to yield a diffusion coefficient which is only slightly
dependent on radius for $r \lesssim 2$ A.U., but strongly dependent on r for large
r, providing a gradual transition to the interstellar medium.) The
difference in the importance of the $j = AT$ component in the two
solutions is clearly visible. We remind the reader that the derivation
of constant phase-space density given by Rygg and Earl depended
critically on the assumption that there existed an energy, T_o, (see
equations VI-15 and VI-16) at which the solution was allowed to change
character, i.e., an energy boundary. The difference between the solutions

in the large-modulation region in Figures VI-5a and b may be attributed

to the difference in the energy boundary. Now, clearly, we do not wish

to argue that some such sharp boundary really exists, however, it would

appear that in both Figure VI-5a and Figure VI-5b there is a

transition between a small-modulation region in which the contours are

predominantly horizontal and presumably are reasonably well described

by the force field approximation, and a large-modulation region in which

the lines tend to be vertical and spread out. In Figure VI-5a this

transition takes place along a boundary which is roughly horizontal,

hence we expect $j = AT$ to be important. In Figure VI-5b the transition

boundary is definitely not horizontal so that it does not satisfy the

requirements of the derivation, and consequently it shows less of the

$j = AT$ component.

The question immediately arises - what characterizes the boundary?

At what point do the small-modulation approximations cease to be useful

and the large-modulation approximation become a better fit? We

considered the following parameters as indicators for the applicability

of a particular approximation.

1) $\psi = \displaystyle\int_{r}^{D} \frac{V dr'}{\kappa}$

2) $\Phi - T$, where Φ is the spectral shift parameter specified by equation VI-27

3) rV/κ

4) κ

The last two of these can be eliminated fairly easily by inspection of

Figure VI-5a. Consider first contours of constant κ. The diffusion

coefficient is independent of radius, hence a contour line of constant

κ would be a straight line at a constant energy. Since the "boundary" of the large-modulation region tilts somewhat downwards (i.e., to smaller energies) as r increases and the contour line of κ does not, we conclude that contour lines of κ do not describe the boundary. This conclusion is supported by studies of large numbers of contour plots of this sort, with varying magnitudes of the diffusion coefficient. The diffusion coefficient, κ, is a monotonically increasing function of energy, thus contour lines of rV/κ would tilt upwards (toward larger energies) with increasing r(rV/κ constant while r increases implies κ increases, which implies T increases). Thus lines of constant rV/κ also do not describe the boundary of the large-modulation region. Both ψ and Φ - T have contour lines of roughly the appropriate shape to describe the boundary, but contours of ψ fit somewhat better. The dotted lines in Figures VI-5a and VI-5b are lines of constant ψ, ψ = 2.5.

Figures VI-5c and VI-5d show two further examples of contour plots, plots in which the radial dependence of the diffusion coefficient is changed substantially inside 1 A.U. It is seen that in Figure VI-5d where the diffusion coefficient is small near the Sun there is essentially no region of constant phase-space density, F, while in Figure VI-5c where the diffusion coefficient is very large near the sun, there is a large region of constant F. The explanation given for the differences in Figures VI-5a and VI-5b also applies here and the ψ = 2.5 line is also indicated on Figures VI-5c and VI-5d. A somewhat simpler, graphical explanation suggests itself in these extreme cases, however. Consider a contour line which originates at high energies at the boundary, D.

Inside 1 A.U., where the diffusion coefficient is very small, such a line will curve towards lower energies. That is, the small diffusion coefficient implies a large gradient, which, in turn, implies closely spaced, more-or-less vertical, contour lines. As these lines enter the low-energy region where the diffusion coefficient is still smaller they approach the $rp^{3/2}$ shape which is implied by a balance of convection and adiabatic deceleration with no diffusion (See equations VI-32 and VI-33.). Thus these lines recross the $r = 1$ A.U. cut at low energies, implying a lower phase-space density. In the other extreme, shown in Figure VI-5c, where the diffusion coefficient is very large near the Sun, the lines which cross the $r = 1$ A.U. cut at high energies do not curve towards low energies since the very large diffusion coefficient implies a small gradient and roughly horizontal contour lines. Since the lines which originate at the boundary at low energies never reach 1 A.U. and the lines which originate at the boundary at high energies are not turned down into the low-energy region, there is a large region with few contour lines, i.e., a large region of $F \approx$ constant.

On the basis of these results and other similar results too voluminous to present here we would suggest the following scheme for understanding the behavior of the solutions to the transport equation.

1) For small ψ, i.e., $\psi \overset{<}{\sim} 0.1$ the force-field model or the power-series solution give a good fit to the numerical calculation. In this region these solutions have the same form as the numerical solution, and they predict an intensity which is close to that predicted by the numerical solution.

2) For $2.5 \stackrel{>}{\sim} \psi \stackrel{>}{\sim} 0.1$ the force-field solution and the numerical solution still have the same form but the differences in the predicted values of the intensity at a specified point becomes more and more significant.

3) For $\psi > 2.5$ the force-field solution no longer has any similarity to the numerical solution, rather, one is now in a region where the solution depends critically on the radial dependence of the diffusion coefficient and is insensitive to the integral parameter, ψ, in that region. The contour lines should approach a shape of $rp^{3/2} =$ constant and if the radial dependence of ψ is weak then the spectrum will have the $j = AT$ shape.[*]

Note the perhaps surprising tendency of the force-field solution to merge quickly and smoothly into the $j \doteq AT$ solution, expecially in the case represented by Figure VI-5b. We recall to the reader the discussion following equation VI-28 in which we pointed out that if $\alpha = 2$ and $\gamma = +1$ then the force-field approximation predicts $\frac{\partial F}{\partial r} = 0$. Thus, $F =$ constant is, in a sense, the limiting case of the force-field solution for large modulation. One must be careful not to attach too much weight to this limit since the force field solution is not valid for large ψ, but it does present a reasonably consistent picture.

---

[*] Similar results were reported by other investigators at the spring meetings of the AGU and the APS (Fisk et al., 1972; Forman et al., 1972).

F. Discussion of Properties of the Numerical Solution: Determination
    of the Parameters

Given only a series of spectra of protons and He nuclei, such
as we have measured, it is not possible to precisely determine the
parameters, κ and j_D, of the transport equation. We find that, over a
large range of variation in the parameters, the spectrum near Earth at
high energies is determined fairly well by j_D and the modulation para-
meter, ψ. One can, of course, construct any number of different models
for κ (r,T) which yield the same ψ. Changes in j_D can be compensated by
changes in ψ, again over a large range of parameters.

Figure VI-6 illustrates, for example, that the high energy
spectra are determined by the parameter ψ. The spectrum at Earth has
been calculated for the indicated interstellar spectrum and for six
values of boundary distance, D, ranging from 2.7 A.U. to 35 A.U. A
simple model with κ independent of radius has been used. The energy
dependence of κ is the same in each case and the magnitude of κ was
adjusted so that ψ is the same at 1 A.U.

The lack of change in the high energy part of the spectrum may
be understood in terms of small modulation approximations. Both
diffusion-convection and the power-series solution depend on the
diffusion coefficient only through ψ, which is held constant at Earth;
the force-field solution is determined by the related quantity ϕ, which
is also constant.(These quantities are defined in equations VI-5 (ψ)
and VI-30 (ϕ).)

It is interesting to note that the intensity at low energies
increases as the distance to the boundary increases, i.e., the nearer

the boundary is, the fewer low-energy particles are observed at 1 A.U.. The low-energy portion of the spectrum is steeper than $j = AT$ for small boundary distances and approaches a limit of $j = AT$ as the boundary distance is increased. The behaviour at low energies may be interpreted graphically in terms of the contour plots. The condition for $j = AT$ is that the "box" roughly formed by the contour lines $\psi(r,T) = 2.5$ have an upper boundary which is horizontal. For a diffusion coefficient which is independent of radius,

$$\psi = \frac{V(D-r)}{\kappa(T)} \quad .$$

For $r \sim 1$ A.U., the term $(D-r)$ is almost independent of r if D is large. Thus, the slope of the top of the box near 1 A.U. is smaller for large boundary distance, D.

Figure VI-7 shows calculated spectra at Earth for two characteristic input spectra, one proportional to T^γ and the other proportional to W^γ, with $\gamma = -2.65$. It would be very difficult to choose between these calculated spectra on the basis of the measured spectra.

An even more serious problem in trying to use the spectra at Earth to determine interstellar spectra is the fact which may be loosely expressed by saying that particles which are incident upon the boundary with low energies have very small probabilities of reaching the Earth (Gleeson and Urch, 1971; Urch and Gleeson, 1972). This feature can also be expressed by saying that in the limit of large modulation ($\psi > 2.5$) the spectrum will be roughly given by $j = AT$ and is independent of the low-energy part of the input spectrum. The low-energy portions of

either of the input spectra in Figure VI-7 may be changed by several orders of magnitude without affecting the spectra at Earth. This result is indicated schematically for the total-energy power-law spectrum by the shaded area. Any input spectrum in the shaded region would give roughly the same spectrum at Earth. A corollary of this argument is the conclusion that the calculated spectrum of galactic particles near Earth does not turn up in the region of large ψ. If ψ is large then the turnup in the low-energy portion of the measured proton spectrum must be attributed to solar emission. The only way to reproduce the measured turnup is to increase κ by more than an order of magnitude at low energies, thus making $\kappa \propto R^{-2}$ (roughly) at low energies. The studies of solar-flare particle propagation and of the magnetic-field power spectra contradict such an assumption.

It is clear that more information than just the spectra of protons and He nuclei is necessary if we are to narrow the range of the parameters $j_D(T)$ or $\kappa(r,T)$. Some of the more obvious measurements that are (or would be) useful are:

1) radial intensity gradients

2) directional anisotropies

3) detailed spatial and temporal behaviour of solar flare particles

4) diffusion coefficients

5) electron and positron spectra.

1. The Radial Gradient

Radial gradients have been determined by several investigators (O'Gallagher, 1967; Anderson, 1968; Krimigis and Venkatesan, 1969;

Lezniak and Webber, 1970; Bercovitch, 1971; Formal et al., 1971; Fireman and Spannegel, 1971), but it is very difficult to deduce an accurate gradient from the measurements. The inconsistencies in the gradients given by these investigators are large, even compared to the large error bars quoted. We make no attempt to judge these results, but we show examples of the gradients predicted for several characteristic sets of parameters in Figure VI-8. The calculated gradient is plotted as a function of radius for two energies, 25 MeV and 500 MeV, for the simple case where κ is independent of radius. Note that in all cases the gradient at low energies is a strong function of radius, being large at the boundary and becoming small at smaller radii where the j = AT approximation is better. The gradient at high energies is almost independent of radius (for κ independent of radius) and serves as a good indicator for the value of κ.

2. The Anisotropy

In Figure VI-9 we show radial anisotropies calculated from the numerical solution to the (spherically symmetric approximation to the) transport equation. Plotted are contours of constant anisotropy for κ independent of radius. The anisotropies are small at large energies as predicted by the power-series solution and as assumed by the force-field solution. In the large-ψ region the anisotropies are again small as one would expect from F = constant. The anisotropy is somewhat larger in the small-T, large-r region where neither j = AT nor the force-field approximation is valid. The anisotropies calculated using the spherically symmetric model adopted in this work cannot be compared with the diurnal

anisotropies measured with neutron monitors (Jokipii, 1971) since those
are thought to arise from the off-diagonal terms in the diffusion
coefficient.   Rao et al. (1967) have reported small anisotropies in
the direction away from the sun at low energies.   Since we predict
anisotropies in the solar direction for galactic particles (i.e., an
excess flow toward the Sun), we conclude, as did Rao et al., that these
measurements indicate the existence of solar emission.

3.   Propagation of Solar Flare Particles

Particles from solar flares propagate outwards through the inter-
planetary medium and are subject to the same forces as are galactic
cosmic rays propagating inward from the boundary.   Lupton (1971) has
provided the most complete analysis to date of these phenomena.   He
concludes the propagation of solar flares is quantitatively well
described by the time-dependent transport equation if the diffusion
coefficient is similar in form and magnitude to that of Jokipii and
Coleman (1968).   He used boundary distances in the range, ~2.5 to
~5 A.U.   If we assume that the boundary is as close at 5 A.U. and use
the diffusion coefficients of Jokipii and Coleman, we can fit the
measured proton spectra only by using an input spectrum of lower
intensity than the total-energy power law plotted in Figure VI-7.   On
the other hand, the large amount of relative modulation (a factor of
~5 from 1965 to 1969 for 250 MeV protons) is inconsistent with the
observations that the diffusion coefficient does not change significantly
if the absolute modulation is small.   (See, for instance, the results of
McCracken and Rao (1970).   See also Mathews et al.   (1971).)   That is,
the large diffusion coefficients and small boundary distances used by

Lupton (1971) imply small ψ and hence small absolute modulation, which is inconsistent with the large changes in ψ needed (if ψ is small) to reproduce the large changes in the measured proton spectrum. However, the work of Lupton and recent investigations of solar particle events performed in this laboratory have disclosed events in which the equilibrium decay time of solar flares is much longer than the decay time observed during the first few days. The possibility exists that the decay times of solar particle fluxes are consistent with larger boundary distances (> 5 A.U.) with the same diffusion coefficients previously used with a boundary distance of 2.7 A.U. In this case the solar particle data may be consistent with large absolute modulation of galactic cosmic rays.

4. Diffusion Coefficients

The power spectra of the interplanetary field, and hence the diffusion coefficient, have been measured (Coleman, 1966; Siscoe et al., 1968; Sari and Ness, 1969; Bercovitch, 1971; Mathews et al., 1971) near Earth. These diffusion coefficients also do not appear to change by large amounts. In order to match the spectra at Earth with these diffusion coefficients, we must assume either an input spectrum with intensities less than those shown in Figure VI-1 or a large boundary distance (with κ independent of r). Again, the relatively small variations in κ and the large changes in the modulation imply that the absolute modulation is large.

5. Electron and Positron Spectra

The electron and positron spectra are modulated in a fashion

similar to that of the heavier particles. Since they have relativistic

velocities there are some differences:

a) κ is an increasing function of velocity and rigidity (recall

equation VI-35). Thus, the electrons will have a larger

diffusion coefficient at the same energy than protons.

b) The parameter α is essentially always 1 for electrons. Thus,

adiabatic deceleration (see equation VI-3) is less important

than for protons.

For these reasons, the electron spectra are less sensitive to the radial

dependence of the diffusion coefficient and, hence, serve as more

sensitive indicators to the value of ψ than the low-energy protons, for

which the spectrum is roughly j = AT and is insensitive to ψ.

In contrast to the protons and alpha particles, the interstellar

spectrum of electrons and positrons can be at least crudely deduced

from measurements made at Earth -- electrons from non-thermal galactic

radio spectra, and positrons from calculations of their production and

storage in the interstellar medium. Given these interstellar spectra,

the spectra measured at Earth can be used to determine ψ(1 A.U., T).

This value of ψ is also applicable to protons and alpha particles

(Goldstein et al., 1970a) and allows us to deduce the interstellar

spectra of these nuclei (with the restriction that the low-energy

portion of the spectrum is still not determined).

G. Comparison of Measured and Calculated Spectra

The test of any physical model is, of course, a quantitative comparison of its predictions with measurements; such comparisons are made in this section. In order to predict the spectra of galactic protons and He nuclei at Earth we need the parameters $K(r,T)$, their diffusion coefficient, and $j_D(T)$, their spectra in the interstellar medium.

We have determined the parameter K in the following manner:

1) From electron data a value of the integral modulation parameter,

$$\psi(1 \text{ A.U., } T) = \int\limits_{1}^{D} \frac{V dr'}{K(r',T)} \, ,$$

may be determined. This method is used because, in the energy range covered by our measurements, the proton spectrum is less sensitive to the value of ψ than the electron spectrum.

2) We make the simplifying, and not unreasonable, assumption that the diffusion coefficient is independent of heliocentric radius, r, for $r < D$. This allows us to represent the radial dependence of the diffusion coefficient by the single parameter D, the boundary distance. In this case K is related to ψ by

$$K(T) = \frac{V(D-1)}{\psi(1 \text{ A.U.,} T)}$$

Studies of the propagation of solar-flare protons presently suggest an effective boundary distance within the range from ~2.5 A.U. to ~6 A.U. Two characteristic values of the boundary distance, i.e., 2.7 A.U. and 6.1 A.U., which roughly bracket this range, were used for most of the calculations reported in this section. The effects

of boundary position on the spectrum were discussed in the preceding
section.

The diffusion coefficient can be described by the parameters η, k_0, R_0,
and D. (Recall equations VI-35 and VI-7.)

$$K = k_0 \beta \, f(R)$$

$$= k_0 \beta \begin{cases} \dfrac{R}{\sqrt{R \, R_0}} & \begin{array}{l} R \geqslant R_0 \\[12pt] R \leqslant R_0 \end{array} \end{cases}$$

$$\eta \ (1 \ \text{A.U.}) = \frac{V(D-1)}{k_0}$$

All calculations presented in this work assume a constant solar-wind
velocity of

$$V = 2.67 \times 10^{-6} \ \text{A.U./sec}$$

$$= 400 \ \text{km/sec}.$$

The transport equation (see equation VI-29, for instance) and the
modulation parameter, ψ, depend only on the ratio K/V. Thus, no
generality is lost by assuming a particular value for V. A list of
the values of the parameters, η, k_0, R_0, and D which were used to
calculate the spectra presented in this section is given in Table VI-1.
These values will be compared with results based on power spectra of
the interplanetary magnetic field.

The determination of the parameter ψ (or η and R_0) was made by
Cummings (1972) in this laboratory. He has performed a careful re-analysis
of the non-thermal galactic radio spectrum to determine the inter-
stellar electron spectrum. Using the interstellar electron spectrum
derived in this manner, the measured electron spectra at Earth, and

numerical solutions to the transport equation, he determined Ψ(1 A.U., T)

for the periods 1965-66 (averaged), June-October 1968, June-July 1969,

and June-July 1970. These values correspond to the entries numbered 2,

4, 5 and 8 (respectively) in Table VI-1. They are preliminary at this

time. There are naturally uncertainties in Ψ associated with the

uncertainties in the measured and interstellar spectra of electrons. A

more complete discussion will appear in his thesis.

The entries in Table VI-1 for other epochs were obtained by

making small changes in Cummings' values, which yield improved fits to

the data. These changes are consistent with the expected temporal

behaviour of the modulation, as explained below.

The interstellar spectra of protons and He nuclei were determined

as follows:

1) The interstellar spectra of both protons and alpha particles are

   assumed to be of the form

   $$j_D \propto (W-\mu m)^{-2.65}$$

   A useful feature of this form is that a power-law spectrum in total

   energy may be represented by $\mu = 0$ and a power law in kinetic energy

   by $\mu = 1$. The assumption that the interstellar spectra of both

   protons and He nuclei are of the same form is made for simplicity.

   We also assume, with reasonable confidence, that the interstellar

   spectra are independent of time. The exponent in the above

   equation is derived from the spectra of nuclei at high energies

   where the effects of solar modulation are negligible.

2) A value of μ is determined by calculating the spectrum of protons at

   Earth, using K determined for 1968 as described above, and comparing

Entry Number	η (MV)	k_0' ($\times 10^{-9}$)	k_0' ($\times 10^{17}$)	R_0 (MV)	D (A.U.)	Epoch and Figure Reference
1a	1194	3.80	8.55	500	2.7	1965 Figure VI-13
1b	"	11.40	25.66	"	6.1	
2a	1375	3.30	7.43	900	2.7	1965-66 Figures VI-11a & b
2b	"	9.90	22.28	"	6.1	& Figures VI-12a & b
3a	1746	2.60	5.85	750	2.7	1967 Figures VI-14
3b	"	7.80	17.55	"	6.1	
4a	1948	2.33	5.24	750	2.7	1968 Figures VI-11c & d
4b	"	6.99	15.73	"	6.1	& Figure 12c
5a	2855	1.59	3.58	1500	2.7	1969 Figure VI-11e &
5b	"	4.77	10.74	"	6.1	Figure VI-12d
6	3067	7.40	16.65	1300	9.5	1969 Figure VI-15
7	3174	7.15	16.09	1200	9.5	
8a	3289	1.38	3.11	1100	2.7	1970 Figure VI-11f &
8b	"	4.14	9.32	"	6.1	Figure VI-12e

Table VI-1

Parameters used to define ψ and κ for the calculated spectra in this section. The various parameters are described in the text. The k_0 column is used to specify κ in units of $[A.U.^2/sec]$, the k_0' column is used for $[cm^2/sec]$.

the calculated spectrum at Earth with the measured proton spectrum. We find a best fit value for μ of 0.25 ± 0.2. The uncertainty in μ is due to the uncertainty in the value of ψ determined from the measured electron spectra, assuming the median value for the inter-stellar electron spectrum which gives the best fit to the radio data. The reader is again cautioned that the low-energy portions of the interstellar spectra of protons and He nuclei cannot be determined from the spectra at Earth since the calculated spectrum is insensitive to the interstellar spectrum in the region where $\psi > 2.5$. (Examples of contour lines in the r - T plane along which $\psi = 2.5$ are given by the dashed lines in Figure VI-5.)

We calculate the spectra of protons and He nuclei near Earth for the four epochs listed above, using the values of κ and j_D determined as described. These calculated spectra are shown in Figure VI-10. The solid curves correspond to a boundary distance of 2.7 A.U. and the dashed curves, to 6.1 A.U.

In Figures VI-11 and VI-12 we compare the most appropriate (i.e., nearest in time) of these calculated spectra with the measured spectra for 1965 through 1970. We emphasize that the calculated spectra are not best fit curves, they are predictions based on the electron data. In general the agreement between the calculated and measured spectra at Earth is satisfactory for protons for the years 1965 through 1968 and for He nuclei for the years 1965 through 1970. There is typically a turnup or flattening in the measured spectra of both protons and He nuclei at low energies, i.e., below about 10 to 50 MeV/nucleon. This

feature cannot be duplicated without drastic changes in the diffusion coefficient. (See section VI.F.) We attribute the turnup to solar emission and will discuss it in more detail below.

We note another general feature of these comparisons, i.e., that the measured integral intensities of protons above 315 MeV show a relative modulation from early in the solar cycle to late in the solar cycle which is smaller than that predicted by the calculation. The integral fluxes are compared in Table VI-2. This relatively smaller amount of modulation implies that, at some high rigidity, κ increases more rapidly with rigidity than we have assumed. We are unable to make a more quantitative statement because of the lack of detailed high-energy data.

We consider the spectra in Figures VI-11 and VI-12 in detail:
<u>1965</u>: The predicted spectrum of alpha particles is slightly below the measured data points in the region below about 200-300 MeV/nucleon, but the shape is similar. The proton spectrum agrees fairly well with the calculated curve for D = 2.7 A.U. Since the value of ψ is for 1965-1966 and since there is considerable latitude in the high-energy proton data, the diffusion coefficient might be larger in 1965 than the value we have used. In Figure VI-13 we show an improved fit which is obtained by making small changes in ψ. We feel that this change is a quite reasonable extrapolation of the temporal behaviour of ψ. (See entry number 1 in Table VI-1.) The data presented in Figure VI-13 were obtained from a wide variety of detector systems. In view of the possibly large intercalibration problems, the fit may be regarded as adequate.

Model	Year	J_M (p/m^2 sec sr)	J_C (p/m^2 sec sr)	Ratio J_M/J_C
2a	1966	2597 ± 51	2511	1.03 ± .02
3a	1967	2069 ± 51	2061	1.00 ± .02
4a	1968	1794 ± 53	1865	0.96 ± .03
5a	1969	1399 ± 27	1282	1.09 ± .02
6	"	"	1131	1.24 ± .02
7	"	"	1084	1.29 ± .02
8a	1970	1419 ± 42	1078	1.32 ± .04

Table VI-2

The "Model" column refers to the model for the diffusion coefficient used in the calculation, as tabulated in Table VI-1. J_M is the measured integral intensity and J_C is the calculated integral intensity.

<u>1966</u>:   The fit is satisfactory for both protons and He nuclei but the data cover only a small energy range. The measured spectra seem to imply that a boundary distance of 6.1 A.U. is more appropriate than 2.7 A.U., but one must use considerable caution in making such statements since there is quite possibly a substantial solar-emission component to the spectrum at energies up to 50 MeV and since there may well be an intercalibration problem between the different detector systems used. This caution naturally applies to other years as well.

<u>1967</u>:   The measured proton spectrum is slightly higher than the calculated curve for 1968, as one would expect. The shape is similar to that of the 1968 curve but the size of the error bars does not allow a choice between the D = 2.7 A.U. and D = 6.1 A.U. curves. In Figure VI-14 we show a fit to the same data with a value of ψ slightly smaller than the 1968 value (entry number 3 in Table VI-1).

<u>1968p and 1967-68α</u>:   The fit is quite good for both protons and He nuclei, but the statistics of the data are not good enough to allow a choice between the different boundary distances used.

<u>1969</u>:   The fit to the measured spectrum of He nuclei in Figure VI-11d is good, but the statistics and the possibility of solar emission do not allow a choice between the two boundary distances considered. We show the low-energy portion of the spectrum of He nuclei given by Mason (1972)[*]. For the protons, the agreement between the measured and

---

[*]The high-energy portion of that spectrum has not been included from the plot because it is in conflict with our measured integral intensity above 315 MeV/nucleon. We find an integral intensity (see Table V-2) which is about 40% larger than that implied by his differential intensity curve and which is in much better agreement with the calculated spectrum.

calculated spectra is not good and will be discussed further.

<u>1970</u>:   The calculated spectrum of alpha particles is slightly lower
than the measurements but not outside the error bars. The low-energy
portion of the measured proton spectrum shows a considerable enhancement
over previous years which we attribute to solar emission. The spectrum
is also much flatter at high energies than one would expect from the
calculation, as is the 1969 spectrum.

As mentioned earlier the measured spectra show a turnup at low
energies which can be reproduced by the calculation only if we increase
the diffusion coefficient at low energies by more than an order of
magnitude. The diffusion coefficient would then be a decreasing function
of energy (roughly given by $\kappa \propto R^{-2}$) at these energies, in complete
contradiction to the results discussed in sections VI.F.3 and VI.F.4. We
find it preferable to attribute this feature to quiet-time solar emission
of energetic particles. The fact that the measured proton spectra for
1969 and 1970 as presented in Figures VI-11e and VI-11f are flatter than
the calculated spectra, flatter than the spectra from earlier years,
and flatter than the spectra of He nuclei might be explained by solar
emission of protons at energies as high as 50 - 100 MeV. One would ex-
pect solar emission to become a more important component of the spectrum
at solar maximum when the intensity of galactic particles is highly
depressed and when solar emission might well be enhanced.

The difference between the calculated and measured spectra should
give the spectrum of these quiet-time solar particles. The statistical
accuracy of our 1969 data is much better than that of the 1970 data
and will be used to study this point. Such a subtraction procedure is

clearly subject to the criticism that the calculated spectrum shown in Figure VI-11 does not fit well at high energies. A better fit to the measured spectrum can be achieved by increasing the modulation parameter ψ slightly (7% compared to the 13% difference between the values determined from the electron spectra for 1969 and 1970) at all energies and assuming a boundary distance of 9.5 A.U. The change in ψ is important to fit the calculation to the measurements at high energies. The change in the boundary distance causes a slight flattening of the spectrum which improves the agreement between the measured and calculated spectra. The change in ψ can be justified as being due to a slight increase in the modulation from the late June - early July period, when the electron spectra were measured, to the August-September period, when the proton spectrum presented here was measured. Our observations over that period show a decrease of 10-20% (±10%) in the proton intensity in our highest energy bin (235-315 MeV) which is consistent with an increase in ψ over that determined from the electron data. (We did not present the late June - early July proton observations in this thesis because they show clear signs of short-term activity associated with the June 7 flare at energies up to 100 MeV.) In Figure VI-15 we show the measured proton spectrum with the calculated spectrum for the adjusted ψ and with a boundary at 9.5 A.U. (We also present, for comparison, the cal-culated spectrum for a 10% change in ψ, with D = 9.5 A.U.) The fit is clearly much better but the measured spectrum is still somewhat flatter than the calculated spectrum. (The fit to the spectrum of He nuclei with these parameters is changed, but still acceptable. Since the alpha particles have higher rigidity at the same energy per nucleon they are

not so sensitive to changes in ψ or boundary distance as the protons.)

If we wish to explain the difference between the measured and calculated proton spectra in the 30-100 MeV energy range as quiet-time solar emission, then we find (by subtraction of the upper curve) a spectrum for these solar particles which is shown by the squares in Figure VI-15. We have now included the measured spectrum below 10 MeV for comparison. We caution the reader that the proton spectrum is highly variable at energies up to about 30 MeV. (See Figure V-2.) The spectrum shown here is an average over more than 30 days of data. (See Table V-1.) The resulting solar spectrum shows a definite decrease in slope for energies between 10 and 30 MeV. The points above 30 MeV are very poorly defined but they are clearly consistent with such a feature. This flattening is a surprising result since observations of solar-flare spectra have shown a steepening at high energies. On the other hand, a galactic origin for the spectrum at 10 MeV would require an increase in the diffusion coefficient at these energies of more than a factor of 10, which we consider unreasonable. The agreement of the He-nuclei spectrum (and the electron spectrum, by definition) with the calculation lends credence to the calculation. The source of the disagreement for protons may very well lie outside the solar modulation model. Similarly, it is clear that a change in the input spectrum would affect the spectra from the earlier years more than it would the 1969 spectrum, so that such a change again cannot be used to explain the shape of the 1969 spectrum. The suggestion that solar emission of protons is responsible for the flatness of the measured spectrum clearly warrants further investigation, which is outside the scope of this thesis.

The argument that solar emission may be an important contributor to the spectrum is supported by other observations; i.e.,

1) The negative intensity gradient observed by Krimigis and Venkatesan (1969) for energies > 50 MeV/nucleon and the outward streaming observed by Rao et al. (1967), both during relatively quiet times, indicate the existence of continual solar emission at even a much lower level of solar activity than existed in 1969 and 1970.

2) The University of Chicago IMP-5 proton spectrum (Hsieh et al., 1971) is steeper than our OGO-6 proton spectrum. Their spectrum was measured in what may be a slightly quieter period. The agreement between the He-nuclei spectra measured by these two instruments in the energy range 40-315 MeV/nucleon and the agreement between the pαe and IMP-4 (which is very similar to IMP-5) proton spectra in 1967 imply that the differences noted are real time variations and not instrumental effects.

3) Kinsey (1970) has presented a strong statistical argument that solar emission accounts for a large part of the proton spectrum below the turnup in the spectrum, which he observed as high at 80 MeV, again at a time when the Sun was much less active than in 1969.

In summary, we have found that the measured spectra of protons and He nuclei for the years 1965 though 1968 can be understood in terms of a simple model using separable diffusion coefficients with κ independent of radius and with the energy dependence similar to that expected from the power spectra of the interplanetary field. These diffusion coefficients are also (by the means of their determination) consistent with the electron spectra. The general trend of the data seems to imply

an effective boundary for the modulation region within 10 A.U., but this conclusion is based on data which may be affected by solar emission of energetic particles and by intercalibration problems between different detector systems. The statistics of the data do not allow us to distinguish changes in the boundary distance from year to year, but we certainly cannot eliminate such changes. The parameter η clearly increased from 1965 to 1970, as one would expect from, for instance, the neutron - monitor counting rates (see Figure V-1). A pronounced, but not monotonic, increase was observed in the parameter R_0, which characterized the change in slope in the rigidity dependence of the diffusion coefficient. We also noted that this slope seems to have changed at high rigidities over the period discussed (1965-1970).

In order to compare the diffusion coefficient used in this thesis with that calculated by Jokipii and Coleman (1968) from the power spectra of the interplanetary magnetic field, we must take account of the transformation from the spiral angle to the radial direction (Jokipii, 1971) and of the different assumed solar-wind velocities (they used V = 350 km/sec). Their diffusion coefficient may be specified as (Jokipii, 1971)

$$\frac{\kappa_\parallel}{\beta} = \begin{cases} 6.66 \times 10^{-12} & R^2 & R > 2000 \text{ MV} \\ 7.03 \times 10^{-7} & \sqrt{R} & R < 1000 \text{ MV} \end{cases} \left[\text{A.U.}^2/\text{sec} \right]$$

$$= \begin{cases} 1.5 \times 10^{15} & R^2 & R > 2000 \text{ MV} \\ 1.58 \times 10^{20} & \sqrt{R} & R < 1000 \text{ MV} \end{cases} \left[\text{cm}^2/\text{sec} \right]$$

with the power-law segments joined by a smooth curve. The transformation to the radial direction reduces their diffusion coefficient by a factor

of about 0.4 at Earth. A solar wind velocity of 350 km/sec reduces our diffusion coefficient by a factor of 0.875 (to keep κ/V or ψ constant). With these corrections, our diffusion coefficient, at, for example, 1000 MV, is roughly 1/3 of that of Jokipii and Coleman if we assume a boundary distance of 2.7 A.U. (using entry number 1a in Table VI-1). Using a boundary distance of 6.1 A.U. (entry number 1b) we find a diffusion coefficient essentially equal to that of Jokipii and Coleman (at 1000 MV).

The measured proton spectra for 1969 and 1970 do not fit very well to the calculated spectra based on the values of ψ determined from electron spectra but the spectra of He nuclei do. For these reasons, and the other reasons outlined above, we conclude that solar emission may be important at relatively high energies in 1969 and 1970, but further study is clearly required.

It should be clear from the discussion in Section VI.F that we cannot argue that the good agreement for the bulk of the data prove that any of our assumptions are valid (i.e., that κ is independent of radius or that D = 2.7 A.U. or 6.1 A.U. or that $j_D \propto (W - 0.25m)^{-2.65}$. It can be said that these assumptions are sufficient to provide good agreement between the measured and calculated spectra, especially for the years 1965 through 1968, without complications such as the non-separable diffusion coefficients, which some authors have argued were necessary for those years (Burger, 1971; Burger and Swanenburg, 1971) or the different input spectra for protons and He nuclei used by Lezniak and Webber (1971) and Urch and Gleeson (1972). We repeat for emphasis:

We do not argue that the input spectrum has some particular shape or that some particular functional form is necessary for $K(r,T)$. We do not argue that K is a separable function; but, simply, that a separable function is sufficient to reproduce the measured spectra. (We have found it necessary to change the energy dependence of K with time, but this measure seems to be well justified. See, for example, Stoker and Carmichael (1971)). We do not argue that the interstellar proton and He-nuclei spectra have the same shape; but that, if care is used in the choice of $K(r,T)$, similar interstellar spectra for protons and He nuclei are sufficient to reproduce the measured spectra at Earth.

VII. SUMMARY

In this thesis we have described measurements of the differential energy spectra of cosmic-ray protons and He nuclei for a substantial portion of the solar cycle at energies up to 315 MeV/nucleon. These measurements were made with identical satellite- and balloon-borne detectors. The extensive calibrations of the instruments and the much improved calculations and measurements of atmospheric secondary production allow considerable confidence in the reliability of these spectra.

The cosmic-ray spectrum in this energy range is dominated by the effects of solar modulation and we have studied this phenomenon, using as tools the measured spectra and numerical solutions of the transport equation for galactic cosmic rays in the interplanetary medium. We have investigated:

1) certain characteristics of the transport equation which hold for a wide range of parameters.

2) the properties of the parameters of the transport equation, in particular the diffusion coefficient, K.

3) the interstellar spectra, which served as boundary conditions in the solution of the transport equation.

We have shown that the "modulation parameter",

$$\psi(r,T) = \int_{r}^{D} \frac{V dr'}{K(r',T)} \qquad (VI-5)$$

is very useful for studies of solar modulation. This parameter is used to define the regions of applicability of several analytic approximations to the solution of the transport equation, i.e., the diffusion-convection

approximation, the power-series approximation, and the force-field

approximation. The force-field model was found to be useful for weak

modulation (small ψ). It is quantitatively correct only for $\psi \stackrel{<}{\sim} 0.1$.

It still has roughly the proper radial and energy dependence for ψ in

the range, $0.1 \stackrel{<}{\sim} \psi \stackrel{<}{\sim} 2.5$, but for $\psi > 2.5$ it is no longer applicable.

As one would expect from any of these three approximations, the

solution to the transport equation for small ψ, i.e., $\psi < 2.5$, is fairly

well determined by ψ alone (plus, of course, the interstellar spectrum,

j_D (T). That is, for ψ in this range (several examples of contour lines

along which $\psi = 2.5$ are given in Figure VI-5), the spectrum at Earth is

related to the interstellar spectrum by a function of ψ only, which may

be accurately determined by numerical calculations or more crudely

determined by one of the approximations mentioned above. This dependence

on ψ alone means that we cannot determine separately the diffusion

coefficient, κ, the boundary distance, D, or the interstellar spectrum,

j_D, from the measured spectra of high-energy protons and He nuclei.

Given good measurements of the high-energy spectra for several years,

limits might be placed on these quantities since κ and D are presumably

time dependent, while j_D should not be time dependent.

For $\psi > 2.5$ the situation is quite different. For a wide range

of interstellar spectra and diffusion coefficients the calculated inten-

sities decrease at lower energies and the spectrum at Earth has, at least

roughly, a shape given by $j = AT$. The solution in this $\psi > 2.5$ region

is not very sensitive to ψ or to the interstellar spectrum, but it is

strongly affected by the radial dependence of κ, especially for

$r \stackrel{<}{\sim} 1$ A.U. Contour plots of the phase-space density were presented as a

suitable graphic means of explaining the behaviour of the proton spectrum at low-energies. Three important points were made about the behaviour of the low-energy portion of the proton spectrum.

1) Since the low-energy proton spectrum is sensitive to the radial dependence of the diffusion coefficient, it may be used as a tool to study that radial dependence.

2) Since the low-energy proton spectrum is not sensitive to the value of ψ at the corresponding rigidity, other means must be used to determine this parameter. In particular, we mentioned that the electron spectrum can be used to determine ψ.

3) Since the calculated spectrum is insensitive to the low-energy portion of the interstellar spectrum, the measured spectrum of protons at Earth cannot be used to determine the interstellar spectrum of low-energy protons.

Since the spectra of protons and He nuclei at 1 A.U. alone cannot provide enough information to completely define the problem, we briefly described how other measurements could be used to study solar modulation. The construction of more complicated models would be greatly aided by precise measurements of spectra at Earth at high energies, spectra at larger distances from the Sun, radial gradients and anisotropies. Such measurements would allow construction of more detailed models including such possibilities as non-separable diffusion coefficients, tensor diffusion coefficients, and non-spherical geometry. The current status of the observational data does not justify such refinements.

The obvious test of the validity of these general observations on the properties of the modulated spectrum of galactic protons and He nuclei is a comparison between the calculated and measured spectra. This comparison was made in section VI.G. The calculated spectra were based on values of ψ derived from electron data and on input spectra which gave good fits to the spectra measured near Earth in 1968. The fact that the measured proton spectra for 1965 through 1968 and the He-nuclei spectra for 1965 through 1970 fit these calculated spectra implies that the simple forms used for the diffusion coefficient and the interstellar spectra in this work are sufficient to explain the measured spectra with the current uncertainties in the measurements.

The values of ψ used were tabulated and discussed in Chapter VI. These values of ψ were related to the diffusion coefficient by the use of a simple model in which the diffusion coefficient is independent of radius within a given boundary distance and infinite beyond that distance. This allows us to describe the radial dependence of the diffusion coefficient by a single parameter, the boundary distance, D.

It was shown that the spectrum of low-energy galactic protons at Earth may be related to the value of D. In particular, we discussed two ways in which spectra steeper than $j = AT$ might be produced.

1) If the diffusion coefficient is largely independent of radius near 1 A.U. (as we have assumed) and if the boundary is relatively nearby, then the proton spectrum will be steeper than $j = AT$.

2) If the diffusion coefficient decreases inside 1 A.U., then the spectra will be steeper than $j = AT$.

The fits to the proton spectra presented in Figures VI-1 and VI-11 are slightly steeper than $j = AT$ for 1965 through 1968. For those years, at least, we may infer that either 1) or 2) above is a valid description of the radial dependence of the diffusion coefficient. If we exclude the second possibility on the basis of the results of Lupton (1971) and Sari (1972) then one may conclude that the effective boundary is within about 10 A.U. (for the years 1965 through 1968). This conclusion is clearly tentative since the statistics of the data are poor, but it is also clear that more precise measurements of the proton spectrum would allow one to derive values of D from local measurements.

The diffusion coefficient used to fit the 1965 data is in reasonable agreement with that determined from the power spectrum of the interplanetary magnetic field (Jokipii and Coleman, 1968) for roughly the same period. We find roughly a factor of 3 change in ψ from 1965 to 1970, in contrast to the assertion of Mathews et al. (1971) that the power spectra of the interplanetary magnetic field have not changed over that period. If more detailed study of the power spectra confirms this hypothesis, then the changes in ψ will have to attributed to changes in the boundary distance.

The interstellar spectrum used was of the form $j_D \propto (W-\mu m)^{-2.65}$ for both protons and alpha particles. By comparing calculated and measured proton spectra for 1968 we found a value for μ of roughly $\mu = 0.25 \pm 0.2$, assuming the values of ψ determined from the electron data as discussed in Section VI.G (but the interstellar spectra below about 100-200 MeV cannot be determined in this manner).

In order to explain the shape of the 1969 (and 1970) spectrum we

found it necessary to invoke the existence of solar emission of protons at energies up to 50-100 MeV. The fit was improved by assuming a boundary distance of 9.5 A.U., which is somewhat larger than was used for the earlier years.

In summary, we find agreement between the calculated and measured spectra which is generally better than in previous investigations. We attribute this generally good agreement to the particular selection of boundary distance in the range used, a range which was suggested by our current understanding of the propagation of solar-flare protons. Some slight further improvement of the fits may be gained by changing the boundary distance from year to year. Even with the larger boundary distance the 1969 (and 1970) proton spectrum has a small excess at energies up to about 100 MeV. We have argued that the excess may well represent solar emission even though this solar spectrum appears to flatten somewhat at higher energies.

APPENDIX 1

The Relation Between the Range-Telescope Counting Rate and

Particle Intensity: Derivation and Verification

The equation

$$\vec{j} = \frac{\bar{\bar{R}}^{-1} \cdot \vec{N}}{\tau} \qquad (IV-1)$$

was specified earlier as the relation between counting rate in the range

telescope and particle intensity. In this appendix the terms in

equation IV-1 will be defined with more detail, the methods by which the

values of these terms were determined will be discussed, and the

verification of these values by calibration will be described. Briefly,

the method of data analysis is as follows: Bins are defined by range

(determined by which detectors are triggered) and energy-loss (PHA's in

D1, D2, and D3, high discriminators in D4 - D7) criteria; and a vector,

$\vec{N}$, is defined which has components, N_i, given by the number of events

which meet those criteria for the i'th bin (or the number of events in

the bin) in a time τ. $\vec{j}$ is a vector with components, j_i, which represent

the intensity in the i'th energy interval with median energy E_i and

width ΔE_i. $\bar{\bar{R}}$ is a matrix which takes into account the geometrical

factor, G, the width of the energy interval, ΔE, and the corrections

due to statistical fluctuations in energy loss and nuclear interactions

in the absorber stack.

For low-energy particles ($\stackrel{<}{\sim}$ 50 MeV/nucleon) the corrections

mentioned above are small and may be neglected. In this case the $\bar{\bar{R}}$

matrix is diagonal and the low energy data were converted to spectra

using the simple form

$$j_i = \frac{N_i}{G_i \; \Delta E_i \tau} \quad .$$

(IV-2)

A. Two Dimensional Plots and Bins

In this section we show how the range and energy-loss measurements are used to define bins. These bins are illustrated graphically by two-dimensional pulse-height distributions called 2-D plots. There is a separate 2-D plot for each useful combination of detectors and high discriminators triggered. The notation used to label these plots indicates the deepest detector penetrated (called the range) and the restrictions on the high discriminator. For instance, the Range 5 HH (or R5HH) plot has on it events which triggered D2, D3, D4, and D5 (possibly also D1) with the D4 and D5 high discriminators. R6XHH means D2 - D6 were triggered; the D5 and D6 high discriminators were triggered; and no restriction was placed on the D4 high discriminator. R4L means D2 - D4 were triggered and the D4 high discriminator was not triggered. Table A1-1 shows which plots were considered in defining the bins.

Figure A1-1 shows a plot of average energy loss in D2 versus average energy loss in D3 for protons and alphas with the deepest detector penetrated marked as a parameter along the curves. Note the segments of the curves marked D5. These segments correspond to Range 5 events. Figure A1-2 shows the Range 5HH plot. The number of events with a given D2 and D3 pulse height is shown as a function of the D2 and D3 pulse heights. The previously mentioned segments of the D2 versus D3 plot in Figure A1-1 are shown again in this plot. Also indicated are the energy-loss boundaries of the proton and alpha - particle bins. Thus the Range 5HH proton bin (which is bin number 4) can be completely described as those events which trigger D2, D3, D4 and D5 but not D6 or D7; trigger the D4 and D5 high discriminators; and have

Plot Type	Comments
R1	low energy p and He
R2	bins - a variable, sometimes large
R3	number of bins per plot
R4H	3 proton bins 3 He bins for OGO-6 2 He bins for pαe
R4L	1 electron-meson bin used for background correction
R5HH	1 proton bin, 1 He bin
R6XHH	1 proton bin
R6HHH	1 He bin
R7XXXX	1 proton bin
R7HHHH	1 He bin

Table A1-1

List of types of 2-D plots and bins. The notation is explained in the text.

D2 and D3 pulse heights within the bounds indicated in Figure A1-2.

B. Effective Time

Dead time during the pαe flight is typically ~10%; data loss due to problems in recording and transferring the data to the FORTRAN compatible tapes is ~5%. The data from the rate scalers allow us to correct for these effects. Since the rate scalers have a negligible dead time, they record the total number of events during a given time interval. We replace the length of that time interval, Δt, with an effective time, τ, given by

$$\tau = \frac{\text{number of analyzable events}}{\text{total number of events}} \cdot \Delta t.$$

τ is used in all flux computations. It should be noted that data transmission errors occasionally change a rate bit. Since these bits are read out with each analyzed event and normally change only after ~100 events, we have an extremely redundant readout and can easily find and correct such errors.

C. Calculation of Intensities

We define a response function, $\mathcal{R}_i(E,\lambda)$, as the probability that a particle of species λ and energy E will trigger an event which meets the requirements to belong to bin i. Let $j(E,\lambda)$ be the differential energy spectrum (intensity) of λ particles and N_i be the number of events falling into bin i in an effective time τ. Then

$$\frac{N_i}{\tau} = \sum_\lambda \int dE \; \mathcal{R}_i(E,\lambda) j(E,\lambda) \quad . \tag{A1-1}$$

The detector design allows us to choose bins such that only one species contributes to a given bin, hence the summation of λ can be dropped. If we make the (trivial) assumption that, in a given energy interval with center at E_n and width ΔE_n, the intensity j can be represented by a power law in E with exponent γ_n and coefficient C_n, then the following definitions are appropriate:

$$j(E) \simeq C_n E^{\gamma_n} \text{ by assumption in the n'th energy interval.}$$

and

$$j_n = C_n E_n^{\gamma_n}$$

and

$$R_{in} = \int_{\Delta E_n} \mathcal{R}_i(E) E^{\gamma_n} \, dE / E_n^{\gamma_n} \quad .$$

If we substitute these definitions into equation A1-1 we get

$$\frac{N_i}{\tau} = \sum_n R_{in} \, j_n$$

or

$$\frac{\vec{N}}{\tau} = \overline{\overline{R}} \cdot \vec{j}$$

which may be inverted to give the desired result, equation IV-1. Note

that $\bar{\bar{R}}$ is a function of the γ_n's only. The data were analyzed by assuming a set of γ_n and determining $\vec{j}$ from equation IV-1. If the resultant $\vec{j}$ is not consistent with the γ_n, the procedure was repeated until a self-consistent $\vec{j}$ was found. The dependence of $\bar{\bar{R}}$ on the γ_n is small for γ_n in the range 0 to +1, which is appropriate to the spectra we measured.

D. The Response Function

The function $\mathcal{R}_i(E)$ was determined by folding together six functions which are briefly described below, and treated in more detail in the following paragraphs. $C(m_2, m_3, E)$ is the probability that a particle of energy E will have an energy loss in channel m_2 in D2 and channel m_3 in D3.

$F_{non}(K, E)$ is the probability that a particle of energy E stops in range K due to its ionization energy loss, without having undergone a nuclear interaction.

$F(J, K, E)$ is the probability that a particle of energy E will undergo a nuclear interaction in range J and stop in range K.

$H(K, E)$ is the probability that a non-interacting particle of energy E will trigger the high discriminator of detector D_K.

$H'(J, K, E)$ is the probability that a particle which interacts in range J will trigger the high discriminator of detector D_K.

$G(K, E)$ is the geometrical factor for a particle of energy E which stops in range K.

Consider, for example, bin 4, which consists of R5HH events which fall into a specified area (S_4) on the 2-D plots (the area illustrated in Figure A1-2). The response function, $\mathcal{R}_i(E)$, for bin 4 is given by

$$\mathcal{R}_4(E) = [F(3,5,E) \ H'(3,4,E) \ H'(3,5,E) + F(4,5,E) \ H(4,E) \ H'(4,5,E)$$
$$+ (F(5,5,E) + F_{non}(5,E)) \ H(4,E) \ H(5,E)] \ \cdot \ G(5,E) \ \cdot$$
$$[\Sigma_{S_4} \Sigma \ C(m_2, m_3, E)] \tag{A1-2}$$

$$= P(5,E) \ \cdot \ G(5,E) \ \cdot \ C_4(E) \tag{A1-3}$$

$F(1,5,E)$ and $F(2,5,E)$ are ignored since they are very small and since any particle which interacts in D1, D2, or D3 is unlikely to fall in S_4 because the interaction products will change the energy loss.

$P(5,E)$, defined by the equations above, is the probability that a particle will stop in R5 and trigger D4H and D5H. $C_4(E)$ is the probability that a particle of energy E will have energy losses in D2 and D3 inside the limits imposed by the area S_4 on the 2-D plots.

The energy loss distribution $C(m_2, m_3, E)$ is calculated by the Space Radiation Lab program "CROSS" which is based on the work of Symon (1948). The fluctuations in the energy loss in detectors D2 and D3 are assumed to be uncorrelated; hence, the (continuous) two-dimensional distribution is simply the product of two one-dimensional distributions. $C(m_2, m_3, E)$ is a discrete representation of this continuous distribution which is obtained by integrating over the small rectangle in the two-dimensional D2, D3 space defined by the widths of channels m_2 and m_3. Calibrations of the pae gondola made at NASA's Space Radiation Effects Laboratory (SREL) in 1968 have confirmed the validity of these distributions. A comparison of predicted and measured energy loss distributions in D2 is shown in Figure A1-3.

$F(J,K,E)$ and $F_{non}(K,E)$ are derived from a Monte Carlo calculation ("FLINT"), described in the following section, which traces trajectories of incoming particles and of secondaries from an interaction. Extensive accelerator calibrations using both protons and alpha particles confirm the predictions of the FLINT program. The calibrations are described in Section F of this appendix.

$H(K,E)$ is determined by integrating the Symon's energy-loss probability distribution above the threshold of the high discriminator of D_K. With the threshold settings in use on $p\alpha e$ and OGO-6, $H(K,E)$ for all ranges K is almost 100% for E; less than about 300 MeV for protons. It falls rapidly to a value of 20% - 30% at ~400 MeV and falls off more slowly at higher energies. Helium nuclei always trigger the high discriminators.

$H'(J,K,E)$ is assumed to be one for any particle which stops in the stack, i.e., which does not trigger D7. The reason for this is that a proton (or meson) which has an energy small enough to stay within the stack must have an energy loss large enough to trigger the high discriminators. Electrons would violate this assumption but are not produced in any significant number at the energies ($\lesssim$ 400-500 MeV) we are concerned with. Even if produced, electrons would almost always trigger D8 because they are scattered so easily.

$G(K,E)$ is calculated for non-interacting protons (for which the range K is determined from E by the range-energy relationship) by a numerical integration over the areas and subtended solid angles of the several discs which define the geometrical limits of a particle trajectory. The upper discs are D2, D3 and the opening in the top of D8; the lowest disc is the cross-section of the absorber stack at the range corresponding to the energy E (or the opening in the bottom of D8). The range detectors define intermediate discs through which the trajectory must pass. For interacting protons the geometrical factor is approximated by the average geometrical factor for that range as calculated for non-interacting particles.

Note that if we omit the summation over the area S_4 in equations A1-2 and A1-3 we can use the response function to predict the two-dimensional distribution of events on a 2-D plot. This can be compared to measured distributions as a further check on the validity of the response function.

Since it is difficult to compare graphically two 2-D plots, the comparison has been made using one-dimensional distributions which are found by collapsing the two-dimensional distributions onto the diagonal. All events falling into a band of specified width (wide enough to contain ~90% of the events) are plotted as a function of the lesser of their pulse heights in D2 and D3. This type of plot is much more easily read than a 2-D plot, and preserves some of the improved resolution given by a double measurement of energy loss. An example is shown in Figure A1-4. The dashed line is the predicted response to "stopping" protons, those with energies between 156.5 and 235 MeV which would stop in R5 if they did not interact. The dotted line is the response to "interacting" protons, those with energies of > 235 MeV which should have been R6 or R7 events. (The response to protons of E < 156.5 MeV is zero.) The solid line is the sum of these curves and should be compared to the histogram which represents measured data from the $p\alpha e$ balloon flights 67C1P and 67C3P. Plots of this type were useful in determining where the boundaries of the bins should be placed to include as many stopping particles as possible while excluding interacting particles, i.e., to minimize the ratio of off-diagonal elements of $\bar{\bar{R}}$ to diagonal elements.

E.   The FLINT Program

The FLINT program calculates the functions $F(J,K,E)$ and $F_{non}(K,E)$, which represent the effect of nuclear interactions in the stack.   Figure Al-5 illustrates some of the types of interaction events which must be considered.   The trajectory A is a non-interacting particle which stops in A5 and is therefore an R5 event.   This type of event contributes to the probability $F_{non}(5,E)$.   B shows a particle which interacts in A4 and has a prong leaving the stack, thus triggering D8.   This event would not be recorded.   In events C and E we have examples in which the prongs do not leave the absorber in which the interaction took place.   C is an R5 event and E is an R4 event, even though both may represent, for example, a 200-MeV proton.   Event E contributes to $F(4,4,E)$ and C to $F(5,5,E)$.   D is the sort of event which contributes to $F(5,6,E)$.

The FLINT calculation is done using Monte Carlo techniques and is based on cross-sections collected from emulsion data and Monte Carlo intranuclear cascade calculations.   Input data to the program consist of a geometrical description of the telescope and an interaction length; multiplicities of "gray" and "shower track" secondaries as functions of energy; energy distributions of gray and shower tracks; angular distributions of gray and shower tracks; and a neutron D8 probability.   For incident alpha particles "straight-on" probabilities are also input.

Gray tracks are primarily secondary protons and are treated as protons in FLINT.   Shower tracks are primarily pions and are treated as such in FLINT.   The terminology originates with the emulsion measurements.

The interaction length is determined by the accelerator cali-

brations described in the next section; the percentage of particles stopping in the proper range without triggering D8 depends strongly on the interaction length and very little on the other distributions. This interaction length is 158.4 gm/cm^2. It is somewhat shorter than the accepted value of ~195 gm/cm^2 for tungsten (Chen et al., 1955) but it represents an effective interaction length in a complicated system so we do not regard this as a serious discrepancy.

Gray-track multiplicities were originally based on the data given by Powell et al. (1959), but these multiplicities did not fit our calibration data; they were too small. We were able to fit our data best with a curve roughly midway between the multiplicity data given by Metropolis et al. (1958a;b) for A = 180 (e.g., tungsten) and the Bertini (1967) data for Pb. Figure A2-3 includes a comparison of the emulsion data with intranuclear cascade multiplicities for heavy elements. The differences among these curves, even allowing for the differences in the definitions of gray and shower tracks and cascade protons, seem to indicate a real discrepancy. The shower-track multiplicities given by different authors agree within statistics and we use this function as given. For both gray and shower tracks the actual multiplicity in an interaction is assumed to be an integer; these integers are assumed to have a Poisson distribution which has an average given by the input data curves.

The energy distribution of gray-track secondaries is $E^{-1.2}$. This function is assumed to be valid for all primary energies; all multiplicities; all secondary angles, etc. The distribution is cut off

at the primary energy. Figure A1-6 shows the Camerini et al. (1950) and Metropolis et al. (1958a;b) data. The shower-track secondaries are assumed to have an E^{-1} energy distribution and are also shown in Figure A1-6.

The gray-track polar-angle distribution which we used was

$$\frac{dn}{d\theta} \propto \sin(\theta) \exp(1.959 \cos\theta)$$

and the shower-track angular distribution was

$$\frac{dn}{d\theta} \propto \sin\theta \, (4.027 \times 10^{-2} e^{28 \cos\theta} + 0.0175 e^{4.8 \cos\theta} + .1771 e^{.3 \cos\theta}).$$

The gray-track angular distribution is from a fit to the Bertini (1966) data; the emulsion data were less forward peaked and did not fit our calibration data as well. The shower-track angular distribution is from a fit to the emulsion data (Powell et al., 1959).

The possibility that an evaportation neutron from an interaction might produce a knock-on proton in the plastic scintillator ($\sim$50% H by number) of the D8 counter was included. The probability of such an event was estimated by integrating over the evaporation-neutron spectrum (Bertini, 1966) and the p-n cross-section (Chen et al., 1968) as a function of energy, assuming that $d\sigma_{pn}/dE_p$ was constant for $E_p < E_n$. The probability of such an event was found to be roughly proportional to $E^{.05}$ and is about 10% at E = 500 MeV, where E is the primary energy. The pulse-height analysis of D8 mentioned in Section A1.F was performed because of concern that these neutrons might cause a steeply falling energy loss spectrum in D8.

For alpha particles the same angular and energy distributions were used as for protons. All multiplicities were increased by a

factor of 1.6 (this factor was expected to be between 1 and 2 based on emulsion data (Ceccarelli et al., 1955; Deutsch, 1955, Quareni and Zorn, 1955; Willoughby, 1956; Jain et al., 1959a;b), and was optimized to fit our calibration data). The interaction length was determined from the accelerator runs as with protons. It had a value of 117 gm/cm^2. The major difference in alpha-particle interactions is that in ~30% of the interactions there is a "straight-on" secondary; that is, a secondary leaves the interaction with the same velocity and in the same direction as the original alpha particle. This phenomenon has been observed in emulsions by Appa Rao (1956, 1961) and others (Quareni and Zorn, 1955); it is also quite evident in our calibration data. If this "straight-on" secondary is a deuteron or triton then the secondary can penetrate to a deeper range than the primary alpha particle would have reached -- this feature is observed for alpha particles, but not for protons. The probabilities of "straight-ons" per interaction which give the best agreement with our calibration data are:

protons	0.125
deuteron	0.090
triton	0.045
He^3	0.045

The results of the calculation for the accelerator telescope are plotted as solid curves in Figures A1-7 and A1-8, with the accelerator calibration data shown as points. The curves for the pαe or OGO-6 telescopes are almost identical to that of the accelerator telescope since considerable care was taken to ensure that the geometry

and mass distribution were the same for the three telescopes.

The cross-section data used in the FLINT calculation are fairly crude, especially in comparison with the elaborate specification of cross-sections in the atmospheric secondaries program (ATSEC) described in Appendix 2. The three most important reasons for this are:

1) The geometry is much more complicated than in ATSEC. Including both complicated geometry and complicated cross-sections would have made coding difficult and execution expensive.

2) The results needed are simpler than in ATSEC -- deciding if a detector was triggered or not requires less information than calculating a spectrum.

3) The program gave the right answer, as verified by the calibrations.

F. Calibration of the Range Telescope

The FLINT program, described in the preceding section, calcu-
lates interaction corrections for the range-telescope data on the basis
of nuclear cross-section data. Since these cross-sections are not very
well-known, accelerator calibrations of the range telescope were
considered necessary. The pαe gondola was calibrated on the proton beam
at NASA's Space Radiation Effects Laboratory (SREL) in 1968, at energies
from ~60 MeV to ~600 MeV. These calibration runs are the source of the
measured energy-loss distributions with which we have checked the Symon's
distributions used in the calculation of the C and H functions. The
minimum, reliable beam intensity we were able to achieve at that time,
however, was still high considering the time resolution of the instrument
electronics. Particle "pileup" problems were noted in D8 which is much
larger than D1 - D7. Furthermore, the data-recording rate was too small
to allow collection of enough events for the 1% statistics desired. For
these reasons, a special prototype of the instrument was constructed
which was geometrically identical to the pαe and OGO instruments, but
with much better time resolution and much higher data-recording rate.

This prototype was calibrated with protons at SREL at 7
energies from 115 to 570 MeV and with alpha particles at the Lawrence
Radiation Laboratory in Berkeley at 188 and 213 MeV/nucleon.

A schematic of the instrument is shown in Figure A1-9. The
solid state detectors have been replaced with discs of NE-102 plastic
scintillator material with radii and thicknesses equal to those of the
replaced SSD's. The light was piped to the photomultiplier tubes by

thin strips of lucite about 25 cm long. To allow space for these light pipes without changing the telescope geometry, it was necessary to construct D8 of two pieces which overlapped so that they subtended the proper angles. The two pieces of D8 were referred to as D8α and D8β. Since we were concerned with measuring particle trajectories without regard to energy loss in D1, D2, or D3 (having already made energy-loss distribution measurements in the 1968 SREL accelerator runs), it was possible to combine D1 and D2 into a single detector D12. By using scintillators and refraining from doing a pulse-height analysis, we were able to use fast electronics composed primarily of NIM standard modules.

The layout of the experiment is included in Figure A1-10. The beam was defined by counters A1, A2, and B. B had a 1/2" diameter hole in its center and was in anticoincidence with the A counters. A1 was 1-1/2" in diameter, A2 was 2" in diameter, both were 1/4" thick. A3 and B were 8" x 8-1/2" x 3/8". A3 was included in the $\overline{AB}$ coincidence to help prevent accidental coincidences; its main purpose, however, was to guard against a "pileup" or accidental coincidence between a particle in the beam and one several inches off the beam. One of its outputs was connected to a "Pileup Gate" which signaled if it received two pulses within a preset time (100 ns).

Figure A1-10 is a block diagram of the electronics. There were two almost independent data systems. One consisted entirely of NIM logic whose output was recorded in visual display scalers. This system allowed on-line monitoring of the experiment. A1, A2, A3, D12, and D3

were in coincidence, with B in anticoincidence to form a trigger signal which initiated analysis of an event. D4, D5, D6, and D7, or their logical complements, were fed to a coincidence gate to determine the range requirement. For example, if one wished to know what fraction of events were R5, the R coincidence requirement was D4D5$\overline{\text{D6}}$D7. To analyze a different range event the inputs to the R coincidence gate were manually changed and another run made. The D8 signal was formed by the logical or of D8α and D8β. A3 was fed to the pileup gate as mentioned before and the not-pileup signal ($\overline{\text{P}}$) gated the signals fed to the scalers.

The parallel data system recorded data directly from the discriminators. The signals from D4, D5, D6, D7, D8α, and D8β were gated by the $\overline{\text{TP}}$ signal from the NIM system. The outputs from this gate were fed to a buffer-interface system and recorded on magnetic tape.

In addition to the systems described above, D8α or D8β was pulse-height analyzed during some runs. This analysis was done because of concern over the fact that a sharply falling energy-loss spectrum in D8 would cause the percentage of events triggering D8 to be strongly dependent on discriminator threshold setting. It was confirmed, in fact, that the D8 spectrum is roughly flat out to many times the discriminator threshold level so that the D8 percentage is insensitive to threshold setting.

The results of these measurements are shown in Figures A1-7 and A1-8 along with the predictions of the FLINT program.

The beam energies were measured by measuring particle ranges

with a variable-thickness absorber. In order to preclude the possibility that low-energy contamination of the beam might be present, we studied the energy-loss distribution as well as the range distribution of the beam and found no evidence of any such contamination.

APPENDIX 2

Production of Secondary Protons

in the Atmosphere

In 1969 and 1970 simultaneous measurements of the differential

energy spectra of protons (which included a small contribution from

unresolved deuterons and tritons) up to 315 MeV were performed with the

$p\alpha e$ instrument, flown on balloons from Fort Churchill, Manitoba, and the

OGO-6 instrument, in polar orbit. This joint experiment was the first

to make simultaneous measurements over a large energy range with

identical instruments. These data, which include the spectra at the top

of the atmosphere, make it possible to study the production of

atmospheric secondaries with more accuracy than was previously possible.

In order to carry out this study we have made extensive calculations

of this production.

Our calculation uses a Monte Carlo method based on the nuclear

cross sections for protons in 0^{16} and other elements as calculated by

Bertini (1963, 1966, 1967, 1969) and others (Alsmiller and Barish, 1968;

Bertini and Guthrie, 1970) at Oak Ridge. Previous calculations have

used numerical integrations of simplified forms of a transport equation

with cross-sections measured in nuclear emulsions (except see Alsmiller

and Boughner (1968)). In this appendix, we shall discuss briefly some of

the previous calculations of other investigators; describe our own

calculation and the cross-sections upon which it is based; and compare

the results of previous calculations with our improved results.

A. Previous Calculations

Previous atmospheric-secondary calculations have been of two
types. The simpler case was when emulsion measurements of secondary
production were used to correct emulsion measurements of particle flux.
The more complicated case involved the use of cross sections derived
from measurements made in emulsion to correct particle fluxes measured
with counter telescopes.

Fichtel et al. (1964) and Freier and Waddington (1965, 1968)
have used emulsion data to calculate secondaries which are then used to
correct their cosmic-ray fluxes measured with emulsions. In these cases
the secondaries can be evaluated from data measured on the same flight
and in the same emulsions in which the total fluxes are measured. If
this technique is used, it is not necessary to determine the producing
spectrum; and scanning inefficiencies and such problems will tend to
cancel out. One must, however, make corrections to the data for
differences in the emulsion and air cross-sections; this has
typically been done by multiplying by a single normalization factor,
which is evaluated by comparison with cross-sections from nuclear-cascade
calculations. Emulsion data typically are available only in small
quantities, leading to problems with statistical fluctuations. A more
complicated calculation is necessary when emulsion data are used to
calculate corrections for spectra measured with counter telescopes as
done first by Vogt (1962) and recently by Rygg and Earl (1971).
In these calculations, the response function determined from the
published emulsion cross sections must be folded with a producing

spectrum, which is not very well known. Scanning inefficiencies may introduce serious absolute errors and the correction for the differences in air and emulsions must still be made. Vogt, in the earliest calculation of this type, included the attenuation of the primary spectrum and the production of secondaries by secondaries in a crude fashion by using the data of Lord (1951) to define the producing spectrum. Rygg has assumed a constant producing spectrum, or "source function." The published, emulsion cross-section data are not very detailed and effects such as the change in angular distributions of secondaries with primary and secondary energy are not well defined because the statistical accuracy is insufficient.

B. Method of Calculation

Our experience in doing the FLINT calculations of interaction corrections in the range-telescope stack (described in Appendix 1), and in comparing them with accelerator calibrations caused us to distrust the emulsion data. This fact, combined with the lack of detail in the emulsion cross sections, led us to decide to use other available cross-section data. The data published by Bertini and his co-workers at Oak Ridge (Alsmiller and Barish, 1968; Bertini, 1963; Bertini, 1966; Bertini, 1967; Bertini, 1969; Bertini and Guthrie, 1970) form the most detailed and comprehensive set of cross-section data available and these data have been used in the calculation described below. Since these data are much more detailed than the emulsion data and, since we wanted to make our model as detailed as necessary, a Monte Carlo technique was most appropriate to do the calculation. It would be very difficult even to write down a transport equation including effects such as production of secondaries by secondaries and change of producing spectrum with depth -- to solve such an equation would, of course, be even more difficult.

Figure A2-1 is a schematic representation of proton and alpha-particle cascades in the atmosphere. It illustrates the physical model upon which our calculation is based. The Monte Carlo program, called ATSEC, begins by generating a primary proton or alpha particle, which is incident upon the top of the atmosphere at a specified energy and with an angle of incidence generated from a random number in a manner designed to reflect an isotropic distribution over the upper hemisphere.

This particle is traced until it stops due to ionization energy loss, or interacts. If it interacts, secondaries are generated according to the cross-sections and each secondary is traced as was the primary. The process is repeated with each interaction until all particles generated have either stopped or left the atmosphere. The ATSEC program writes on magnetic tape a description of each particle containing its order, type, energy, range, polar angle, and starting and stopping depths. Order is 1 for primaries, 2 for secondaries, 3 for tertiaries, etc. Type is proton, neutron, deuteron or alpha particle. The "energy" is evaluated at the beginning of the particles path, and the "range" is the ionization energy loss range of a non-interacting particle corresponding to this energy. The secondary spectrum at any given depth is calculated by counting all the particles which cross that level and assigning them to bins according to order, type, energy, angle, and energy and type of the primary. The counts in the appropriate bins are then multipled by a weighting factor, k, which reflects the spectrum at the depth of interest.

The weighting factor is derived by knowing the number of primaries incident at the top of the atmosphere in a given energy interval, N_o $(E, \Delta E)$, (this number is part of the input to ATSEC and is picked to be large enough that statistical fluctuations will not be important; it is typically 1000 for an energy interval of 5%) and by knowing (by assumption) the intensity of primaries, j_p, at the top of the atmosphere. Thus, if N_p $(E, \Delta E, \theta, \Delta \theta, \tau)$ is the flux of primaries at

a depth τ in the atmosphere with energy between E and E + ΔE and polar

angle between θ and θ + $\Delta\theta$, there exists a factor k'(E) which relates

N_p to j_p by j_p (E + 1/2ΔE, τ) = $\dfrac{N_p \ (E, \ \Delta E, \ \theta, \ \Delta\theta, \ \tau) \ \cdot \ k'(E)}{\Delta E \ \cdot \ G \ \cdot \ \Delta t}$. The same

factor applies to secondaries created in cascades initiated by primaries

with energy between E and E + ΔE. G is the geometrical factor,

$$G = \pi \cdot \Delta A \cdot [\cos^2 \theta - \cos^2 (\theta + \Delta\theta)] \qquad (A2-1)$$

and ΔA and Δt are increments of area and time and may be taken to be

unity. If we absorb the constant factors into the weighting factor,

$$k(E) = \frac{k'(E)}{\pi \cdot \Delta A \cdot \Delta t}$$

and set θ = 0, $\Delta\theta$ = π/2, and τ = 0, we get

$$k(E) = \frac{j_p \ (E + 1/2 \Delta E, \ 0) \ \cdot \ \Delta E}{N_p \ (E, \ \Delta E, \ 0, \ \pi/2, \ 0)} \qquad (A2-2)$$

or

$$k(E) = \frac{j_p \ (E + 1/2 \Delta E, \ 0) \ \cdot \ \Delta E}{N_o \ (E, \ \Delta E)} \qquad (A2-3)$$

Note that for the geometrical factor to be meaningful we must pick an

angular interval within which the intensity is isotropic - for primaries

at the top of the atmosphere this is true over the upper hemisphere.

The choice of θ = 0 and $\Delta\theta$ = π/2 in equations A2-2 and A2-3 is convenient

but any θ, $\Delta\theta$ in the upper hemisphere will give the same k. For

secondaries θ is the direction of interest (θ = 0 for atmospheric

secondary corrections, θ = 180° for splash albedo) and $\Delta\theta$ must be small

enough that the flux is roughly isotropic.

Given the weighting factors, k, and the counts in the secondary

bins, N_s, where

$$N_s = N_s (E_s, \Delta E_s, \theta, \Delta\theta, \tau, E_p),$$

E_s is the secondary energy, and E_p is the energy of the primary which initiated the cascade then

$$j_s \left(E_s + \frac{\Delta E_s}{2}, \tau, \theta, \Delta\theta\right) = \frac{1}{(\Delta E_s) \cdot G \cdot (\Delta t)} \sum_{E_p} N_s(E_s, \Delta E_s, \theta, \Delta\theta, \tau, E_p) k'(E_p)$$

$$= \frac{1}{\Delta E_s [\cos^2\theta - \cos^2(\theta + \Delta\theta)]} \sum_{E_p} N_s(\ldots, E_p) k(E_p)$$

C. Details of the Model and the Cross Sections

Since the accuracy of the calculation is limited by that of
the interaction cross-sections which form the input to the ATSEC
program, these will be discussed in some detail. Other important
details are the atmospheric model and the energy loss of charged
particles -- these are also discussed in this section.

The atmosphere is assumed to be a planar slab with a "top" at
0 gm/cm^2 and a "bottom" at 600 gm/cm^2. No model for density versus
altitude is needed provided the geomagnetic field is vertical (certainly
a good approximation at Ft. Churchill) and the atmosphere is planar.
Assuming a planar atmosphere requires that the scale height ($\sim$8 km) be
small in comparison to the radius of the earth, which is a reasonable
approximation. If, for instance, we consider a primary arriving at a
depth of 1 gm/cm^2 at a polar angle of $\cos^{-1}$ (.1) $\sim 84^{\circ}$, i.e., almost
horizontal, then in the Earth's atmosphere it would have traversed
9.06 gm/cm^2. Only 1% of the primaries are incident at angles larger
than this and the discrepancy becomes smaller at greater depths. The
"bottom" of the atmosphere is that depth below which no more interactions
take place and has the main purpose of saving time in the computation.
It is justified by the fact that very few particles ever reach this
depth.

Note that the inclusion of pions would have required a density
versus altitude model, but the lifetime of pions is short enough that
they almost always decay before undergoing a nuclear interaction in the
quite tenuous medium of the atmosphere.

Ionization energy loss is computed in the program by a sub-routine version of the Space Radiation Lab library program "ENLO" which uses a power-law interpolation scheme based on the Janni (1966), and Barkas and Berger (1964) tables. The accuracy of the ENLO program is limited only by the accuracy of the tables.

The first cross-section used by ATSEC in processing each particle is the total inelastic cross-section or interaction length. The proton cross-section is a function of energy and, therefore, changes as the proton moves along its trajectory, losing energy by ionization. It was considered too complicated to include this feature, and an approximation was used in which the total interaction probability P_{int} (E_o) is specified as a function of the initial energy of the proton. A constant average interaction length, $\lambda(E_o)$ is calculated which gives the same probability of interacting, that is

$$P_{int}(E_o) = 1 - \exp \left\{ -N_o \int_0^{P(E_o)} dx \frac{\Sigma_i \, r_i \, \sigma_1 \, (x)}{\Sigma_i \, r_i \, A_i} \right\}$$

= probability that a proton interacts before

stopping due to ionization energy loss

where

N_o is Avogadro's number.

$P(E_o)$ is the total pathlength of the proton.

r_i is the faction of the i'th element in the mixture (air).

$\sigma_i = \sigma_i (E(x))$ is the total cross section of the i'th

element for protons of energy $E(x)$.

A_i is the atomic weight of the i'th element.

The integral is calculated by changing variables and integrating over energy instead of pathlength

$$P_{int} = 1 - \exp \left\{ -N_o \int_o^E \frac{dE}{dE/d\tau} \quad \frac{\Sigma_i \; r_i \; \sigma_i \; (E)}{\Sigma_i \; r_i \; A_i} \right\}$$

where τ is the depth in gm/cm^2. The average interaction length $\lambda(E_o)$ is defined by

$$P_{int} (E_o) = 1 - e^{-R/\lambda}$$

where R is the range of the proton. This average interaction length is a function only of the initial energy of the proton and does not change along the path. The function P_{int} is tabulated by Janni (1964) who used primarily the cross-sections of Bertini (1963, 1966), and Metropolis et al., (1958a;b). Figure A2-2 is a plot of $1-P_{int}$ versus range. The slope of this curve at any given energy is determined by the total cross section for a proton-air interaction at that energy. The average interaction length $\lambda(E_o)$ defined above is determined by the slope of the line connecting the point $(1-P_{int} (E_o), E_o)$ with the upper left-hand corner (the point $(1,0)$).

The neutron interaction length is also specified as a function of energy, but since the neutron energy is assumed constant along its

path no averaging was needed. The cross-sections were taken from Bertini (1966) for C^{12} and O^{16}. The N^{14} cross-section was taken to be the average of the C^{12} and O^{16} and the N^{14} and O^{16} cross-sections were used to calculate $\lambda(E_o)$ in air.

For both protons and neutrons it was necessary to extrapolate cross-sections to higher energies. Since the Bertini cascade calculations are based on the pp and np cross-sections, the air cross sections were assumed to behave in a similar manner-- i.e., almost constant above 2 GeV.

The average multiplicity of cascade protons for O^{16} is shown in Figure A2-3, with the emulsion data and the heavy element data from intranuclear-cascade calculations. One finds a discrepancy between the cascade data and the emulsion data, even allowing for the differences between gray and shower tracks and cascade protons. The O^{16} data are quite different from either the emulsion data or the heavy-element cascade data. The C^{12} data were essentially identical to the O^{16} data, justifying the use of the O^{16} curve for air. Bertini (1966, 1967) gives the multiplicity distributions as a function of energy as well as the average multiplicity. These distributions were used in the calculation.

For evaporation protons and deuterons the C^{12} and O^{16} data were used to calculate the multiplicity in air. No evaporation particles were generated with an energy less than 10 MeV/nucleion; this energy is therefore the lower limit of the validity of the computation. The energy spectra of evaporation particles were used to adjust the multiplicities for the lack of particles of <10 MeV/nucleon. These

energy spectra (above 10 MeV/nucleon) were fit by exponentials of the form,

$$N(E) \propto e^{-E/E_0} \quad .$$

An isotropic angular distribution was used.

Evaporation particles were not allowed to interact; this was done to simplify program coding and should have no significant effect on the results. Since neutrons were included only for the reason that they might interact and create more protons, evaporation neutrons were not included. Therefore the neutron spectra calculated from ATSEC results are deficient below about 20-30 MeV.

The angular distributions for cascade particles were taken from Bertini (1966, 1967) in tabular form and fit with simple functional forms for coding purposes. The data used were for 0^{16}. The distributions were parameterized by primary type and energy and secondary type. The energy distributions for cascade particles were taken from Alsmiller and Barish's (1969) fits to the Bertini data and were parameterized by primary type and energy, secondary type, and angle of emission of secondary. The correlation between angle of emission and energy is important since the energy distributions are quite different in the forward and backward directions.

The spectrum of secondaries produced by primary alpha particles was calculated in a manner similar to the method used for the primary protons. The cross sections were assumed to be the same as for the protons with the following exceptions:

1) the total interaction cross section was assumed to be constant, with a value for λ of 45 gm/cm^2,

2) the average multiplicities were increased by a factor of 1.5,

3) there was a 12.5% chance of generating a "straight-on" proton and an 8% chance of generating a "straight-on" deuteron. The "straight-on" particles are secondaries which continue in the same direction and at the same velocity as the primary.

D. Fit to the Measurements and Comparison with Previous Results

In Figure A2-4 we show two of the measured proton intensity versus altitude (τ) curves for 1969, including a point at 0 gm/cm^2 derived from the OGO-6 measurements. The smooth curves are the results of the ATSEC calculation. They have been fit to the data by multiplying the calculated secondaries by a constant factor, independent of energy and depth. This factor compensates, at least to first order in τ/λ, for uncertainties in interaction length, multiplicity, and input primary spectrum.

The factor has the value 1.13 and is a small correction considering the uncertainities in the calculation.

Figure A2-5 is a comparison of our results with those of other investigators. The spectrum of secondaries at 3 gm/cm^2 is shown. The appropriate dates are shown in the figure because of the possibility that time variations of the primary input spectrum might invalidate the comparison. Since the level of solar modulation for 1963-1964 is not significantly different from 1966, and for 1965 is only slightly different from either (see, for instance, Figure V-1), time variations should not seriously affect the comparison.

Our curve is calculated for the assumed 1966 primary input spectrum using the factor of 1.13 derived from the 1969 measurements. The curve attributed to Fichtel was calculated at Caltech using data supplied to us in a private communication. The Teegarden (1967a, 1967b) data were given by the author as points but they do not represent a direct measurement of secondaries, as do our data.

The fact that our calculation agrees with the measurements made in and above the atmosphere within a 13% correction gives us considerable confidence in using our results to correct data obtained from balloon-borne instruments to the top of the atmosphere.

REFERENCES

R. G. Alsmiller and J. Barish, "Analytic Representation of Nucleon- and Pion-Emission Spectra from Nucleon-Nucleus Collisions in the Energy Range 750-2000 MeV," Oak Ridge National Laboratory - TM - 2277, (1968).

R. G. Alsmiller, Jr. and R. T. Boughner, "Solar Neutron Transport in the Earth's Atmosphere," J. Geophys. Res., 73, 4935, (1968).

W. E. Althouse, E. C. Stone, R. E. Vogt and T. H. Harrington, "A Solar and Galactic Cosmic Ray Satellite Experiment," IEEE Transactions on Nuclear Science, 15, 229, (1967).

H. R. Anderson, "The Radial Gradient of Cosmic Radiation Measured by Mariners 2 and 4," J. Geophys. Res., 73, 2897, (1968).

M. V. K. Appa Rao, "Isotropic Composition of the Low-Energy Helium Nuclei in the Primary Cosmic Radiation," Phys. Rev., 123, 295, (1961).

M. V. K. Appa Rao, R. R. Daniel and K. A. Neelakantan, "Nuclear Integrations Produced in Nuclear Emulsions by α-particles of Great Energy," Proc. Indian Acad. Sci., 43, 181 (1956).

V. K. Balasabrahmanyan and D. Venkatesan, "Spectral Variations in Short Term (Forbush) Decreases and in Long Term Changes in Cosmic Ray Intensity," Acta Physica Academiae Scientiarum Hungaricae, 29, Suppl. 2, 327, (1970).

W. H. Barkas and M. J. Berger, "Tables of Energy Losses and Ranges of Heavy Charged Particles," NASA SP-3013, (1965).

M. Bercovitch, "The Heliocentric Radial Density Gradient of Relativistic Cosmic Rays in 1967-68," The 12th International Conference on Cosmic Rays, Vol. 2, 579, University of Tasmania, Hobart, Tasmania, (1971).

H. W. Bertini, "Low-Energy Intranuclear Cascade Calculation," Phys. Rev., 131, 1801, (1963).

H. W. Bertini, "Results from Low-Energy Intranuclear-Cascade Calculation," Nucl. Phys., 87, 138 (1966).

H. W. Bertini, "Preliminary Data from Intranuclear-Cascade Calculations of 0.75-, 1-, and 2-GeV Protons on Oxygen, Aluminum and Lead, and 1-GeV Neutrons on the Same Elements," Oak Ridge National Laboratory-TM-1996, (1967).

H. W. Bertini, "Intranuclear Cascade Calculation of the Secondary Nucleon Spectra from Nucleon-Nucleus Interactions in the Energy Range 340 to 2900 MeV and Comparisons with Experiment," Phys. Rev., 188, 1711, (1969).

H. W. Bertini and M. P. Guthrie, "Results from Medium-Energy Intranuclear-Cascade Calculation," Oak Ridge National Laboratory-TM-336, (1970).

J. J. Burger, "A Phenomenological Approach to the Solar Modulation of Cosmic Rays," Astrophys. J., 166, 651 (1971).

J. J. Burger and B. N. Swanenburg, "Long-Term Solar Modulation of Cosmic-Ray Electrons with Energies above 0.5 GeV," The 12th International Conference on Cosmic Rays, Vol. 2, 554, University of Tasmania, Hobart, Tasmania, (1971).

U. Camerini, P. H. Fowler, W. O. Lock and H. Muirhead, "Nuclear Transmutations Produced by Cosmic-Ray Particles of Great Energy - The Distribution in Energy and Secondary Interactions of the Particles Emitted from Stars," Phil. Mag., 41, 413, (1950).

M. Ceccarelli, G. Quareni and G. T. Zorn, "On the Nuclear Interactions of He-Nuclei in the Cosmic Radiation," Nuovo Cimento, 1, Series 10, 669, (1955).

F. F. Chen, C. P. Leavitt and A. M. Shapiro, "Attenuation Cross Sections for 860-MeV Protons," Phys. Rev., 99, 857 (1955).

K. Chen, Z. Fraenkel, G. Friedlander, J. R. Grover, J. M. Miller and Y. Shimamoto, "VEGAS: A Monte Carlo Simulation of Intranuclear Cascades," Phys. Rev., 166, 949, (1968).

T. F. Cleghorn, P. S. Freier and C. J. Waddington, "The Energy Dependence of the Fragmentation Parameters and Mean Free Paths of Cosmic Ray Nuclei with Z > 10," Can. J. Phys., 46, S572, (1968).

P. J. Coleman, Jr., "Variations in the Interplanetary Magnetic Field: Mariner 2, 1, Observed Properties," J. Geophys. Res., 71, 5509, 1966.

A. C. Cummings, Private Communication, (1972).

R. W. Deutsch, "Secondary Particles Resulting from High-Energy Nuclear Bombardment of Al, Ag, Au, U," Phys. Rev., 97, 110, (1955).

ESSA Solar Geophysical Data, Vols. 229-307, World Data Center A, Boulder, Colorado, 1967-70.

L. C. Evans, "OGO-4 Data Coverage Plots," SRL Internal Report No. 25, California Institute of Technology, (1971).

C. Y. Fan, G. Gloeckler, B. McKibben, K. R. Pyle and J. A. Simpson, "Differential Energy Spectra and Intensity Variation of 1-20 MeV/Nucleon Protons and Helium Nuclei in Interplanetary Space," Can. J. Phys., 46, S498, (1968).

J. L. Fanselow and E. C. Stone, "Geomagnetic Cutoffs for Cosmic Ray Protons for Seven Energy Intervals between 1.2 and 39 MeV," J. Geophys. Res., 77, to be published, (1972).

C. E. Fichtel, D. E. Guss, G. R. Stevenson and C. J. Waddington, "Cosmic-Ray Hydrogen and Helium Nuclei during a Solar Quiet Time in July 1961," Phys. Rev., 133, B818, (1964).

E. L. Fireman and G. Spannazel, "Radial Gradient of Cosmic Rays from the Lost City Meteorite," J. Geophys. Res., 76, 4127, (1971).

L. A. Fisk, Behaviour of Cosmic Rays in the Interplanetary Medium, Ph. D. Thesis, University of California at San Diego, (1969).

L. A. Fisk, "Solar Modulation of Galactic Cosmic Rays, 2," J. Geophys. Res., 76, 221, (1971).

L. A. Fisk and W. I. Axford, "Solar Modulation of Galactic Cosmic Rays, 1," J. Geophys. Res., 74, 4973, (1969).

L. A. Fisk, M. A. Forman and W. I. Axford, "Solar Modulation of Galactic Cosmic Rays, Implications of the Compton-Getting Coefficient," EOS, Trans. A. G. U., 53, 480, (1972).

M. A. Forman, "The Compton-Getting Effect for Cosmic-Ray Particles and Photons and the Lorentz Invariance of Distribution Functions," Planet. Space Sci., 18, 25, (1970).

M. A. Forman, L. A. Fisk and W. I. Axford, "Compton-Getting Coefficient of Severely Modulated Galactic Cosmic Rays," Bulletin of the A.P.S., Series II, 17, 456, (1972).

M. A. Forman, R. W. Stoenner and R. Davis, Jr., "Cosmic-Ray Gradient Measured by the Argon 37/Argon 39 Ratio in the Lost City Meteorite," J. Geophys. Res., 76, 4109, (1971).

P. S. Freier and C. J. Waddington, "Electrons, Hydrogen Nuclei, and Helium Nuclei Observed in the Primary Cosmic Radiation during 1963," J. Geophys. Res., 70, 5753, (1965).

P. S. Freier and C. J. Waddington, "Singly and Doubly Charged Particles in the Primary Cosmic Radiation," J. Geophys. Res., 73, 4261 (1968).

T. L. Garrard, "OGO-6 Monthly Summary Plots," SRL Internal Report No. 27, California Institute of Technology, (1971).

L. J. Gleeson and W. I. Axford, "Solar Modulation of Galactic Cosmic Rays," Astrophys. J., 154, 1011, (1968).

L. J. Gleeson and I. H. Urch, "Energy Losses and Modulation of Galactic Cosmic Rays," Astrophysics and Space Science, 11, 228, (1971).

G. Gloeckler and J. R. Jokipii, "Solar Modulation and the Energy Density of Galactic Cosmic Rays," Astrophys. J., 148, L41, (1967).

M. L. Goldstein, L. A. Fisk and R. Ramaty, "Energy Loss of Cosmic Rays in the Interplanetary Medium," Phys. Rev. Letters, 25, 832 (1970a).

M. L. Goldstein, R. Ramaty and L. A. Fisk, "Interstellar Cosmic Ray Spectra from the Nonthermal Radio Background from 0.4 to 400 MHz," Phys. Rev. Letters, 24, 1193, (1970b).

J. T. Gosling, R. T. Hansen and S. J. Bame, "Solar Wind Speed Distribution: 1962-1970," J. Geophys. Res., 76, 1181 (1971).

K. C. Hsieh, "Study of Solar Modulation of Low-Energy Cosmic Rays Using Differential Energy Spectra of Protons, ^{3}He, and ^{4}He at E < 100 MeV per Nucleon during the Quiet Time in 1965 and 1967," Astrophys. J., 159, 61, (1970).

K. C. Hsieh, G. M. Mason and J. A. Simpson, "Cosmic-Ray ^{2}H from Satellite Measurements, 1965-1969," Astrophys. J., 166, 221, (1971).

M. H. Isreal and R. E. Vogt, "Characteristics of the Dirunally Varying Electron Flux near the Polar Cap," J. Geophys. Res., 74, (1969).

P. L. Jain, E. Lohrmann and M. W. Teucher, "Heavy Nuclei and α Particles between 7 and 100 BeV/Nucleon, II, Fragmentation and Meson Production "and" III, Energy Spectrum of the Heavy Nuclei in the Cosmic Radiation between 7- and 100-BeV/Nucleon," Phys., Rev., 115, 643 and 654, (1959).

J. F. Janni, "Calculations of Energy Loss, Range, Pathlength, Straggling, Multiple Scattering, and the Probability of Inelastic Nuclear Collisions for 0.1 - to 1000 - MeV Protons," Air Force Weapons Laboratory-TR-65-1500, (1966).

J. R. Jokipii, "Cosmic-Ray Propagation, 1, Charged Particles in a Random Magnetic Field," Astrophys. J., 146, 480, (1966).

J. R. Jokipii, "Cosmic-Ray Propagation, 2, Diffusion in the Interplanetary Magnetic Field," Astrophys. J., 149, 504, (1967).

J. R. Jokipii, "Addendum and Erratum to Cosmic-Ray Progration, 1," Astrophys. J., 152, 671, (1968).

J. R. Jokipii, "Propagation of Cosmic Rays in the Solar Wind," Reviews of Geophysics and Space Physics, 9, 27, (1971).

J. R. Jokipii and P. J. Coleman, Jr., "Cosmic-Ray Diffusion Tensor and its Variation Observed with Mariner 4," J. Geophys. Res., 73, 5495, (1968).

J. H. Kinsey, "Identification of a Highly Variable Component in Low-Energy Cosmic Rays at 1 A.U.," Phys. Rev. Letters, 24, 246, (1970).

S. M. Krimigis and D. Venkatesan, "The Radial Gradient of Interplanetary Radiation Measured by Mariners 4 and 5," J. Geophys. Res., 74, 4129, (1969).

J. A. Lezniak and W. R. Webber, "Measurements of Gradients and Anisotropies of Cosmic Rays in Interplanetary Space: Pioneer 8," Acta Physica Academiae Scientiarum Hungaricae, 29, Suppl. 2, 111, (1970).

J. A. Lezniak and W. R. Webber, "Solar Modulation of Cosmic Ray Protons, Helium Nuclei, and Electrons: A Comparison of Experiments with Theory," J. Geophys. Res., 76, 1605, (1971).

E. Lohrmann and M. W. Teucher, "Heavy Nuclei and α particles between 7- and 100-BeV/Nucleon," Phys. Rev., 115, 636, (1959).

J. J. Lord, "The Altitude and Latitude Variation in the Rate of Occurence of Nuclear Disintegrations Produced in the Stratosphere by Cosmic Rays," Phys. Rev., 81, 901, (1951).

J. E. Lupton, "Solar Flare Particle Propagation--Comparision of a New Analytic Solution with Spacecraft Measurements," Ph. D. Thesis, California Institute of Technology, (1971).

G. M. Mason, "Interstellar Propagation of Galactic Cosmic-Ray Nuclei $2 \leq Z \leq 8$ in the Energy Range 10-1000 MeV per Nucleon," Astrophys. J., 171, 139, (1972).

T. Mathews, J. Quenby and J. Sear, "Mechanism for Cosmic Ray Modulation," Nature, 229, 246, (1971).

K. G. McCracken and U. R. Rao, "Solar Cosmic Ray Phenomena," Space Science Reviews, 11, 155, (1970).

N. Metropolis, R. Bivins, M. Storm, A. Turkevich, J. M. Miller and G. Friedlander, "Monte Carlo Calculations on Intranuclear Cascades. I. Low-Energy Studies," Phys. Rev., 110, 185, (1958a).

N. Metropolis, R. Bivins, M. Storm, J. M. Miller, G. Friedlander and A. Turkevich, "Monte Carlo Calculations on Intranuclear Cascades. II. High-Energy Studies and Pion Processes," Phys. Rev., 110, 204, (1958b).

J. P. Meyer, "Cosmic Ray Deuterons and He^3, Interplanetary Deceleration and Energy Spectra of Sources," The 12th International Conference on Cosmic Rays, Vol. 2, 169, University of Tasmania, Hobart, Tasmania, (1971).

S. S. Murray, "Propagation of 1-10 MeV Solar Protons in Interplanetary Space," Ph. D. Thesis, California Institute of Technology, (1970).

S. S. Murray, E. C. Stone and R. E. Vogt, "Interplanetary Deceleration of Solar Cosmic Rays," Phys. Rev. Letters, 26, 663 (1971).

J. H. Noon and M. F. Kaplon, "Interactions of the Heavy Nuclei of the Cosmic Radiation," Phys. Rev., 97, 769, (1955).

J. J. O'Gallagher, "Cosmic-Ray Radial Density Gradient and Its Rigidity Dependence Observed at Solar Minimum on Mariner 4," Astrophys. J., 150, 675, (1967).

J. F. Ormes and W. R. Webber, "Proton and Helium Nuclei Cosmic-Ray Spectra and Modulations between 100 and 2000 MeV/Nucleon," J. Geophys. Res., 73, 4231, (1968).

E. N. Parker, Interplanetary Dynamical Processes, John Wiley and Sons, New York, (1963).

E. N. Parker, "The Passage of Energetic Charged Particles through Interplanetary Space," Planet. Space Sci., 13, 9, (1965).

C. F. Powell, P. H. Fowler and D. H. Perkins, The Study of Elementary Particles by the Photographic Method, Pergammon Press, N.Y., 1959.

G. Quareni and G. T. Zorn, "On the Nuclear Interactions of 350 MeV α-Particles," Nuovo Cimento, 1, Series 10, 1282, (1955).

U. R. Rao, K. G. McCracken and R. P. Bukata, "Cosmic Ray Propagation Processes, 3, The Diurnal Anisotropy in the Vicinity of 10 MeV/Nucleon," J. Geophys. Res., 72, 4343, (1967).

T. A. Rygg and J. A. Earl, "Balloon Measurements of Cosmic Ray Protons and Helium over Half a Solar Cycle 1965-1969," J. Geophys. Res., 76, 7445, (1971).

J. W. Sari, "Modulation of Cosmic Rays by Interplanetary Magnetic Field," EⓄS, Trans. A. G. U., 53, 480, (1972).

J. W. Sari and N. F. Ness, "Power Spectra of the Interplanetary Magnetic Field," Solar Phys., 8, 155, (1969).

G. L. Siscoe, L. Davis, Jr., P. J. Coleman, Jr., E. J. Smith and D. E. Jones, "Power Spectra and Discontinuities of the Interplanetary Magnetic Field: Mariner 4," J. Geophys. Res., 73, 61, (1968).

J. F. Steljes, "Cosmic Ray NM-64 Neutron Monitor Data - I to XVI," Atomic Energy of Canada Limited, Chalk River, Ontario, (1965 to 1970).

P. H. Stoker and H. Carmichael, "Steplike Changes in the Long-Term Modulation of Cosmic Rays," Astrophys. J., 169, 357, (1971).

J. D. Sullivan, "Geometrical Factor and Directional Response of Single and Multi-Element Particle Telescopes," Nuclear Instruments and Methods, 95, 5, (1971).

K. R. Symon, "Fluctuations in Energy Loss by High Energy Charged Particles in Passing through Matter," Ph. D. Thesis, Harvard University, (1948).

B. J. Teegarden, "A Study of Low Energy Galactic Cosmic Rays from 1961 to 1965," Ph. D. Thesis, University of Maryland, (1967), GSFC X-611-67-8.

B. J. Teegarden, "Atmospheric Secondary and Re-Entrant Albedo Protons," J. Geophys. Res., 72, 4857, (1967).

I. H. Urch and L. J. Gleeson, "Galactic Cosmic Modulation from 1965-1970," preprint, submitted to Astrophysics and Space Science, (1972).

R. Vogt, "Primary Cosmic-Ray and Solar Protons," Phys. Rev., 125, 336, (1962)

C. J. Waddington, "The Alpha-Particle Component of the Cosmic Radiation," Phil. Mag., 45, 1312 (1954).

C. J. Waddington, "The Composition of the Primary Cosmic Radiation," Prog. Nuc. Phys., 8, 1, (1960).

K. P. Wenzel, "Primaere, Sekundaere und Albedo-Protonen aus der kosmischen Strahlung," Ph. D. Thesis, Ruprecht-Karl-Universitaet, Heidelberg, (1968) or "Cosmic-Ray Protons, Atmospheric Secondaries, and Proton Albedo at High and Low Geomagnetic Latitudes," SRL Internal Report Number 70-2.

D. S. Willoughby, "Interactions of 380-MeV Alpha Particles in Nuclear Track Emulsion," Phys., Rev., 101, 324, (1956).
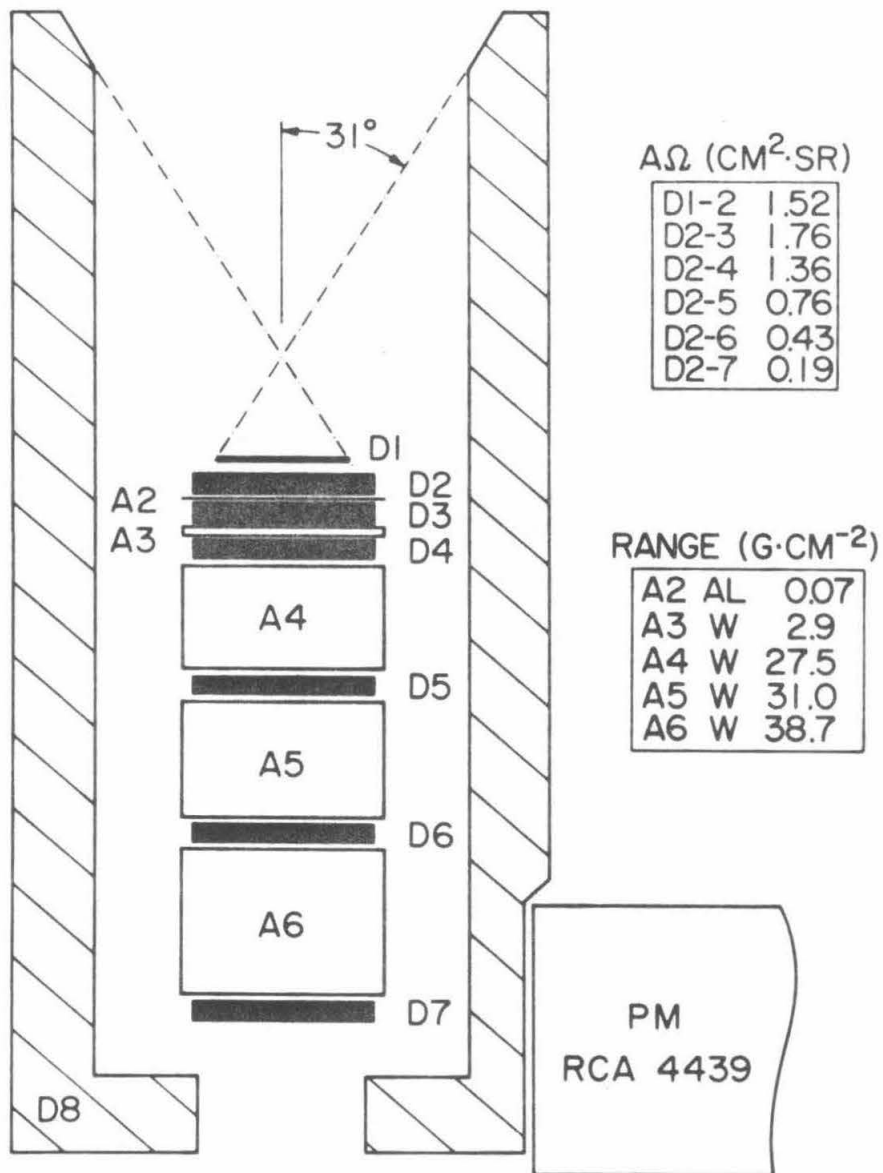
Figure II-1

Schematic cross-section of the range telescope. The geometrical factors
(AΩ) given are nominal since the geometrical factor is a function of
energy.

Figure II-2: Calculated average energy loss of protons and alpha
particles in various range-telescope detectors as a function of incident
kinetic energy. The deepest detector penetrated is noted along the
incident-energy scale. Vertical incidence is assumed.
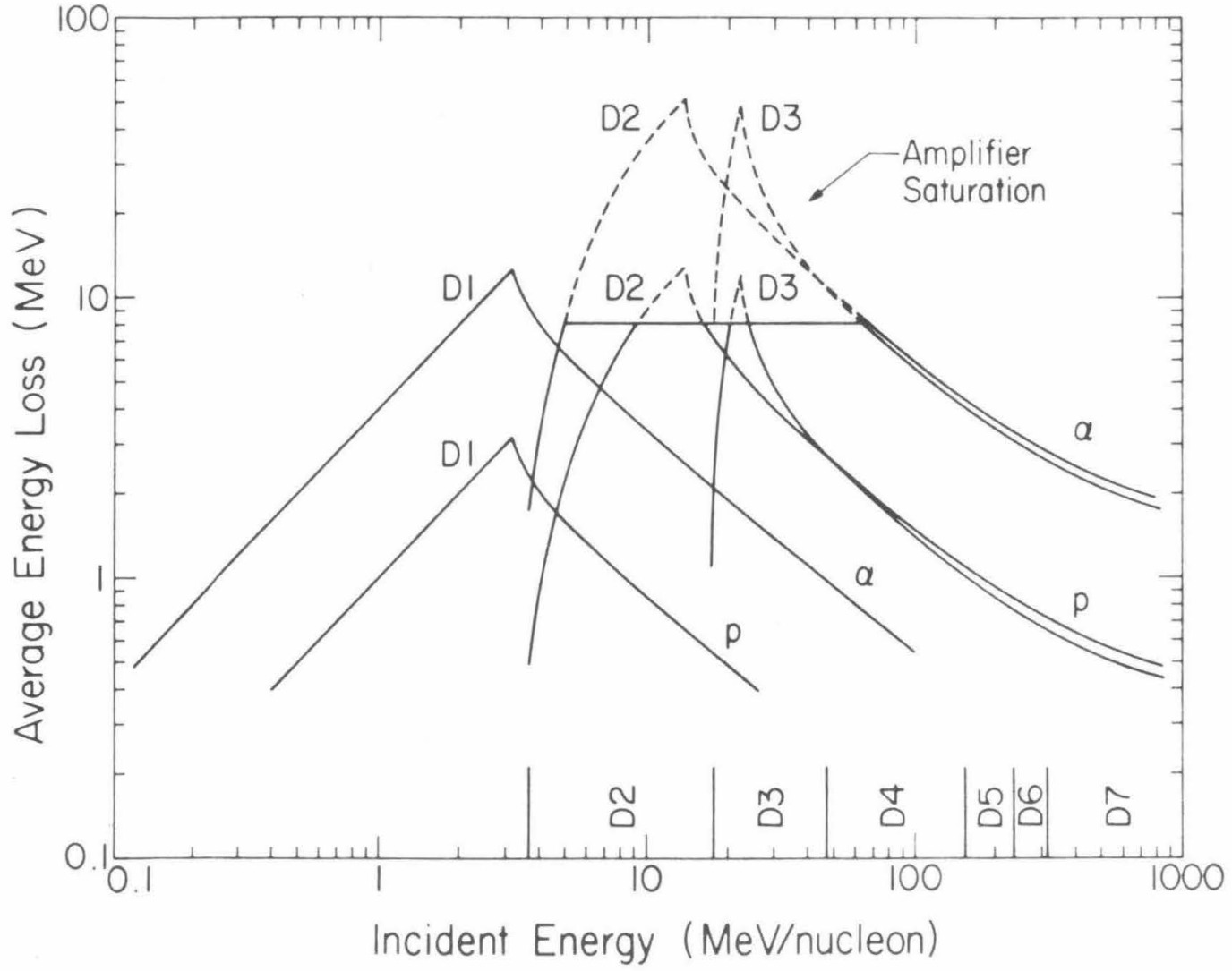
Figure II-2
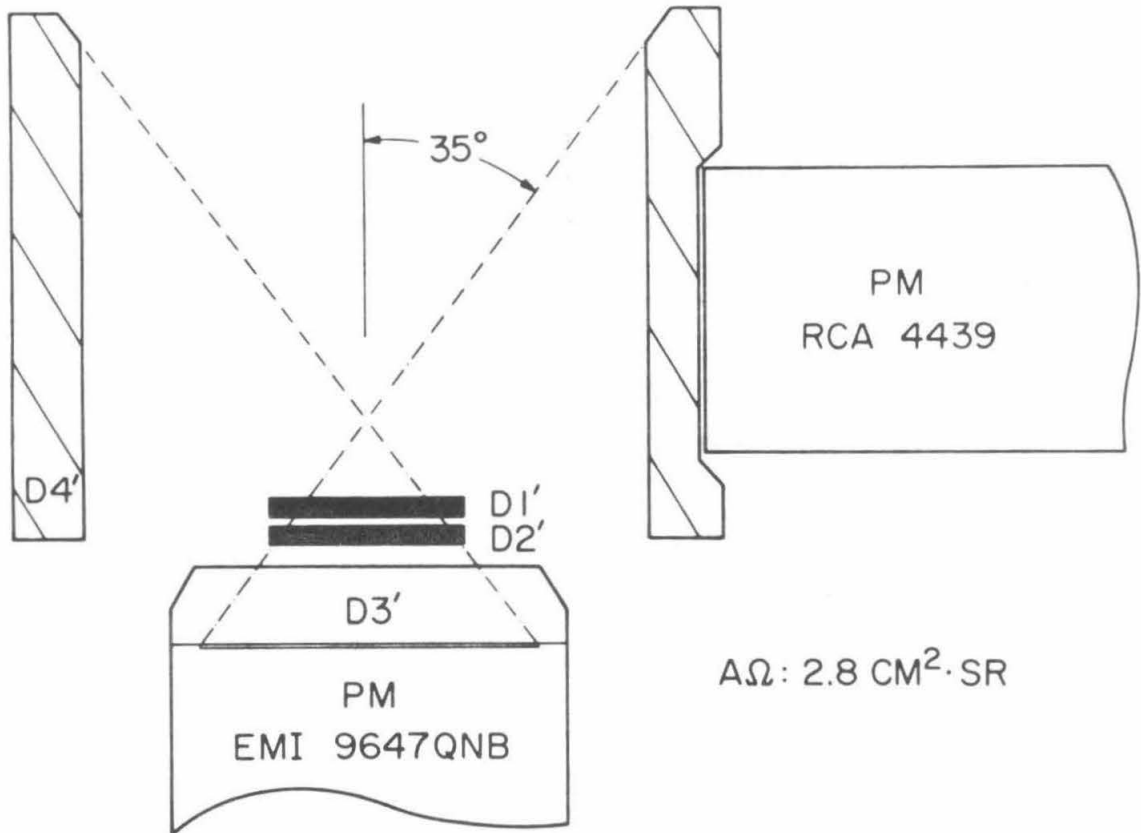
Figure II-3

Schematic cross-section of the Čerenkov telescope.
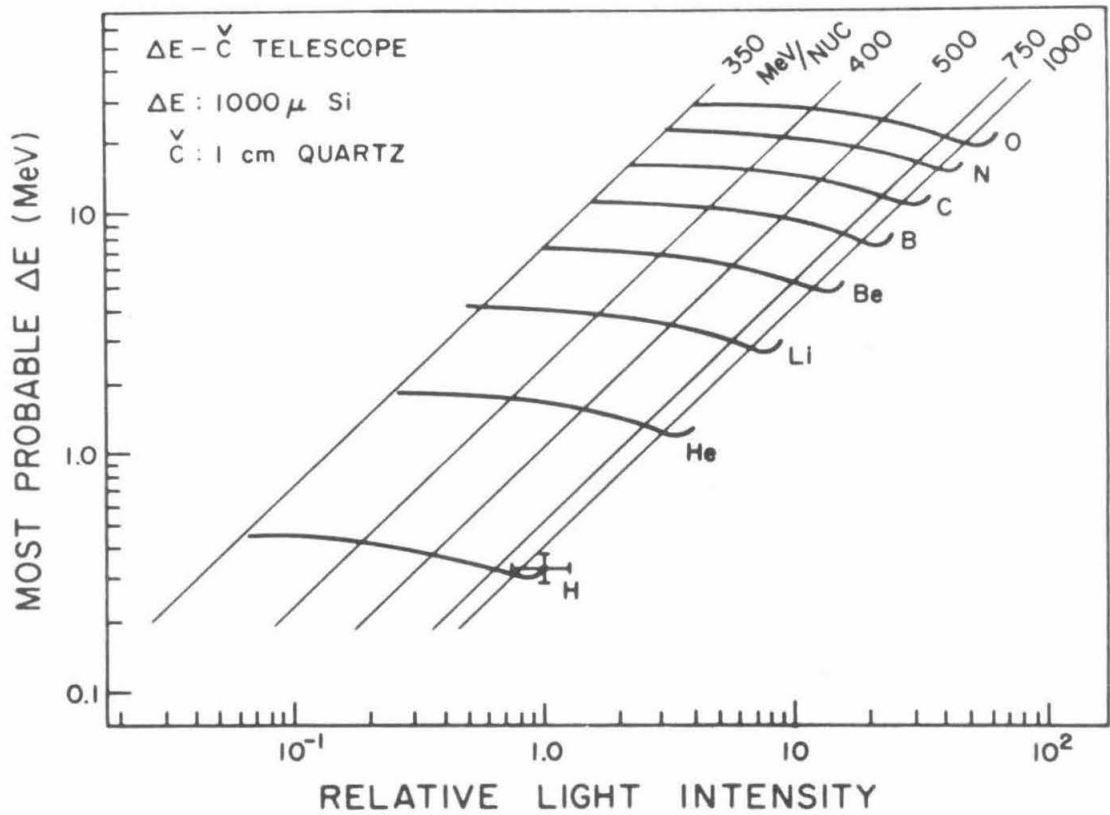
Figure II-4

Average energy loss in 1000μ of silicon versus relative Čerenkov-light intensity for H through O nuclei. The error bars on the H curve indicate 30% (FWHM) resolution for ionization energy loss and 35% resolution in Čerenkov-light intensity. These values are typical of the Čerenkov-telescope system.

137

Figure II-5: Schematic block diagram of the pe electronic-logic
system. The range-telescope logic is illustrated in (a) and the
Čerenkov-telescope logic in (b) for simplicity, but many of the
components are common to the two systems.

Figure II-5a

138

Figure II-5b

139

140
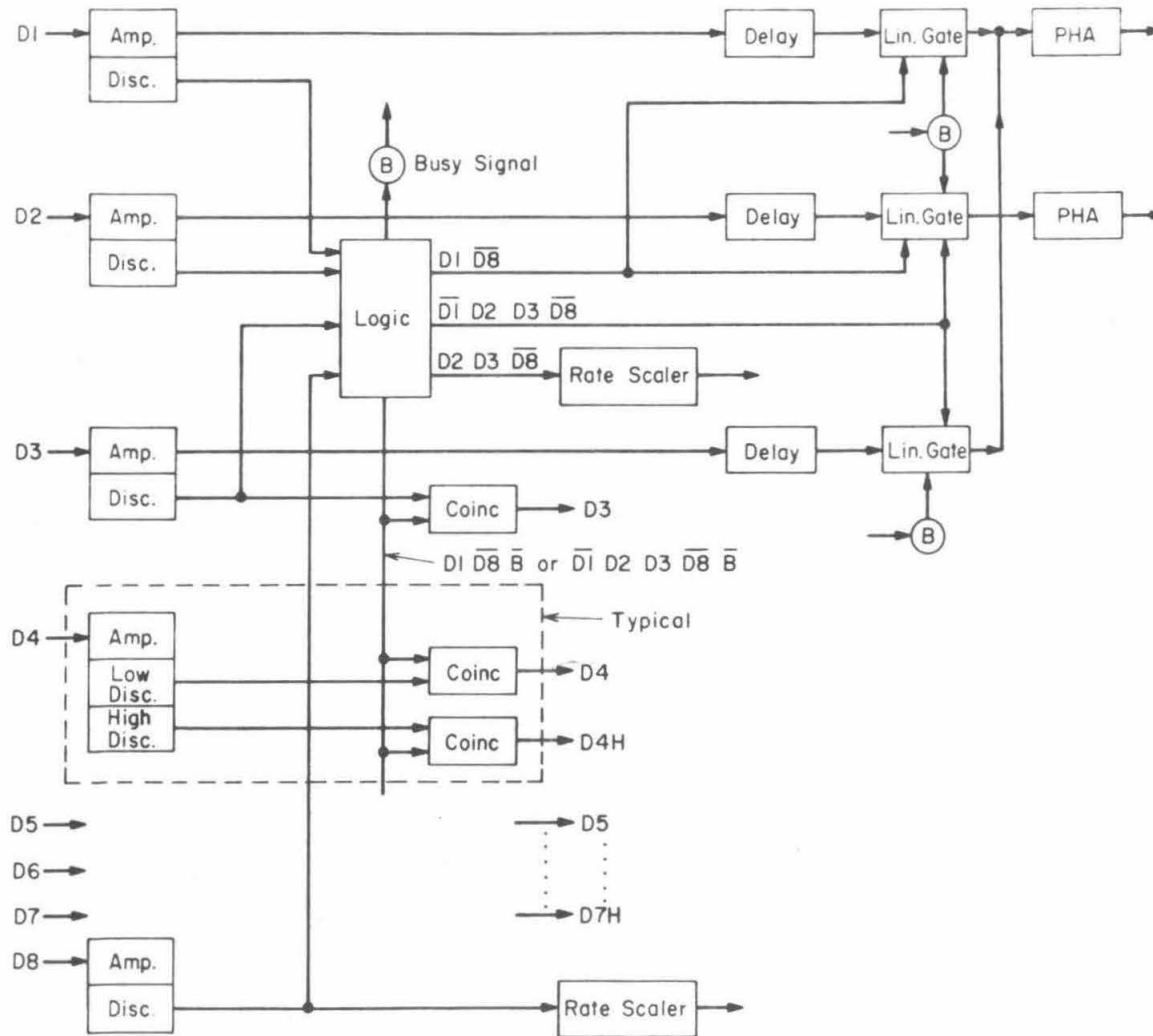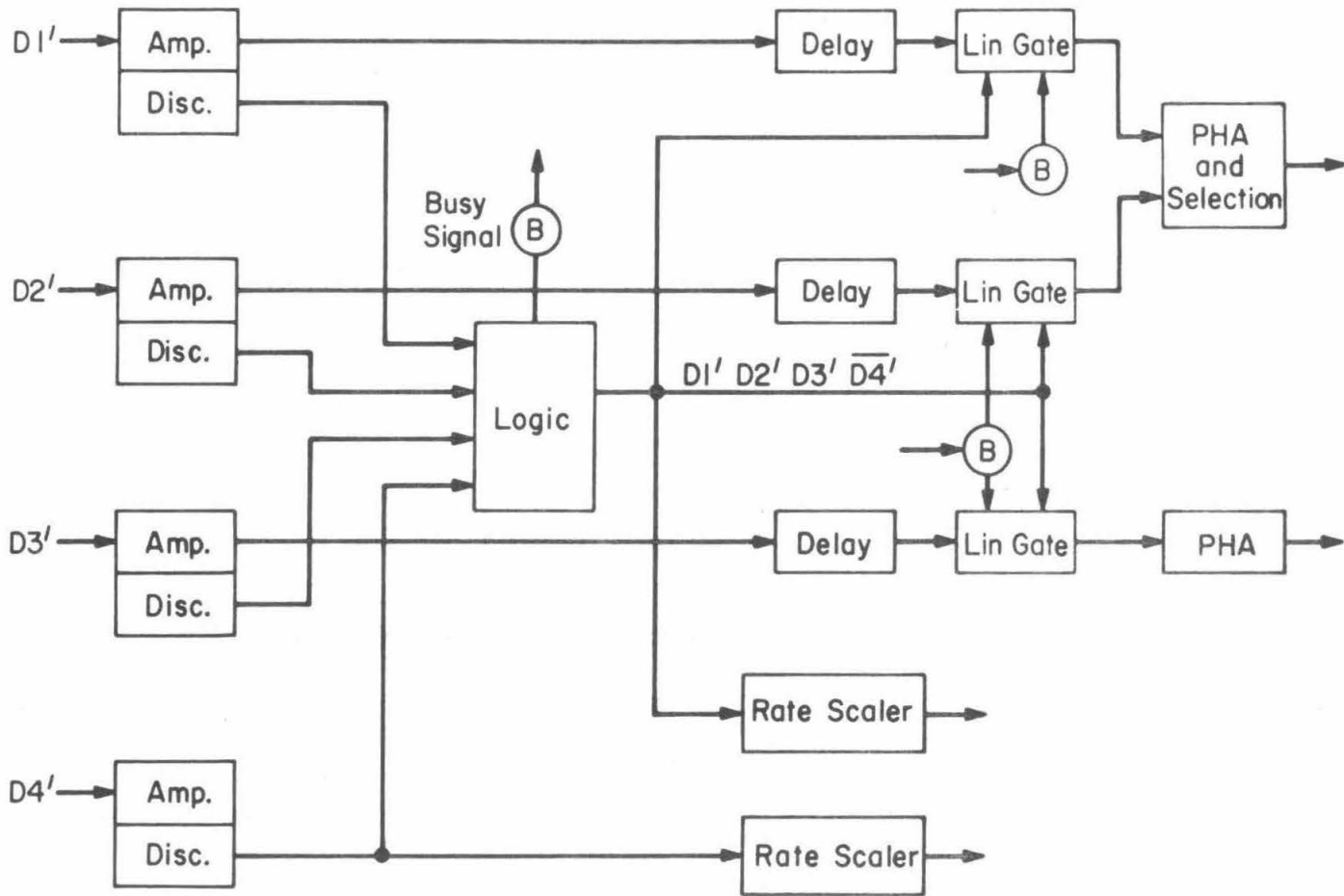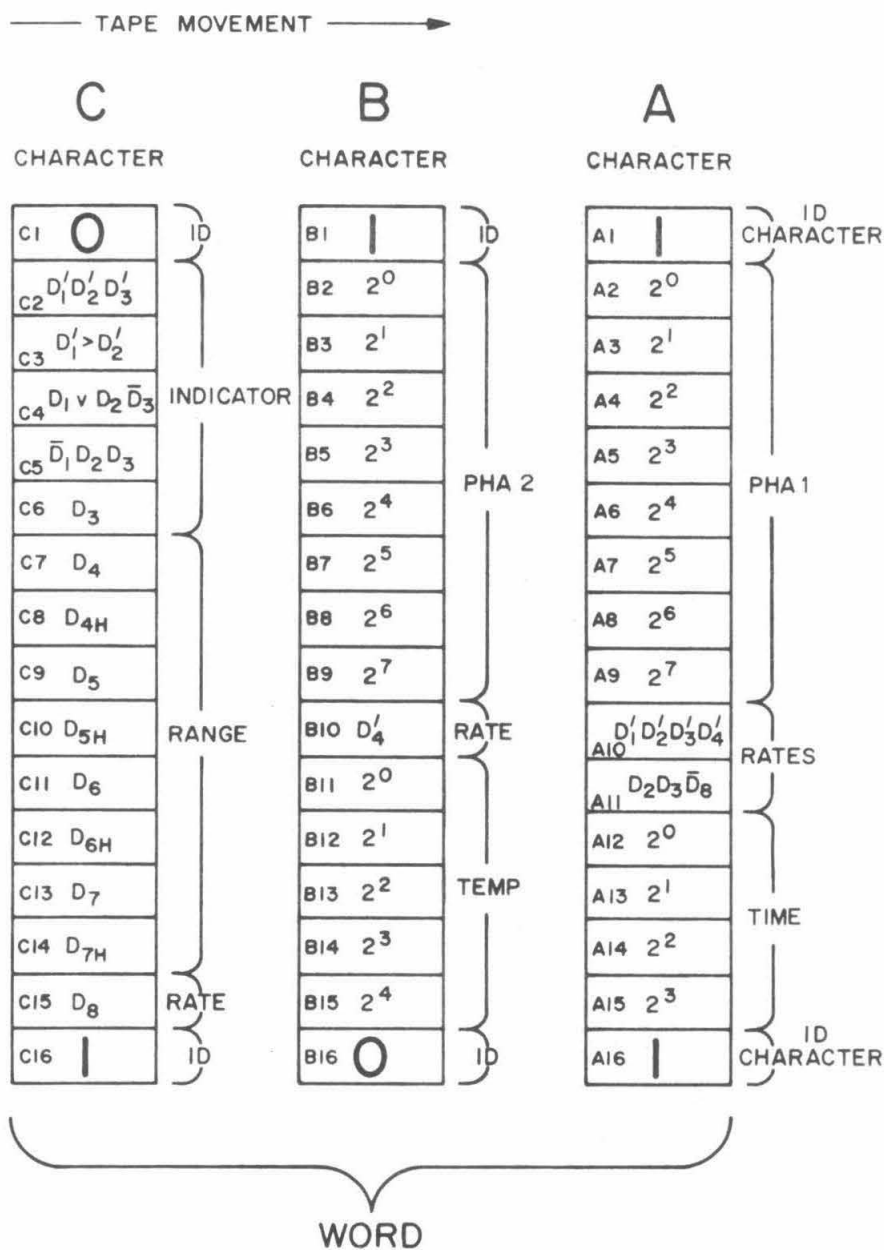
Figure II-6

Illustration of the bit arrangement in the word recorded for each
analyzed event in the pɑe instrument.
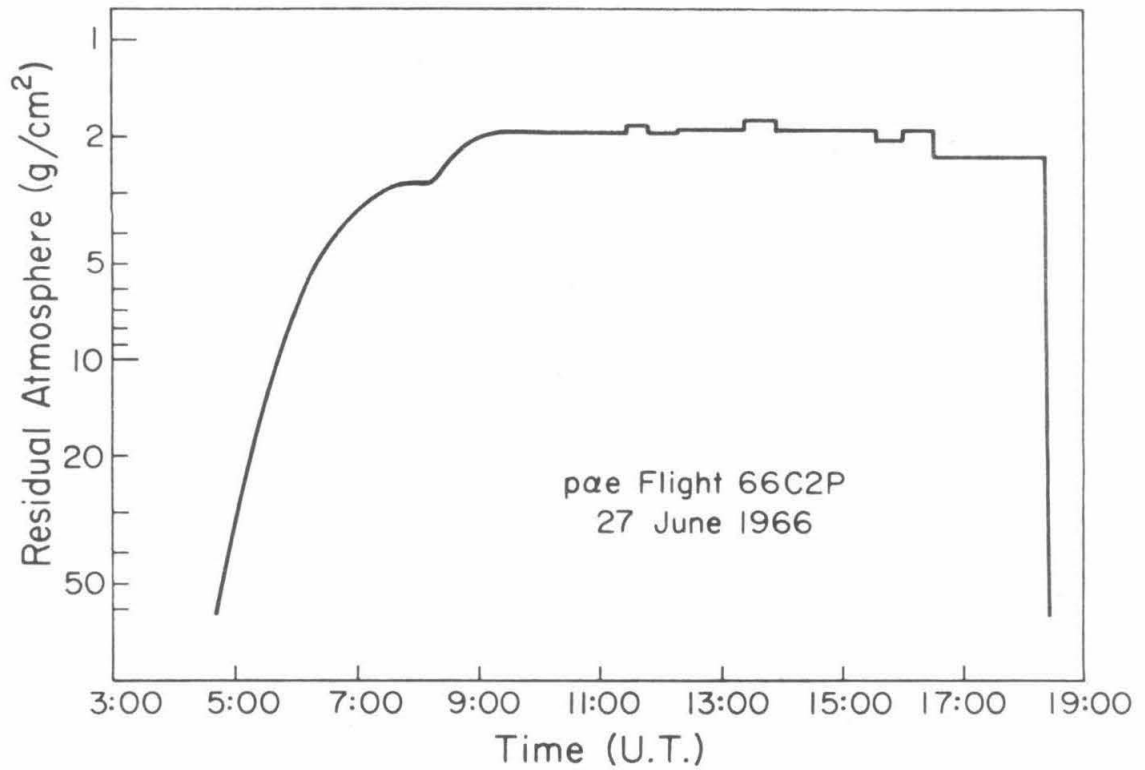
Figure III-1

Plot of residual atmosphere versus time for a balloon flight.   Launch
was at 3:01 U.T.
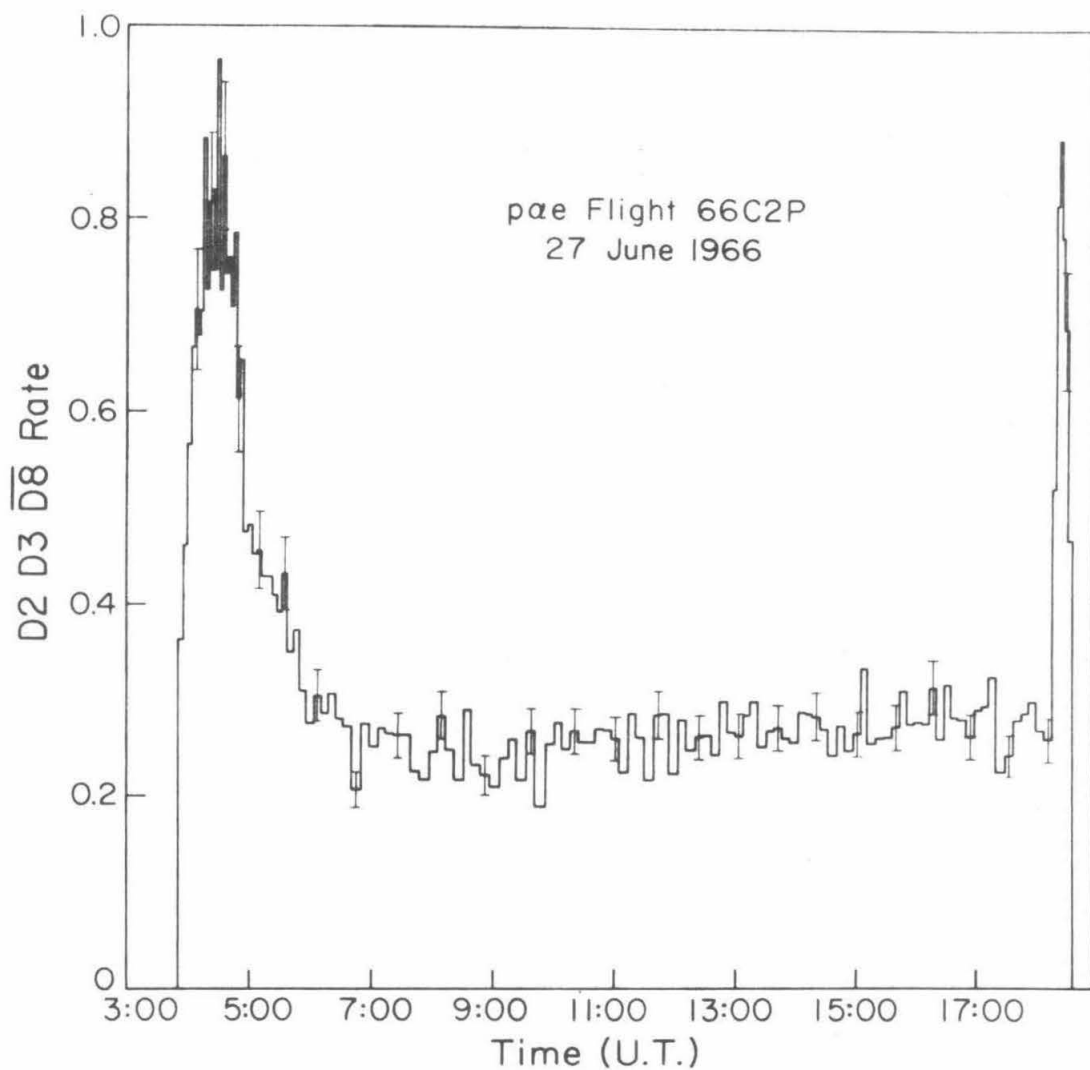
Figure III-2

Plot of the counting rate of D2D3$\overline{D8}$ events in counts per second versus time for the balloon flight shown in Figure III-1.

143

Figure III-3: Plot of several event counting rates versus time for the OGO-6 instrument for one orbit. The curves of interest are described in the text. The scales for the counting rates are logarithmic with decades indicated by tickmarks. The plots are described in detail in the thesis of Murray (1970).

Figure III-3
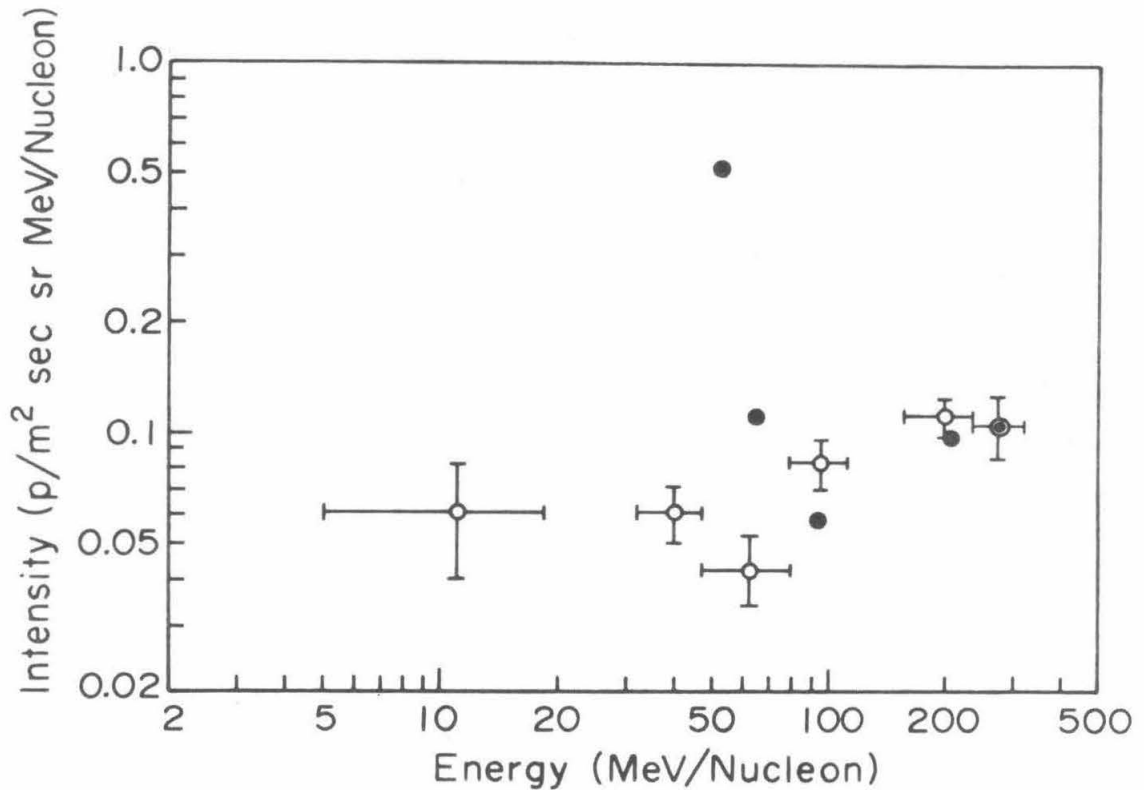
Figure IV-1

Differential energy spectra of He nuclei measured by pαe and OGO-6
for the same time period in 1969. The open circles represent OGO-6
data, the full circles represent pαe data. The error bars on the pαe
points are roughly the same size as those on the OGO-6 data. The pαe
points have been corrected for energy loss in the residual atmosphere
above the instrument, but they have not been corrected for attenuation
or production by nuclear interactions in the atmosphere.

146

Figure V-1: Deep River neutron-monitor counting rate versus time. The
arrows indicate times of balloon flights and the bars indicate periods
for which OGO-6 spectra have been calculated.
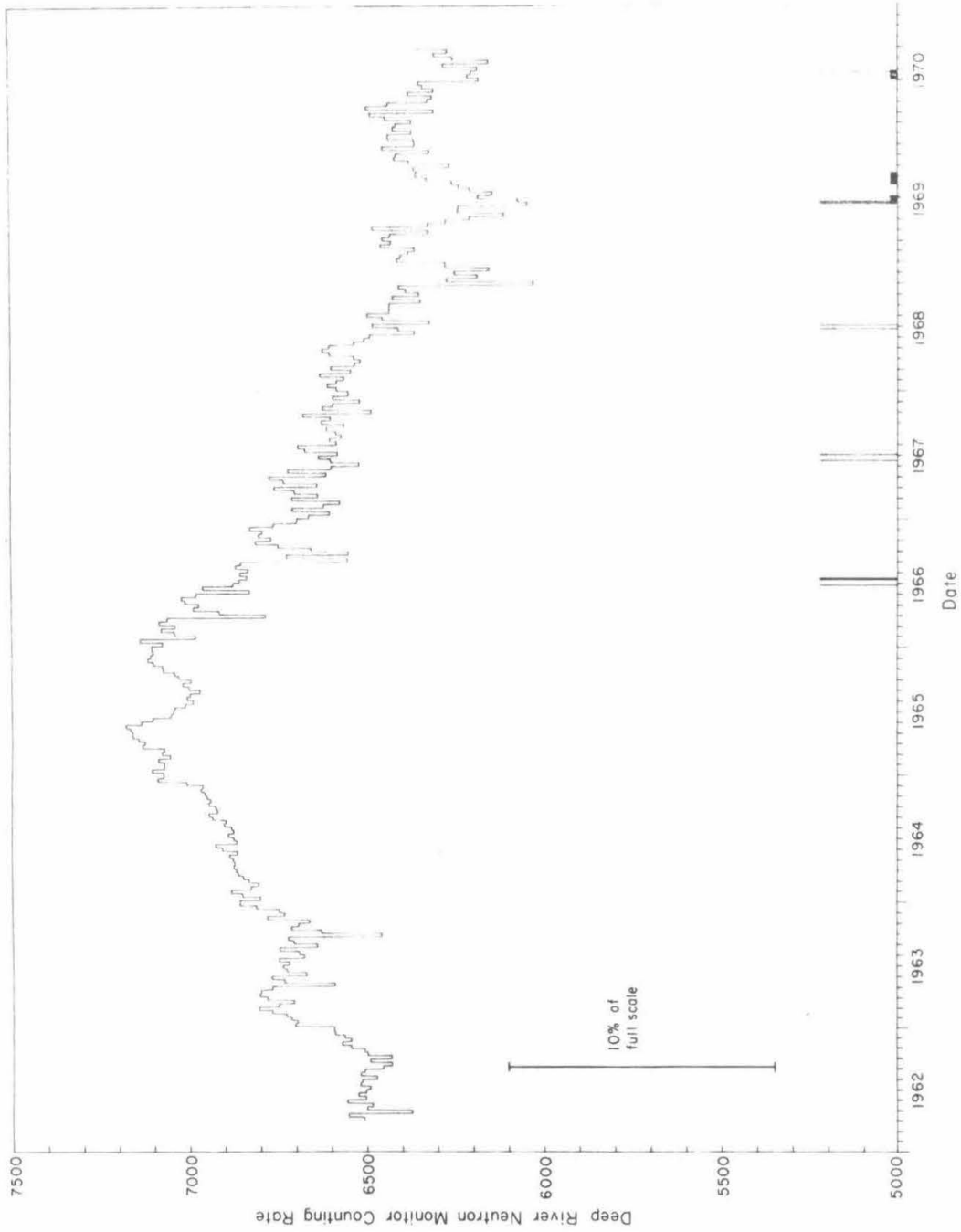
Figure V-1

Figures V-2a through f: Monthly summary plots used to select quiet periods in 1969 and 1970. For the indicated month the following information, starting at the top, is plotted vs. time:

1) The average polar $D1\overline{D8}$ counting rate in cts/sec (labelled D1) is plotted logarithmically. This rate is nearly insensitive to electrons but responds to nuclei from ~1.2 to ~20 MeV/nucleon.

2) The average polar $D2\overline{D8}$ counting rate in cts/sec (labelled D2) is plotted logarithmically. This rate responds to electrons $\gtrsim$ 200 keV and to nuclei $\gtrsim$ 3 MeV/nucleon.

3) The average polar $D1D2\overline{D8}$ counting rate in cts/sec (labelled D1D2) is plotted logarithmically. This rate responds to nuclei from ~3 to ~20 MeV/nucleon.

4) The average polar $D2D3\overline{D8}$ counting rate in cts/sec (labelled D2D3) is plotted logarithmically. This rate responds to electrons $\gtrsim$ 1 MeV and nuclei $\gtrsim$ 19 MeV/nucleon.

5) The > 10 MeV solar proton fluxes measured by the Solar Proton Monitoring Experiment aboard Explorer 41. This cosmic ray telescope, which is described briefly in the ESSA descriptive text, also has some electron sensitivity. The large rate excursions repeated at ~4.3 day intervals are due to the periodic passage of the satellite through the earth's radiation belts. These excursions have been largely suppressed by the plotting program.

6) Normalized hourly average counting rates for 2 neutron monitors: Alert (upper line) and Deep River.

7) The standardized K-index of geomagnetic activity from twelve observations are averaged to obtain K_p. The quasi-logarithmic K_p scale ranges from 0 (quiet) to 9 (very disturbed). The legend for the plots is identical to that adopted by ESSA.

8) Geomagnetic storm sudden commencements (labelled SC) are indicated by solid triangles if confirmed and by open triangles if unconfirmed.

9) Magnetogram sudden impulses (labelled SI) are indicated by solid diamonds if confirmed and open diamonds if unconfirmed.

10) Optical solar flares (labelled SOLAR FLARE) of importance greater than 2F observed by the world-wide system of solar observatories are indicated by a small vertical line plotted at the beginning time of the flare. The importance (2N, 3B, etc.) is included. Periods of no flare patrol are indicated by horizontal lines of appropriate length.

11) 2 - 12$\overset{o}{A}$ solar x-ray flares (labelled X RAY) with a peak flux at least 4 times the ambient value are indicated by a vertical line. These

data were collected by experiments aboard Explorers 33 and 35.

12) Occurrences of type-IV radio emission (labelled TP IV RADIO) are indicated by vertical lines. This radiation is normally associated with the acceleration of solar flare electrons.
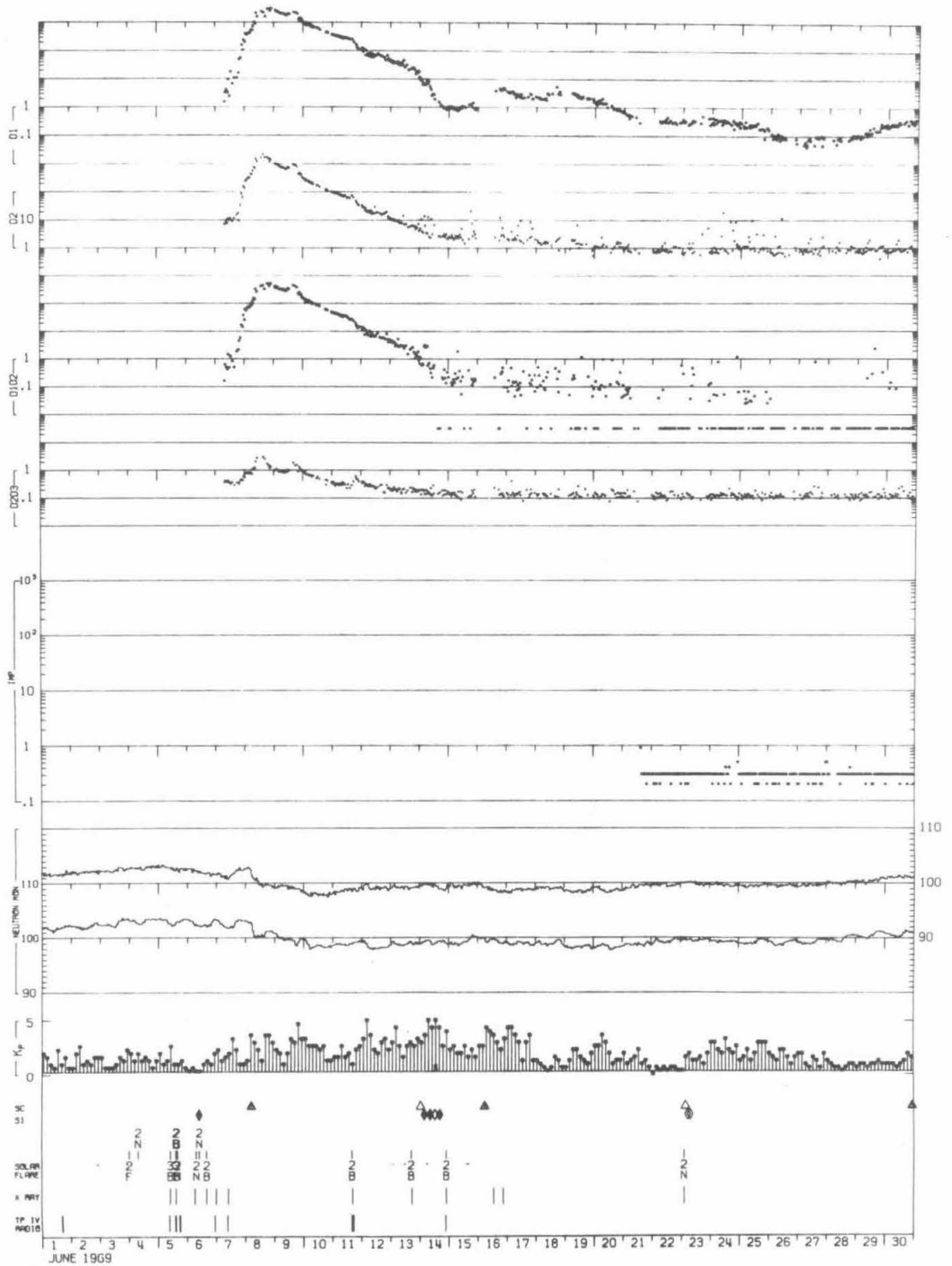
Figure V-2a

Figure V-2b

152

Figure V-2c

153
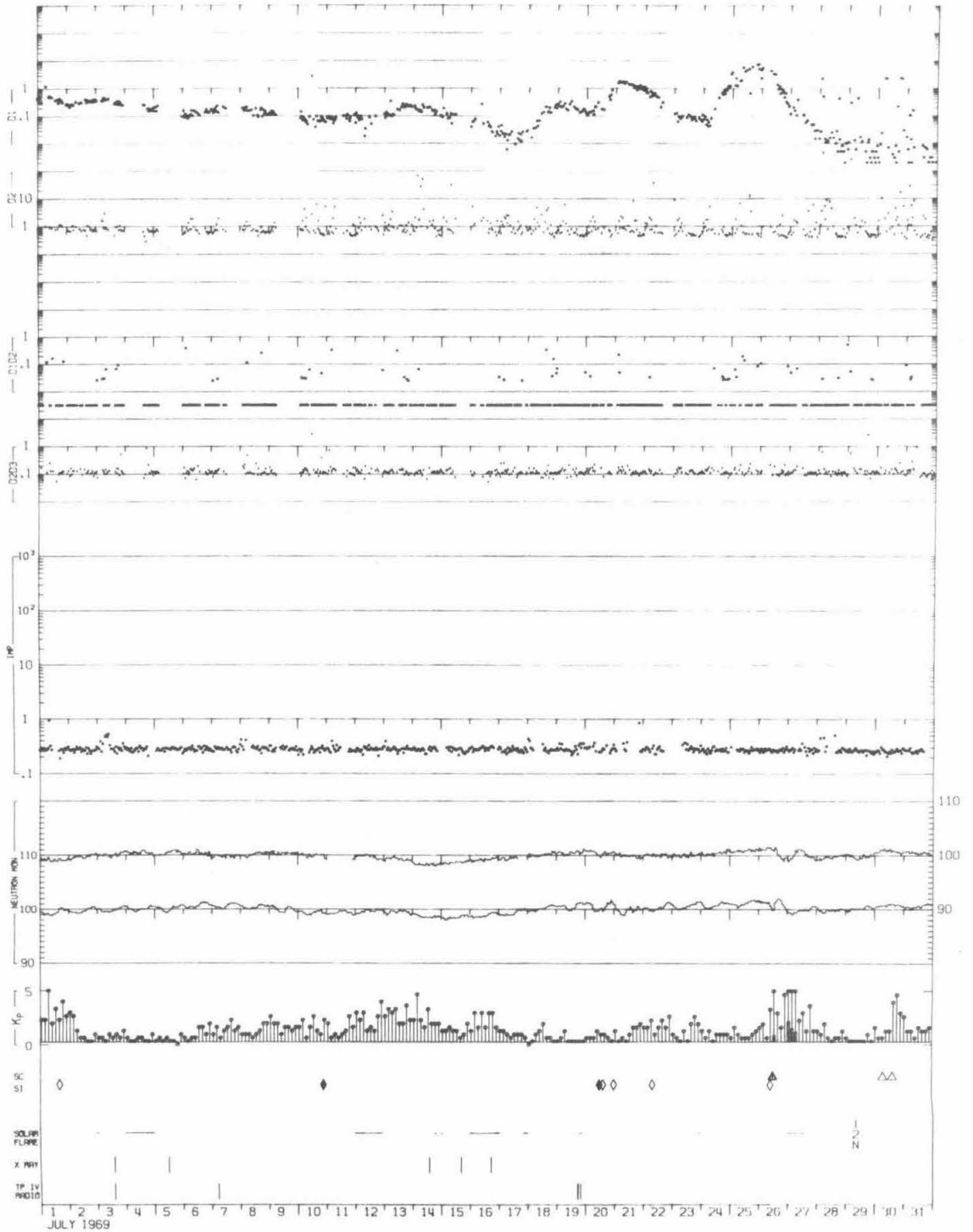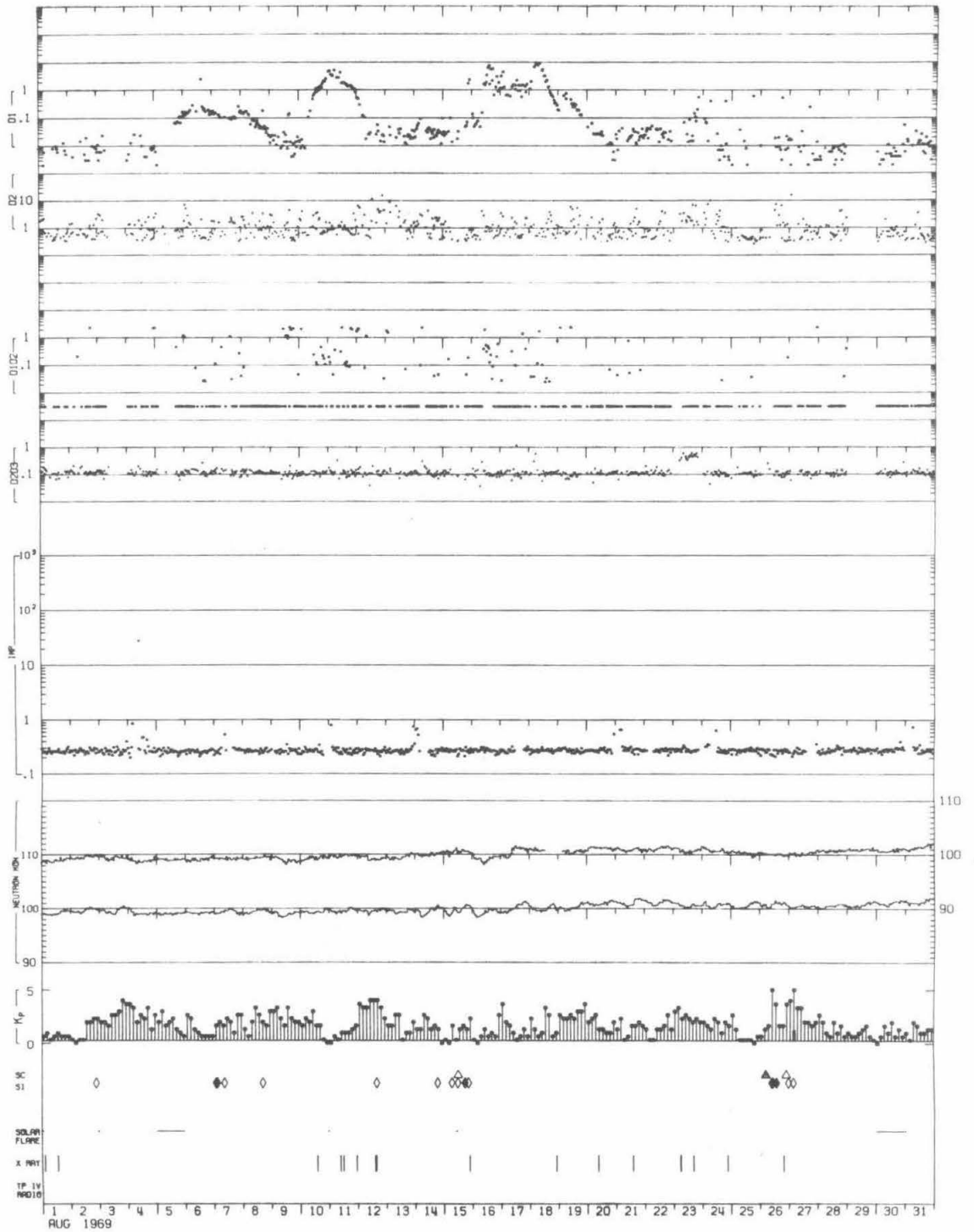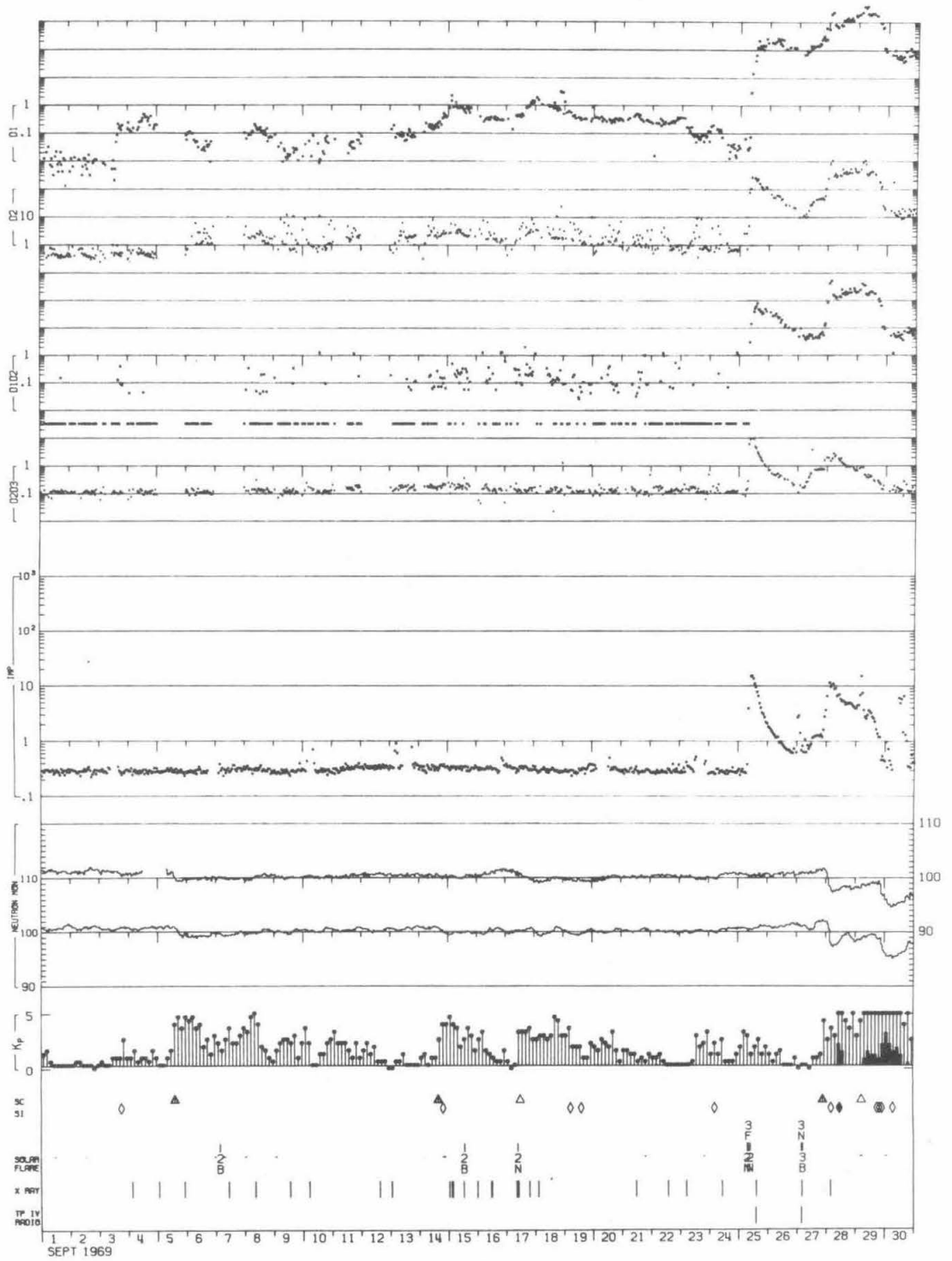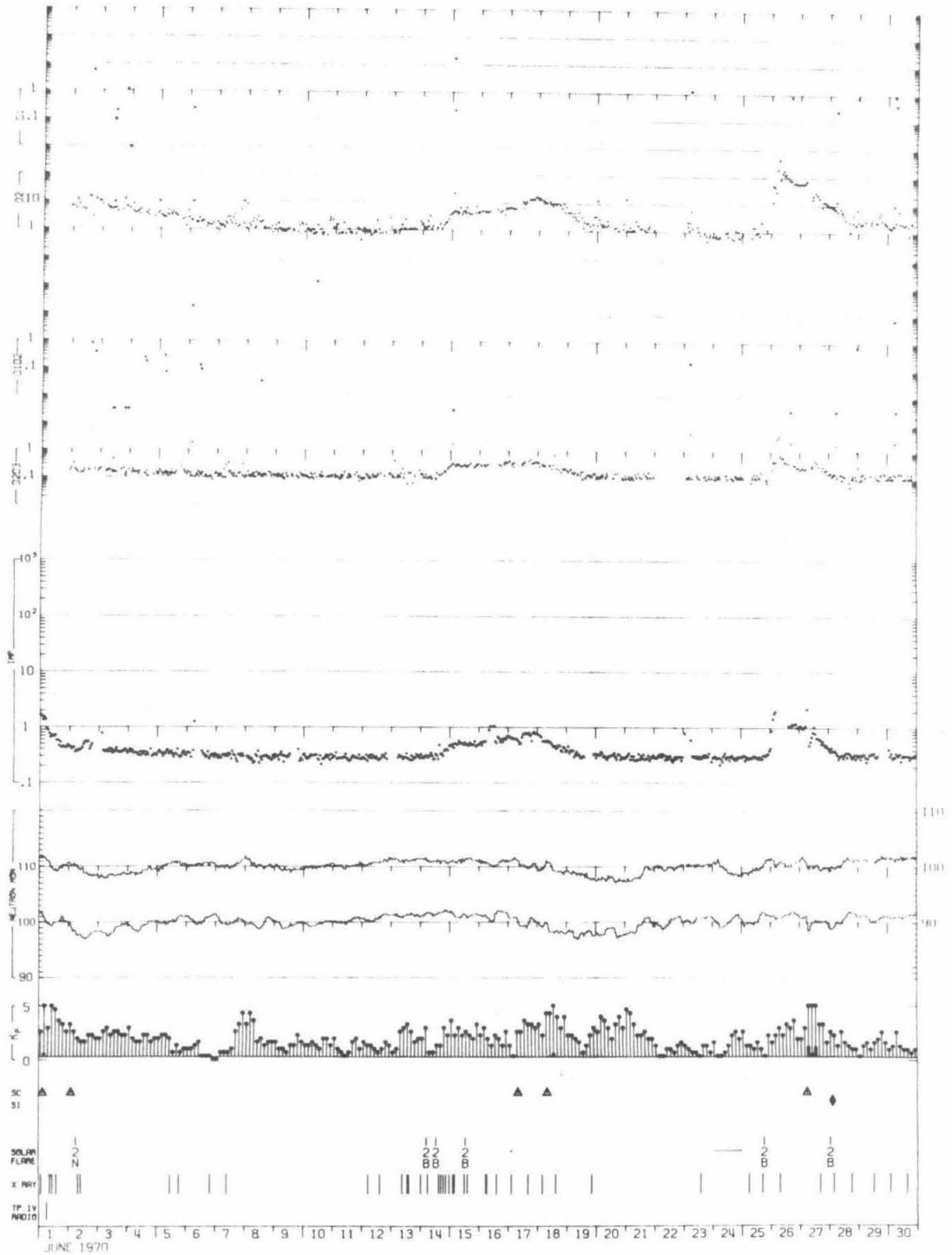
Figure V-2d

Figure V-2e
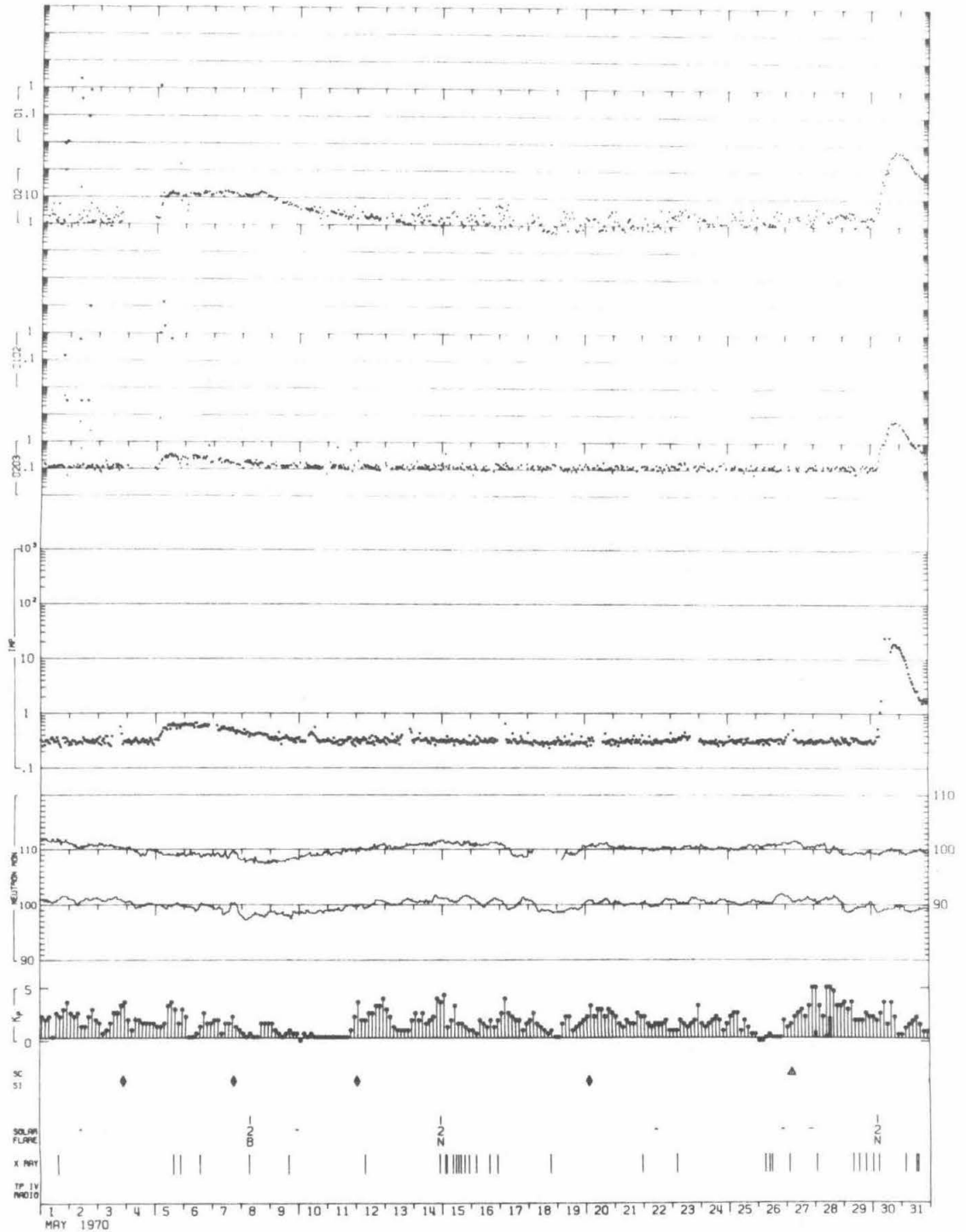
Figure V-2f
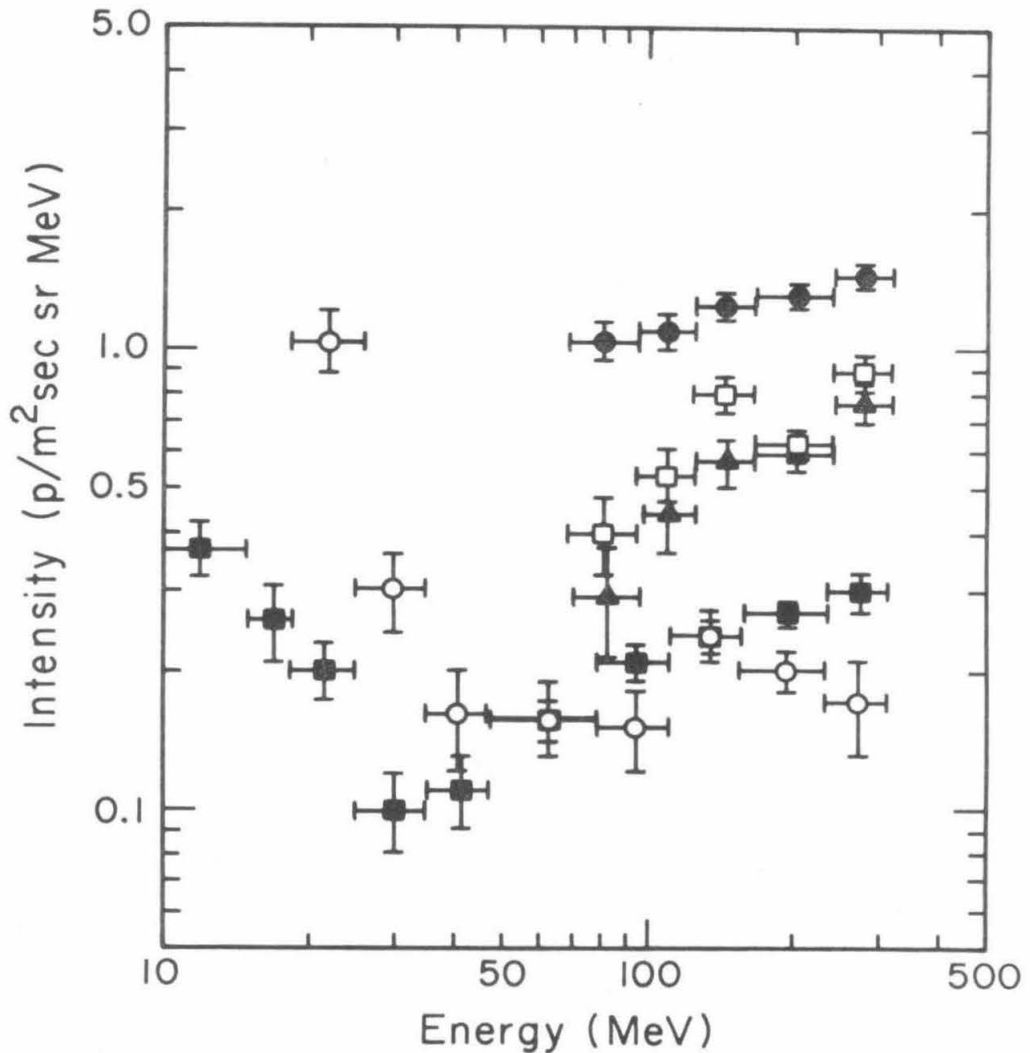
Figure V-3

The differential intensity spectra of protons for solar quiet times in the years 1966 through 1970. The full circles represent the 1966 spectrum, the open squares 1967, the triangles 1968, the full squares 1969, and the open circles 1970. (See table V-1). The vertical error bars indicate one standard deviation assuming Gaussian statistics.

157
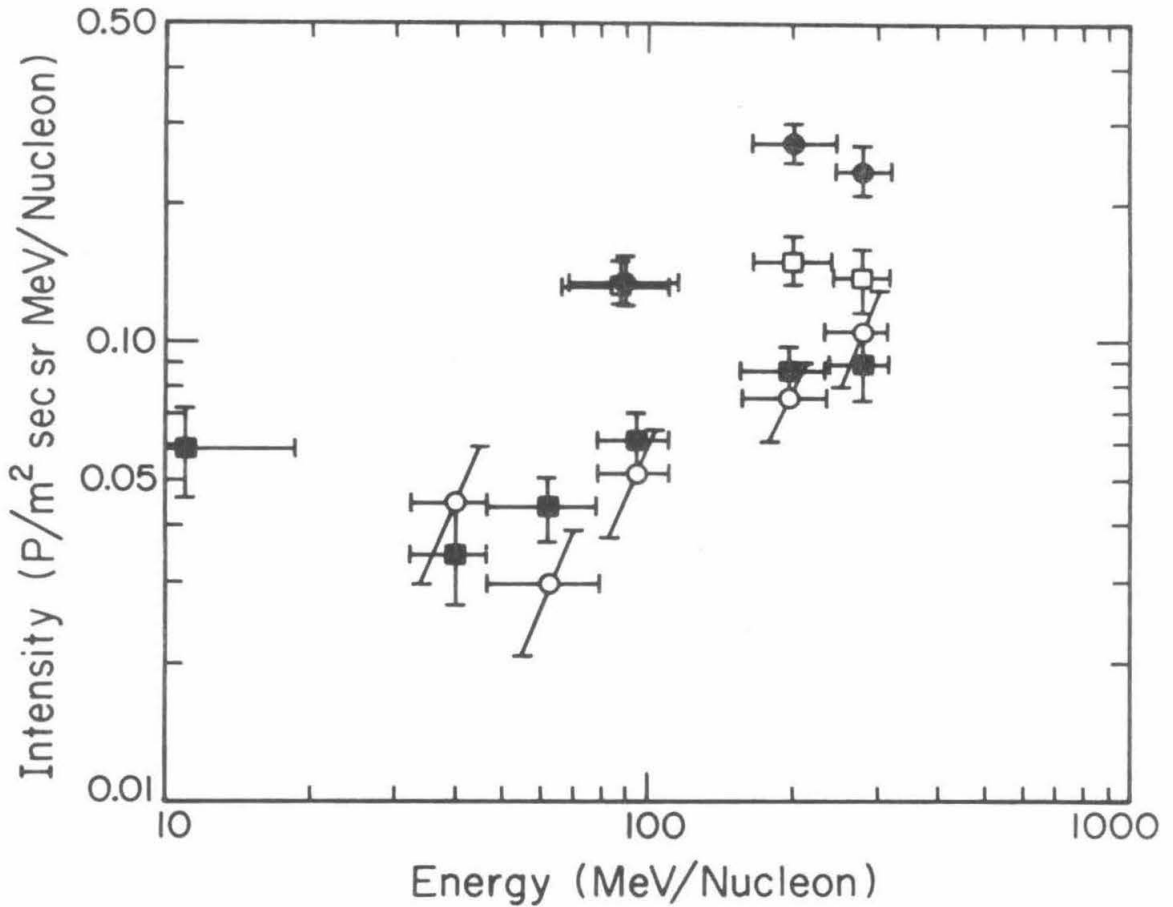
Figure V-4

The differential intensity spectra of He nuclei for solar quiet times
in the years 1966 through 1970. The full circles represent the 1966
spectrum, the open squares the 1967-68 spectrum (averaged for lack of
data), the full squares 1969, and the open circles 1970. (See Table V-2.)
The vertical error bars represent one standard deviation assuming Gaus-
sian statistics.
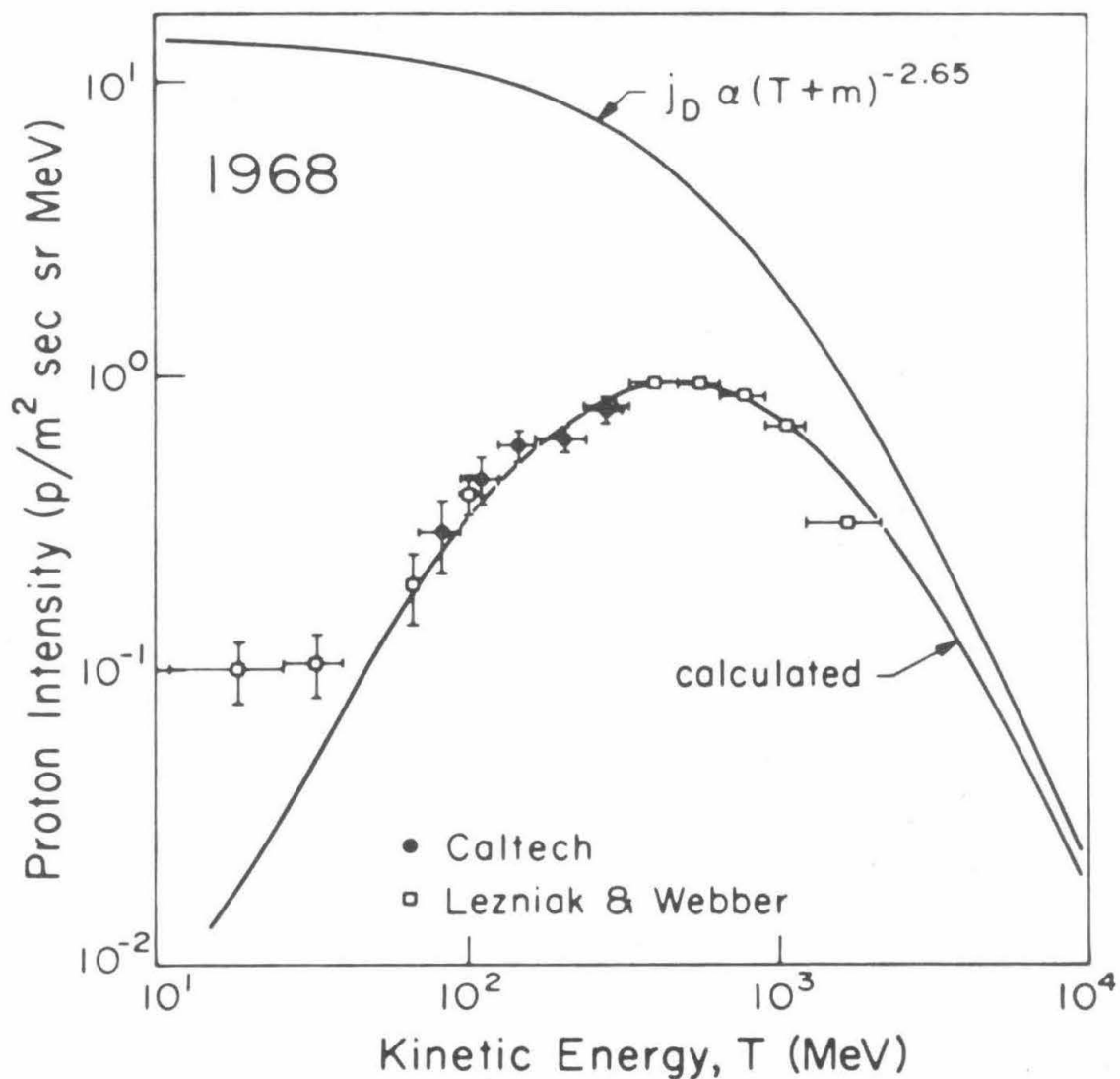
Figure VI-1

Calculated and measured proton spectra for 1968. The upper curve is
the input (interstellar) spectrum assumed for the calculation. The
reader should keep in mind that (as will be discussed later) even
though the input spectrum is plotted over the same energy range as the
spectrum at Earth, the solution is not sensitive to the low-energy
portion of the input spectrum.

Figure VI-2: Some of the rigidity, R, and heliocentric-radius, r, dependences of the diffusion coefficients used in this thesis are illustrated. The velocity of the particle, β, has been factored out of the energy dependence. The $\sqrt{R}$ dependence illustrated by the solid line at low rigidities gives a better fit to the observed spectra than the R^0 dependence shown by the dashed line. The R^0 dependence was sometimes used to facilitate making calculations with the force-field model.

160
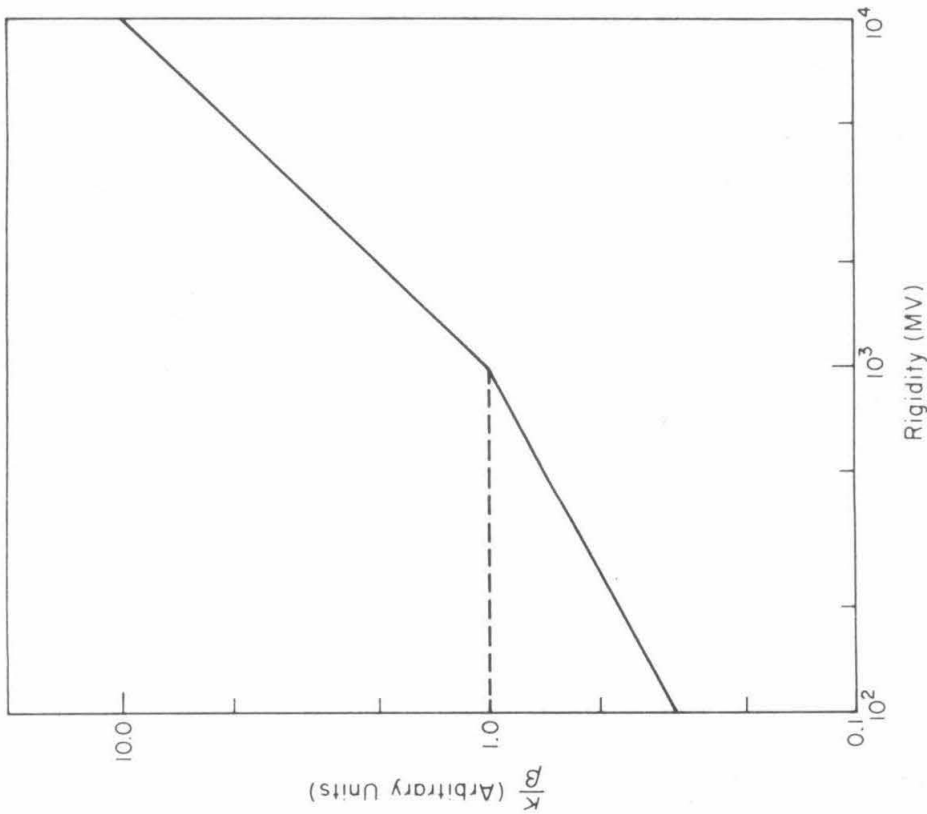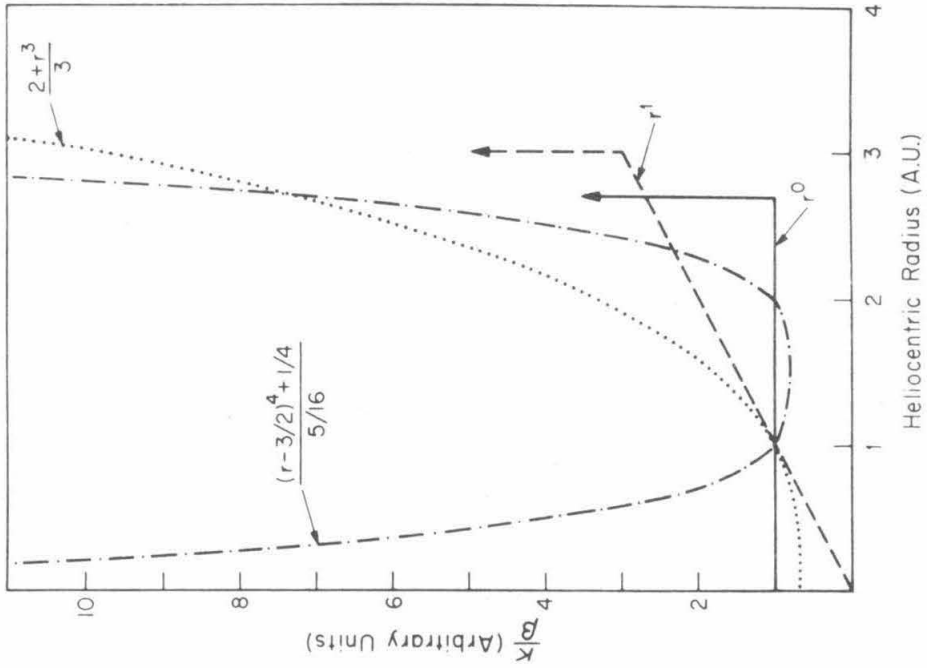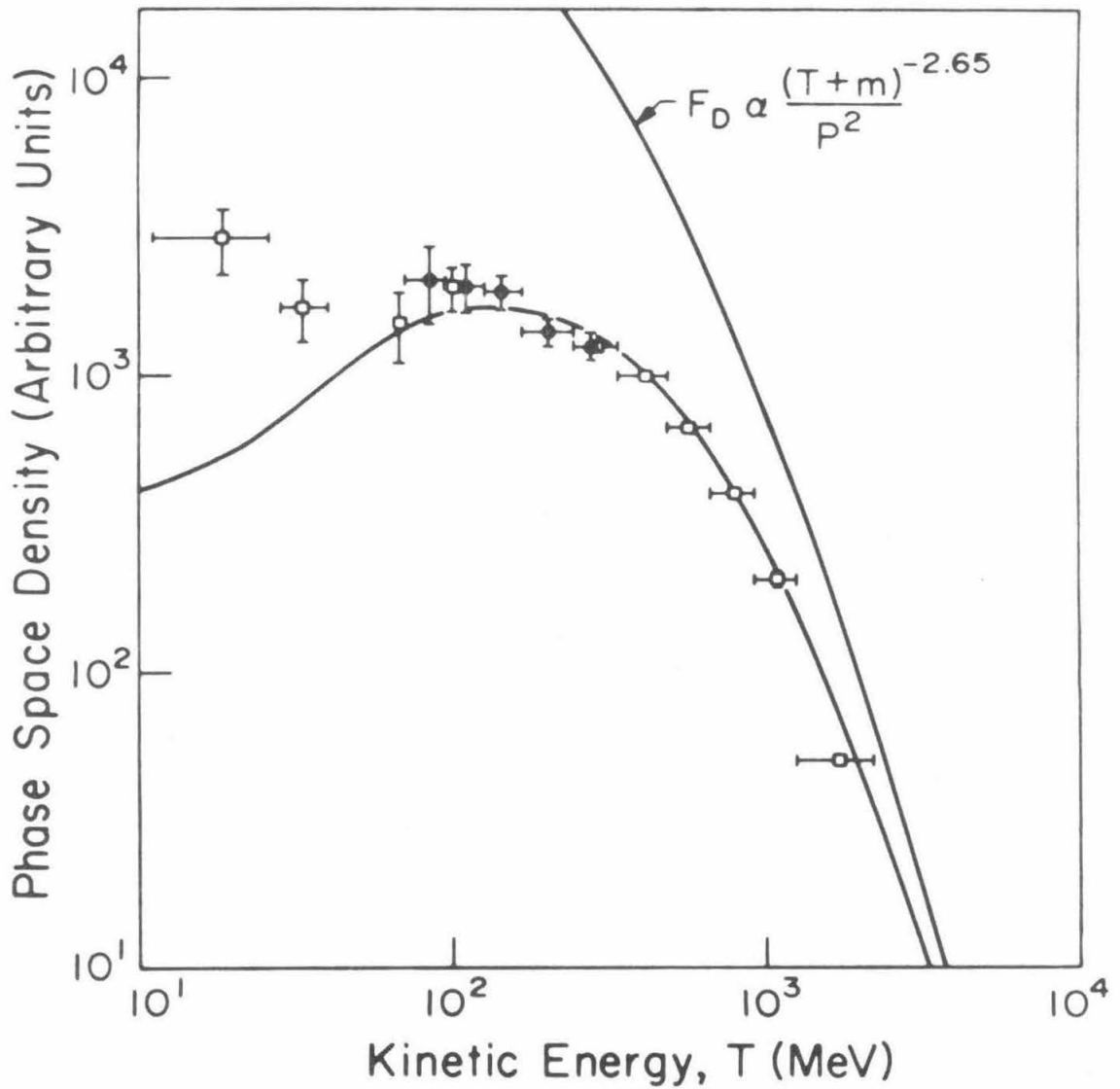
Figure VI-2

Figure VI-3

Calculated and measured proton spectra for 1968 as in Figure VI-1.
In this figure the ordinate is phase-space density, F, rather than
intensity.

Figure VI-4:   Illustration of the dependence of the phase-space density, F, on the two variables, heliocentric radius, r, and kinetic energy, T. Figure VI-4a is a plot of F versus T at r = 1 A.U. Figure VI-4B is a plot of F versus r at 50 MeV. Figure VI-4c is a perspective plot of F versus r and T. The heavy lines indicate the cross-sections which are shown in a and b.
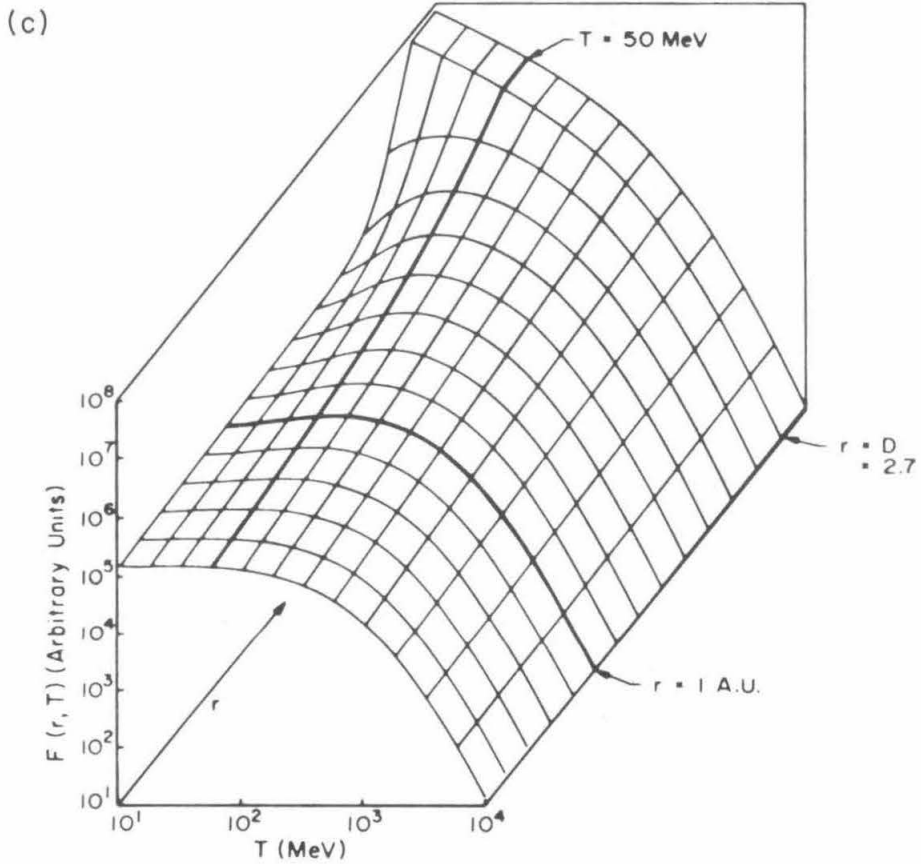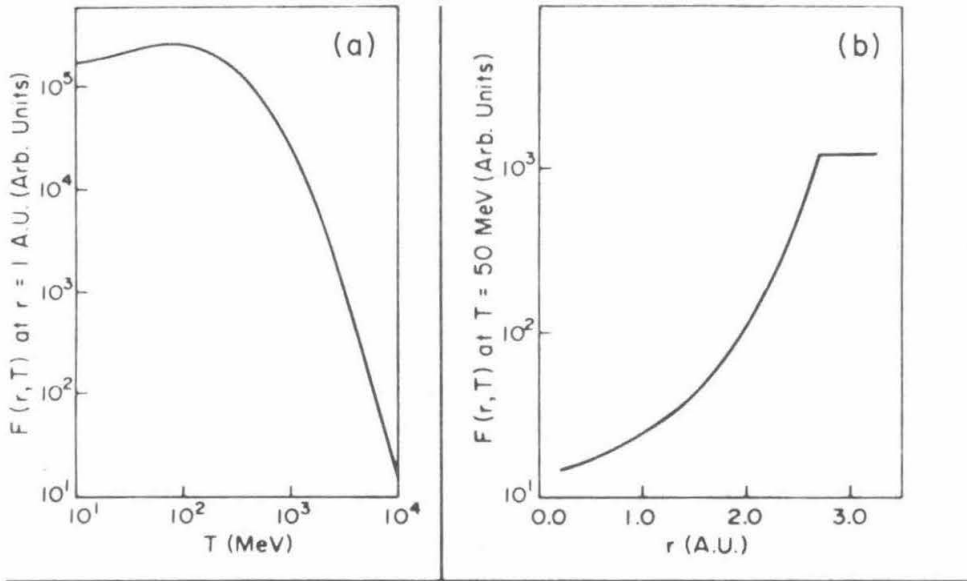
Figure VI-4

Figure VI-5: Contour lines of constant phase-space density in the radius-energy plane. The radial and rigidity dependence of the diffusion coefficient is indicated on the contour plot and is schematically illustrated in Figure VI-2. The dotted line is the $\psi = 2.5$ contour line and is intended to separate the r-T plane into two regions -- large- and small-modulation regions.

Figure VI-5a&b

166
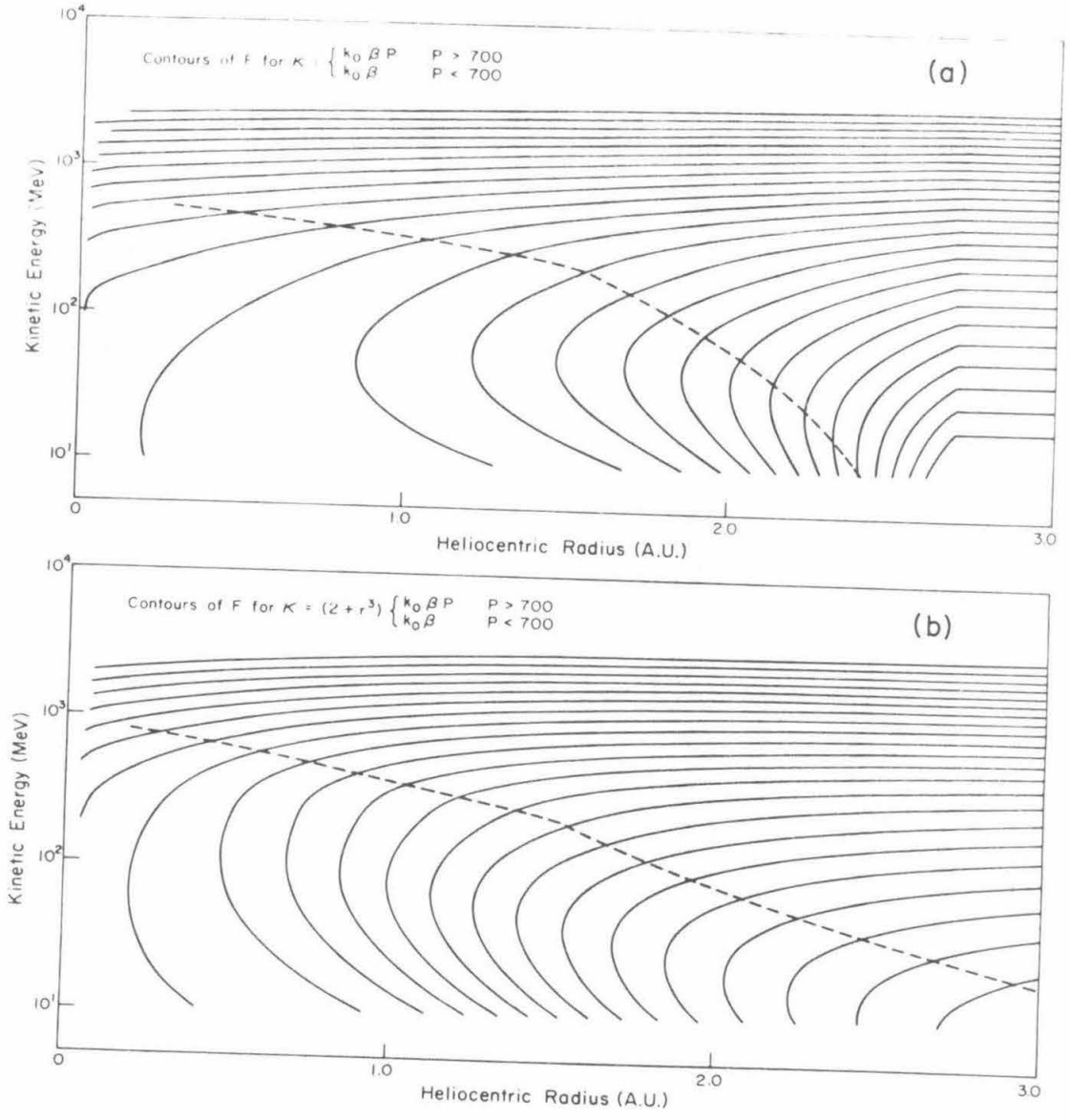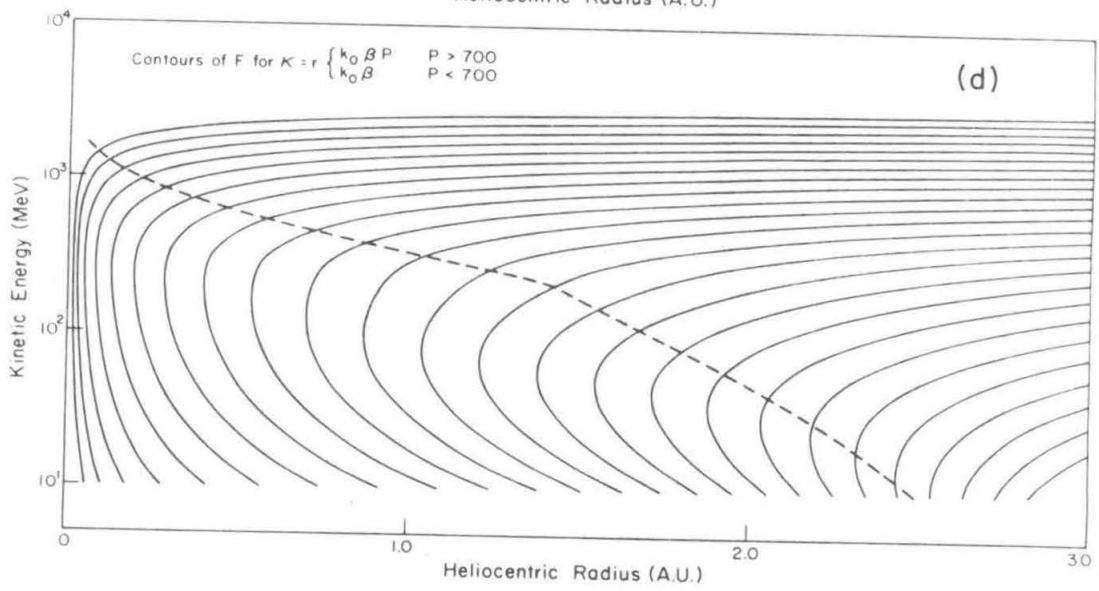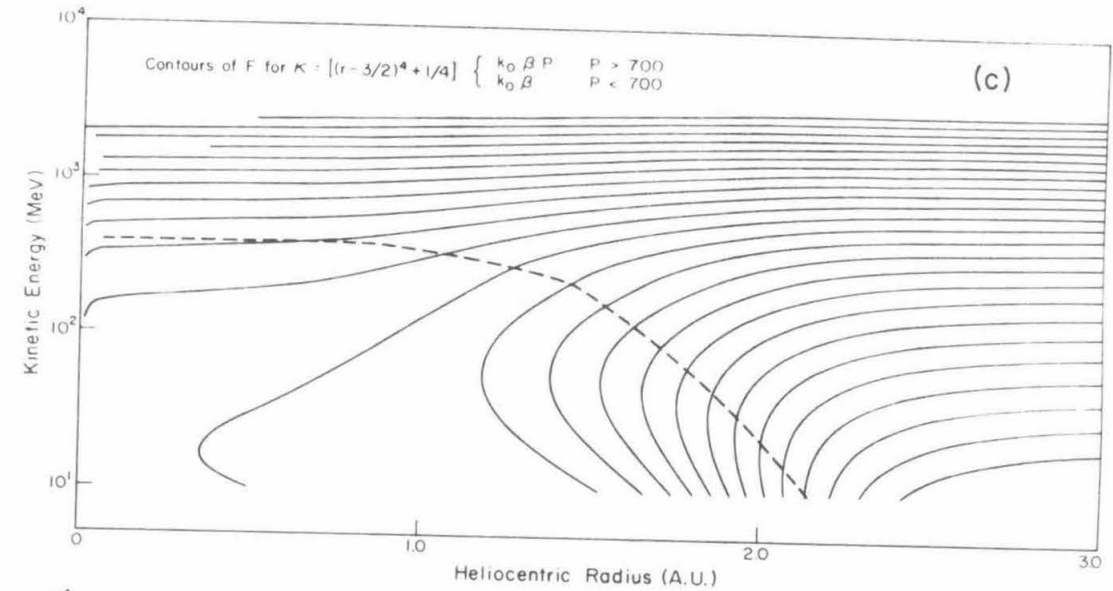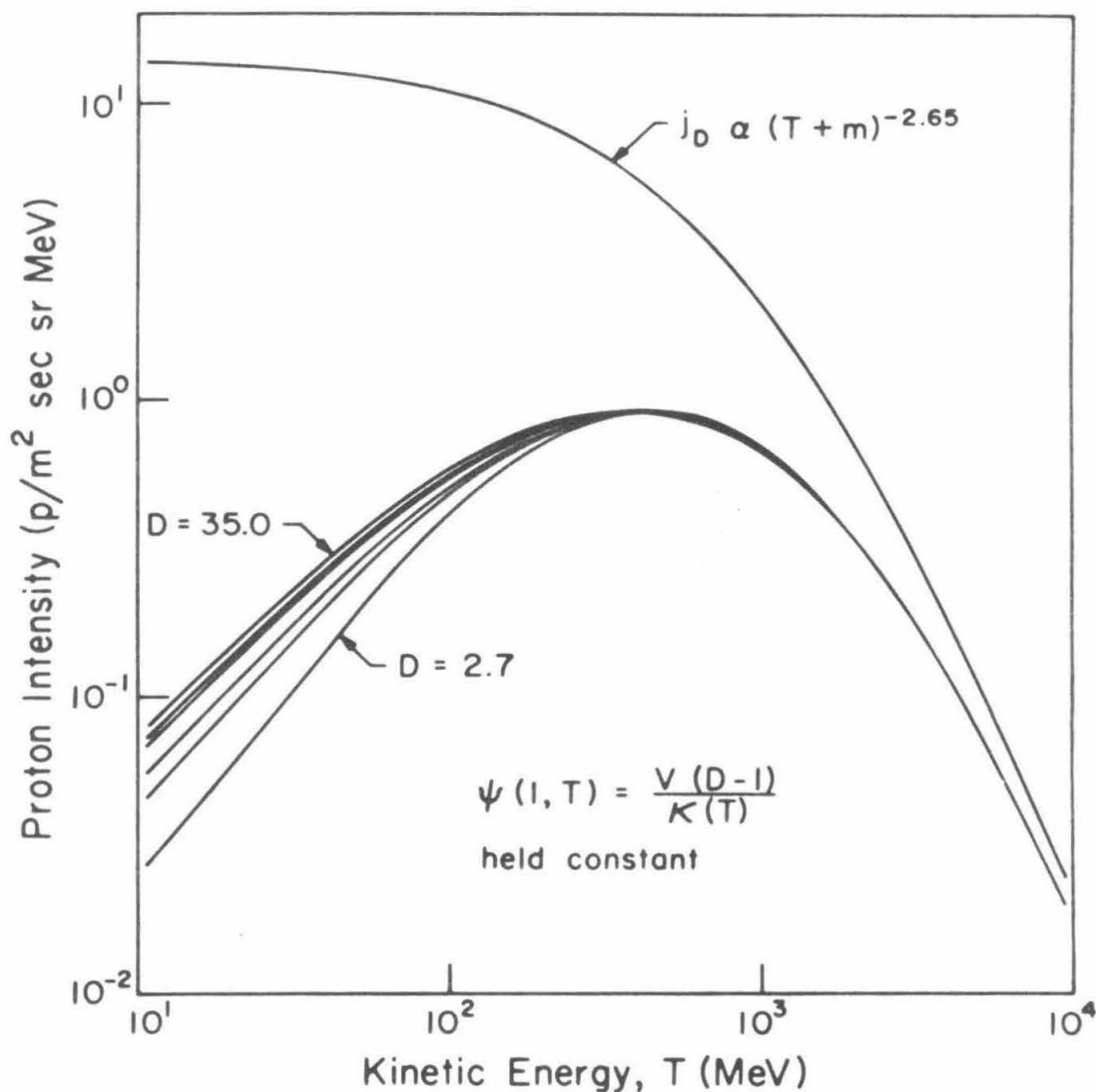
Figure VI-5c&d

Figure VI-6

Calculated spectra of protons at Earth for various values of the boundary
distance, D. The upper curve is the input spectrum, the lower curves
are calculated for various values of D. The magnitude of the diffusion
coefficient, κ, is scaled to keep the modulation parameter, ψ, constant
at Earth. The rigidity dependence of κ is the same for all curves in
this plot. The D values used are 2.7, 4.4, 6.1, 12.9, 18.0, and 35.0
A.U. The curves corresponding to 2.7 A.U. and 35.0 A.U. are labeled
and the intermediate curves form a monotonic sequence.
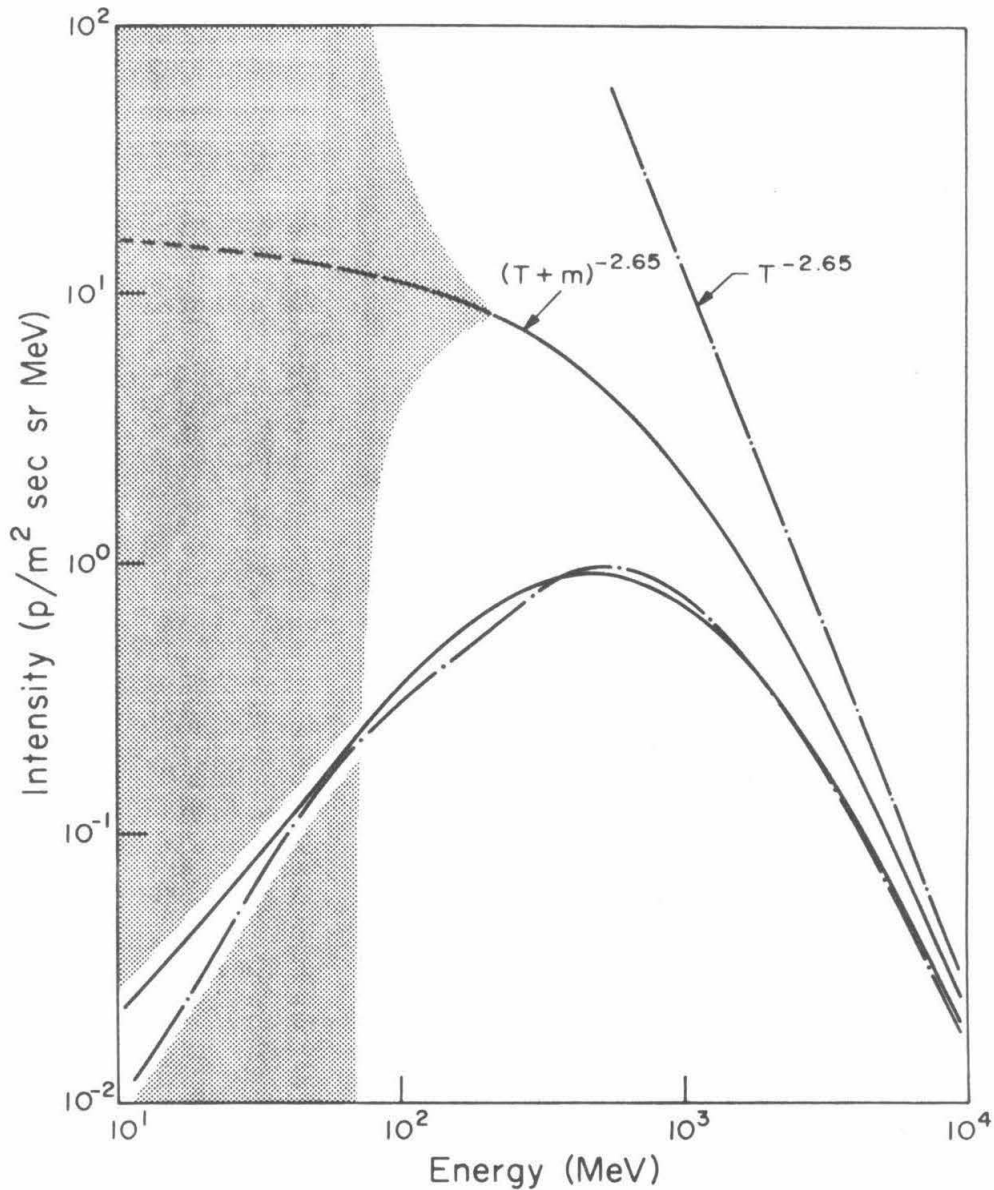
Figure VI-7

Calculated spectra of protons at Earth for various interstellar spectra. The dash-dot curves and the solid curves form corresponding pairs of interstellar and Earth spectra. The two calculated spectra are both good fits to the measured proton spectrum for 1968 (see again Figure VI-1). The diffusion coefficient used with the kinetic-energy power-law input spectrum is roughly a factor of 3 smaller than the diffusion coefficient used with the total-energy power-law input spectrum. The shaded area with the total-energy power-law spectrum indicates schematically the range of values of the intensity in interstellar space which would yield the same spectrum at Earth without changes in the diffusion coefficient.

Figure VI-8: Three examples of radial intensity gradients calculated for characteristic sets of parameters. In each case κ is adjusted so that the calculated spectrum at Earth is roughly the same as that measured in 1968. The radial gradient is plotted as a function of radius for two different energies, 25 MeV and 500 MeV. At low energies the gradient is small and essentially independent of κ or j_D. The gradient at large energies is roughly inversely proportional to κ.
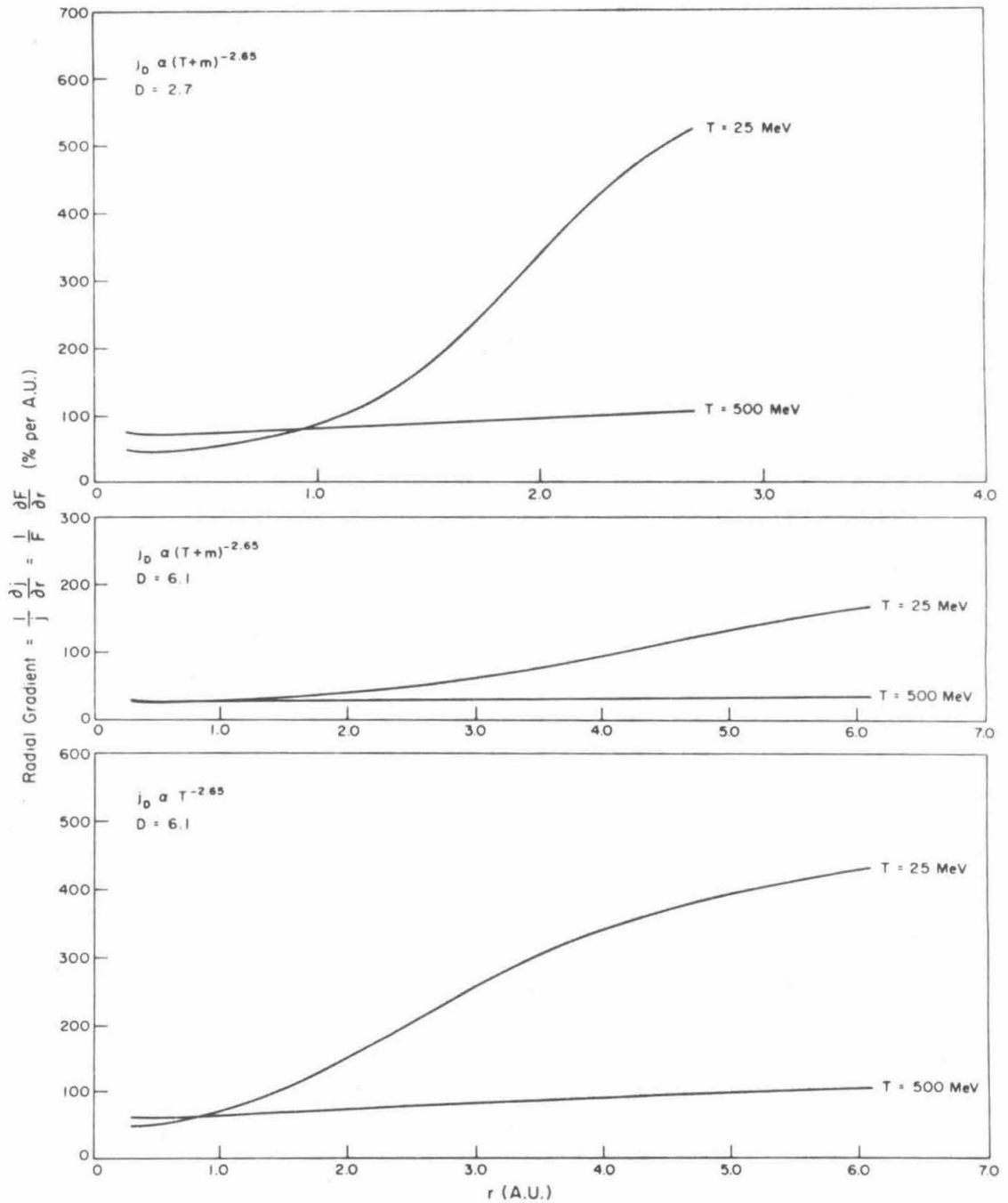
Figure VI-8

Figure VI-9: Contour lines of the radial component of the anisotropy are plotted in the r-T plane. The value associated with each contour line is indicated on the plot. The arrows are intended to remind the reader of the sense of flow associated with the sign of the anisotropy.
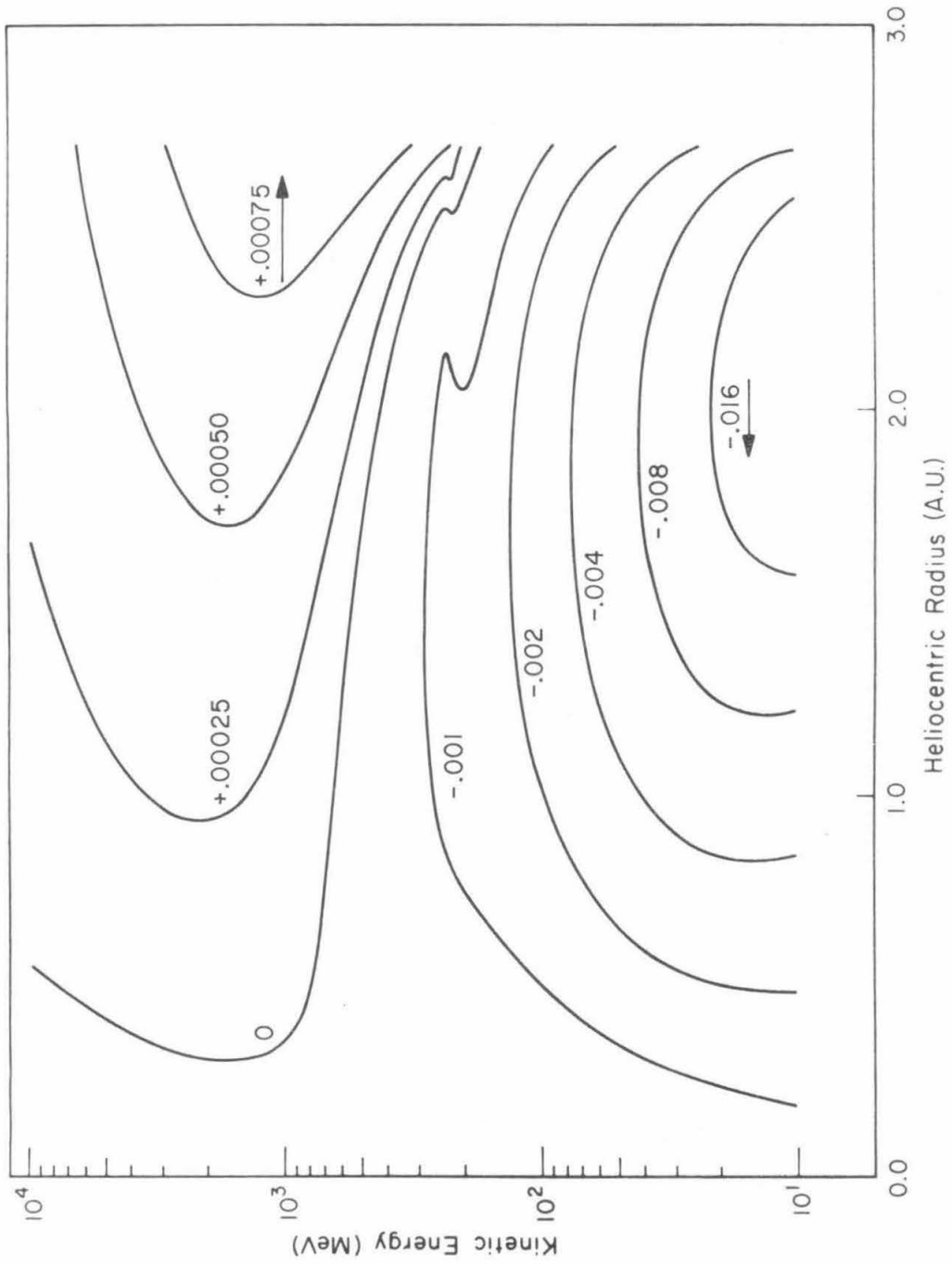
Figure VI-9

Figure VI-10: Calculated spectra of protons (a) and alpha particles
(b) at Earth for the four epochs -- 1965-66, June-October 1968, June-
July 1969, and June-July 1970 -- which correspond to the entries num-
bered 2, 4, 5, and 8 in Table VI-1, i.e., those determined from the
electron data. The assumed interstellar spectra shown are of the form
$j_D \propto (W - 0.25m)^{-2.65}$. The dashed curves correspond to a boundary
distance of 6.1 A.U. and the solid curves, to 2.7 A.U. The reader is
cautioned that, even though the input (interstellar) spectra are plotted
over the same energy range as the spectra at Earth, the calculated spec-
tra are not sensitive to the low-energy portion of the input spectra.
The range of uncertainty is schematically indicated by the shaded area
in Figure VI-7.
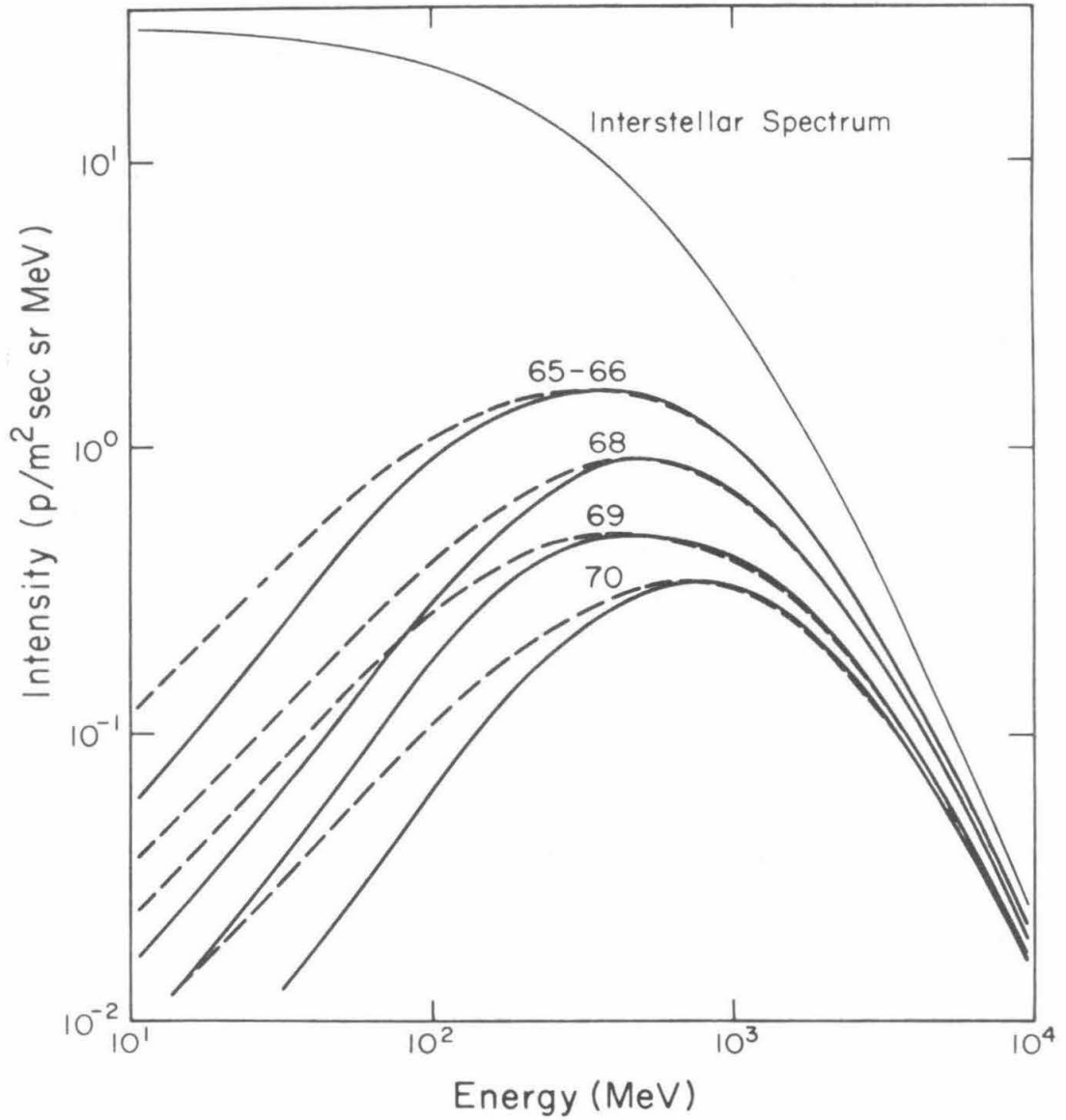
Figure VI-10a
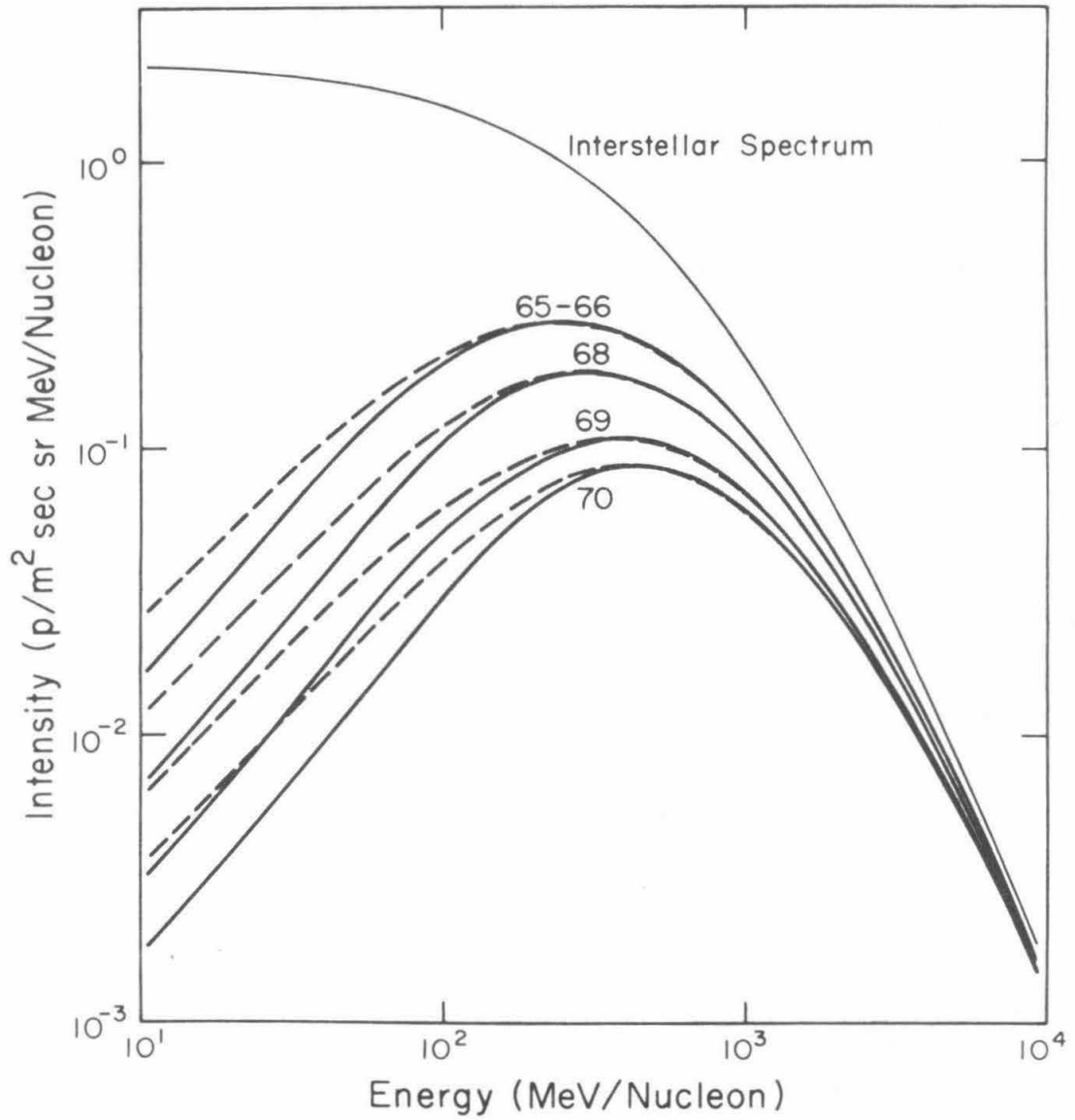
Figure VI-10b

Figure VI-11: The measured spectra of protons are compared with the most appropriate (nearest in time) of the calculated spectra shown in Figure VI-10a. The dashed curve is calculated for a boundary distance of 6.1 A.U. and the solid curve, for 2.7 A.U. The measured spectra are represented by points. The Caltech data are represented by full circles and are discussed in Chapter V. (VI-11a) The observational data are from the collection of Gloeckler and Jokipii (1967). Not all of the observations were made in 1965 but they should all be roughly appropriate to solar minimum. The calculation is based on entry number 2 in Table VI-1. (VI-11b) The triangles are from Fan et al. (1968). The calculated spectra are again for entry number 2 in Table VI-1. (VI-11c) The open squares are from Hsieh (1970). The calculation is based on entry number 4 in Table VI-1. (VI-11d) The open squares are from Lezniak and Webber (1971). The calculated spectra are for entry number 4 in Table VI-1. (VI-11e) The open squares are from Hsieh et al. (1971). The calculated spectrum is for entry number 5 in Table VI-1. (VI-11f) The calculated spectra are for entry number 8 in Table VI-1.

Figure VI-11a

1966

Interstellar Spectrum

Intensity (p/m^{2}sec sr MeV)

10^1

10^0

10^{-1}

10^{-2}

10^1 10^2 10^3 10^4

Energy (MeV)
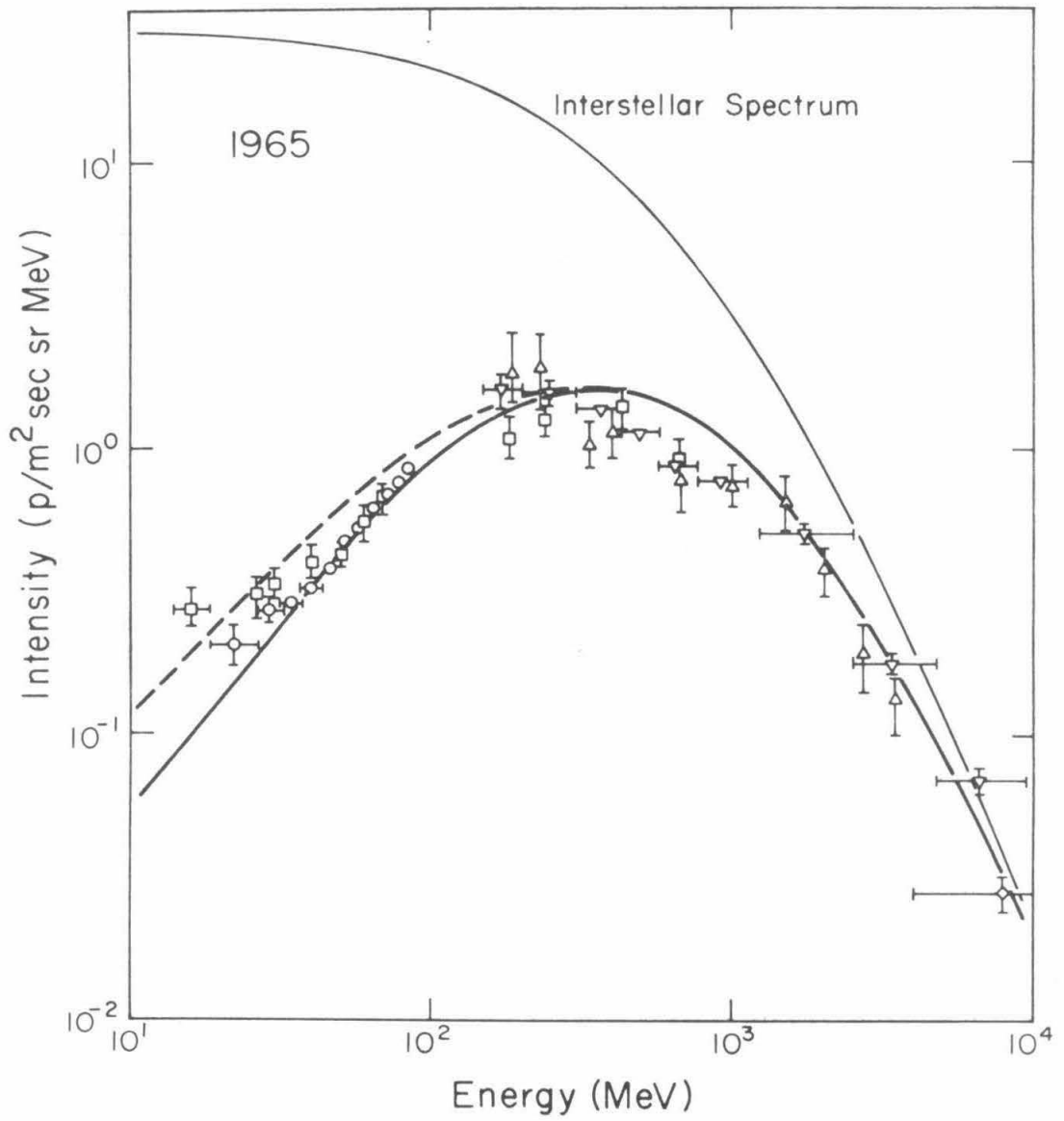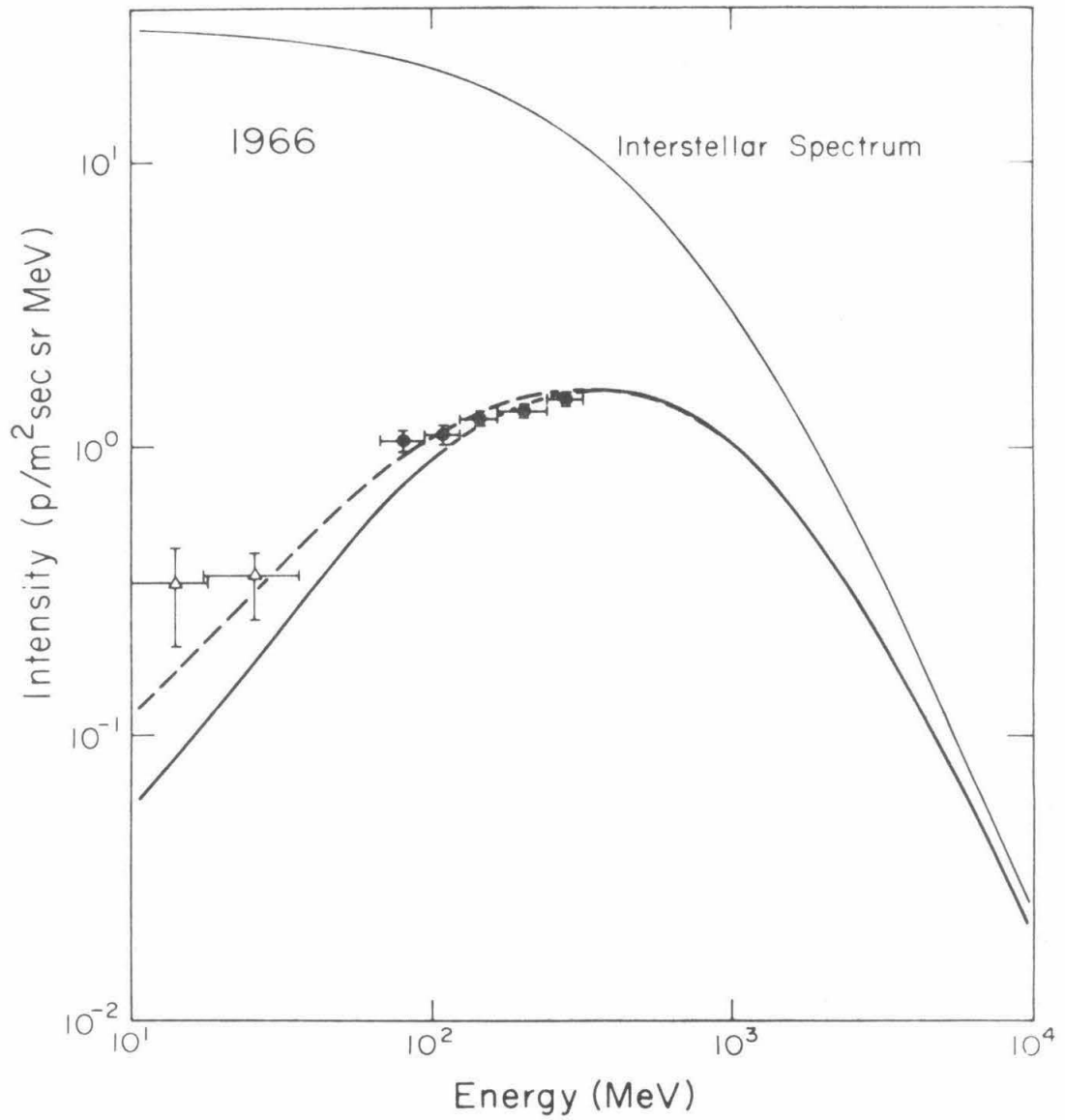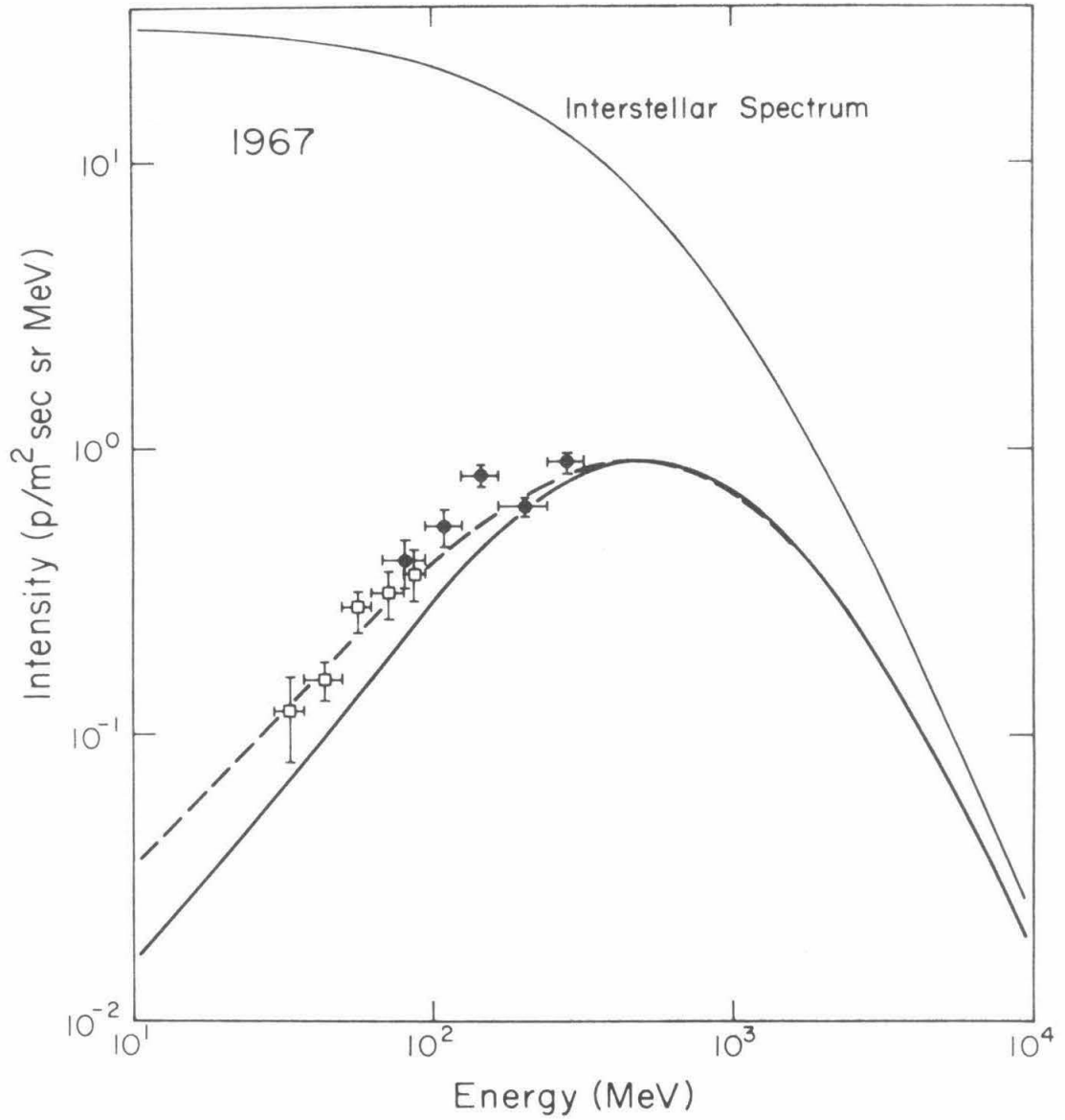
Figure VI-11b

Figure VI-11c
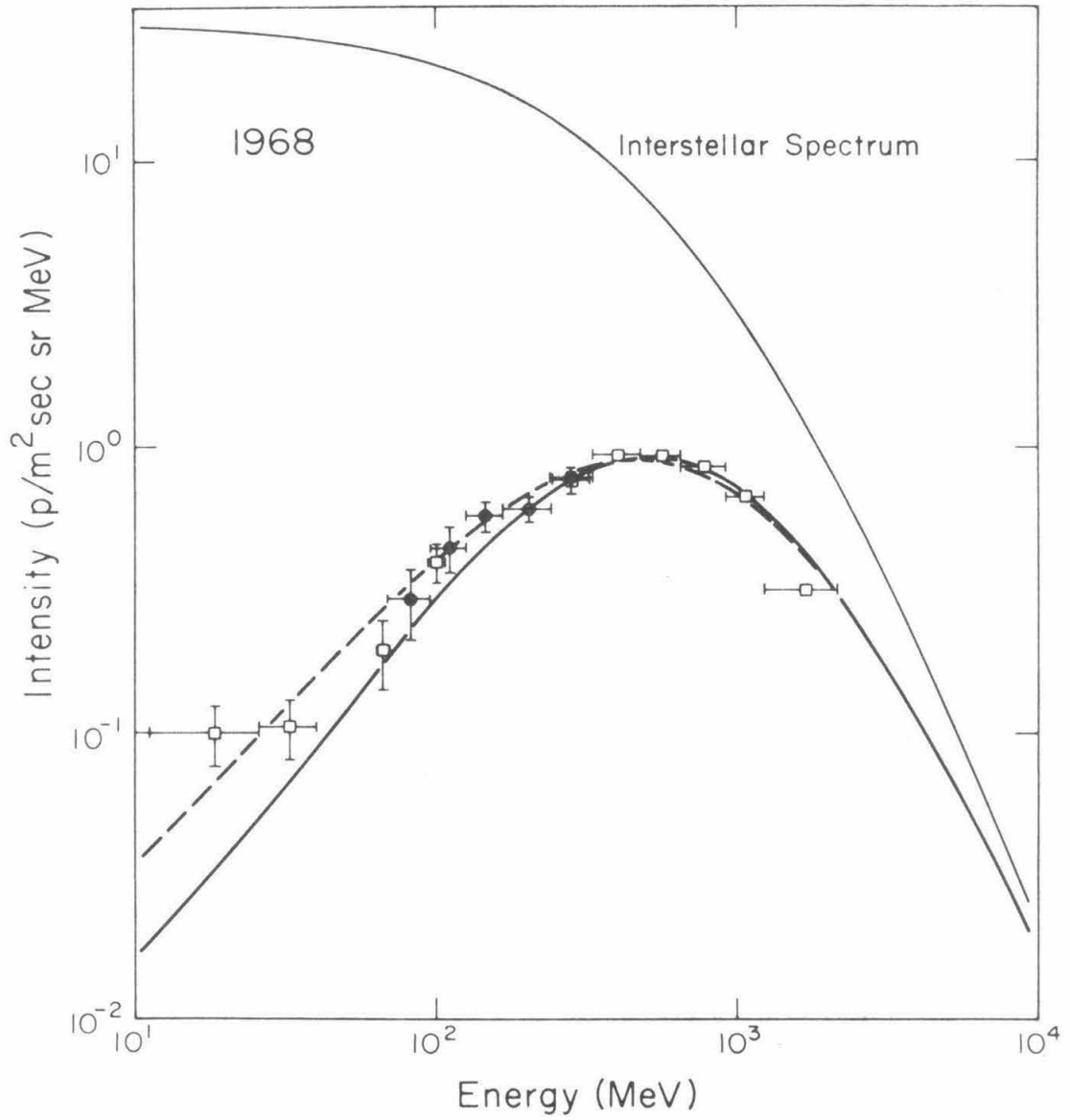
Figure VI-11d

Figure VI-11e

182
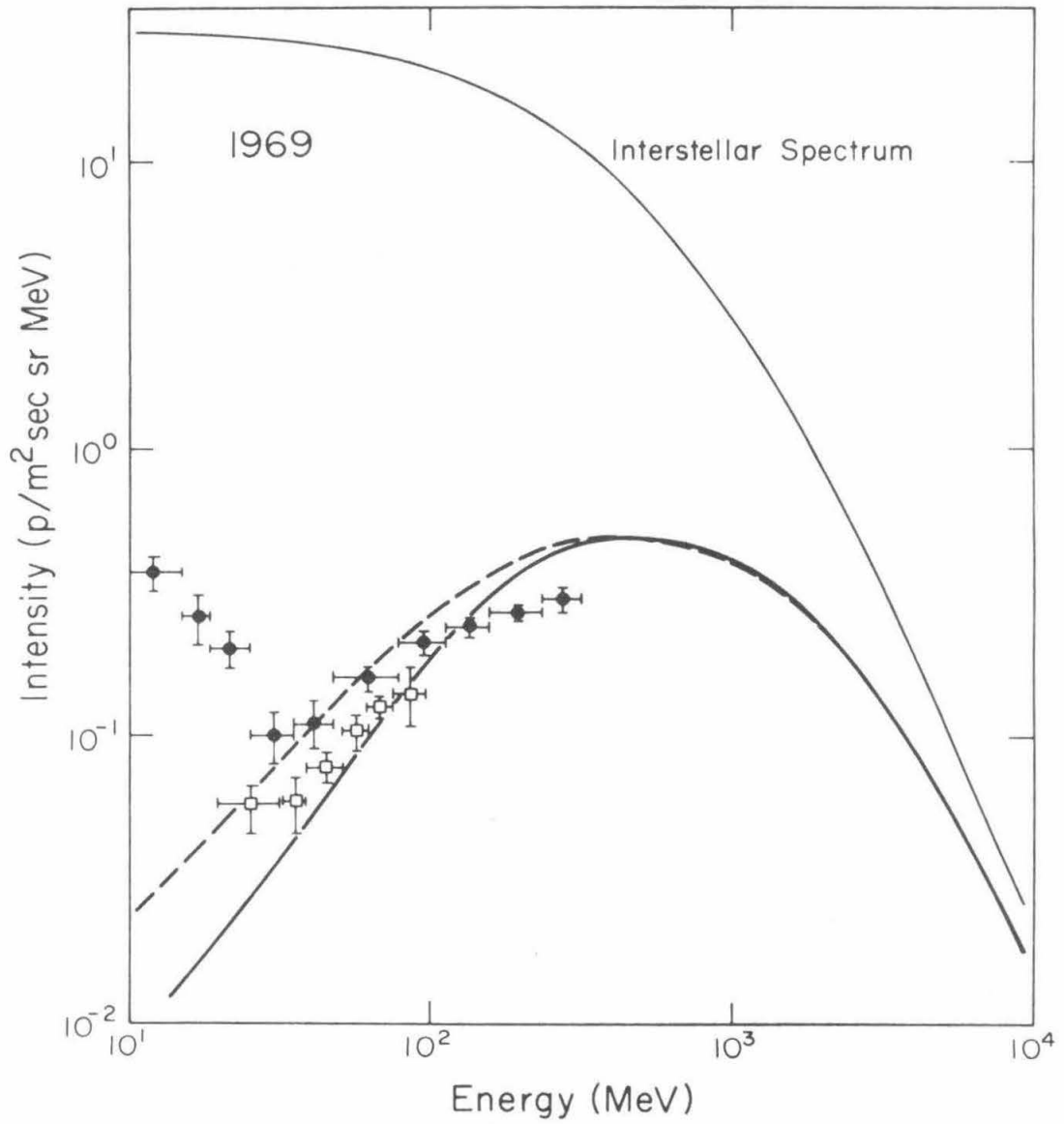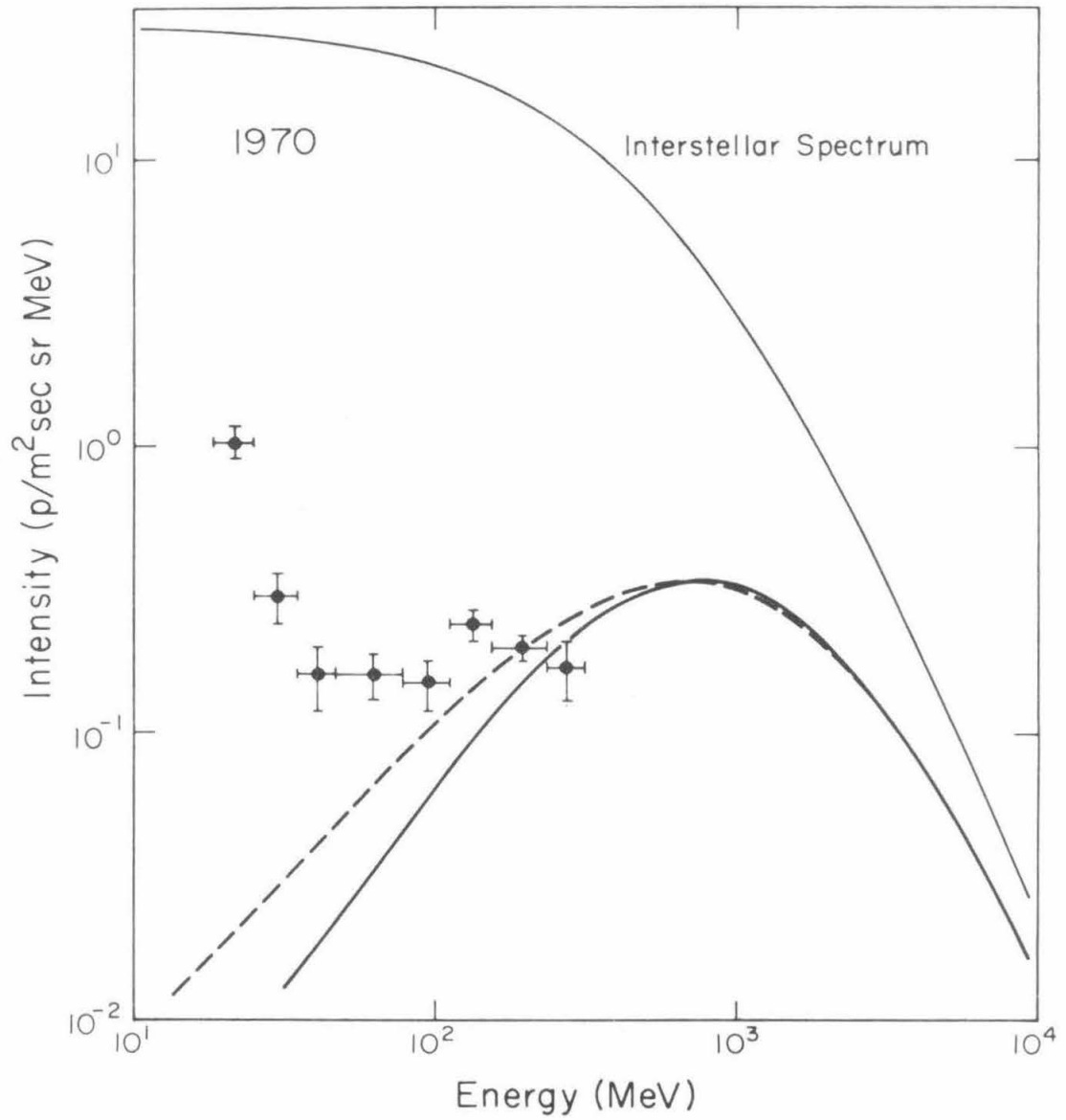
Figure VI-11f

Figure VI-12: The measured spectra of He nuclei are compared with the most appropriate (nearest in time) of the calculated spectra shown in Figure VI-10b. The dashed curve is calculated for a boundary distance of 6.1 A.U. and the solid curve, for 2.7 A.U. The measured spectra are represented by points. The Caltech data are represented by full circles and are discussed in Chapter V. (VI-12a) The observational data are from the collection of Gloeckler and Jokipii (1967). Not all of the observations were made in 1965 but they should all be roughly appropriate to solar minimum. The calculation is based on entry number 2 in Table VI-1. (VI-12b) The triangles are from Fan et al. (1968). The calculated spectra are again for entry number 2 in Table VI-1. (VI-12c) The open squares are from Lezniak and Webber (1971). The calculated spectra are for entry number 4 in Table VI-1. (VI-12d) The triangles are from Mason (1972). The calculation is based on entry number 5 in Table VI-1. (VI-12e) The calculated spectra are for entry number 8 in Table VI-1.
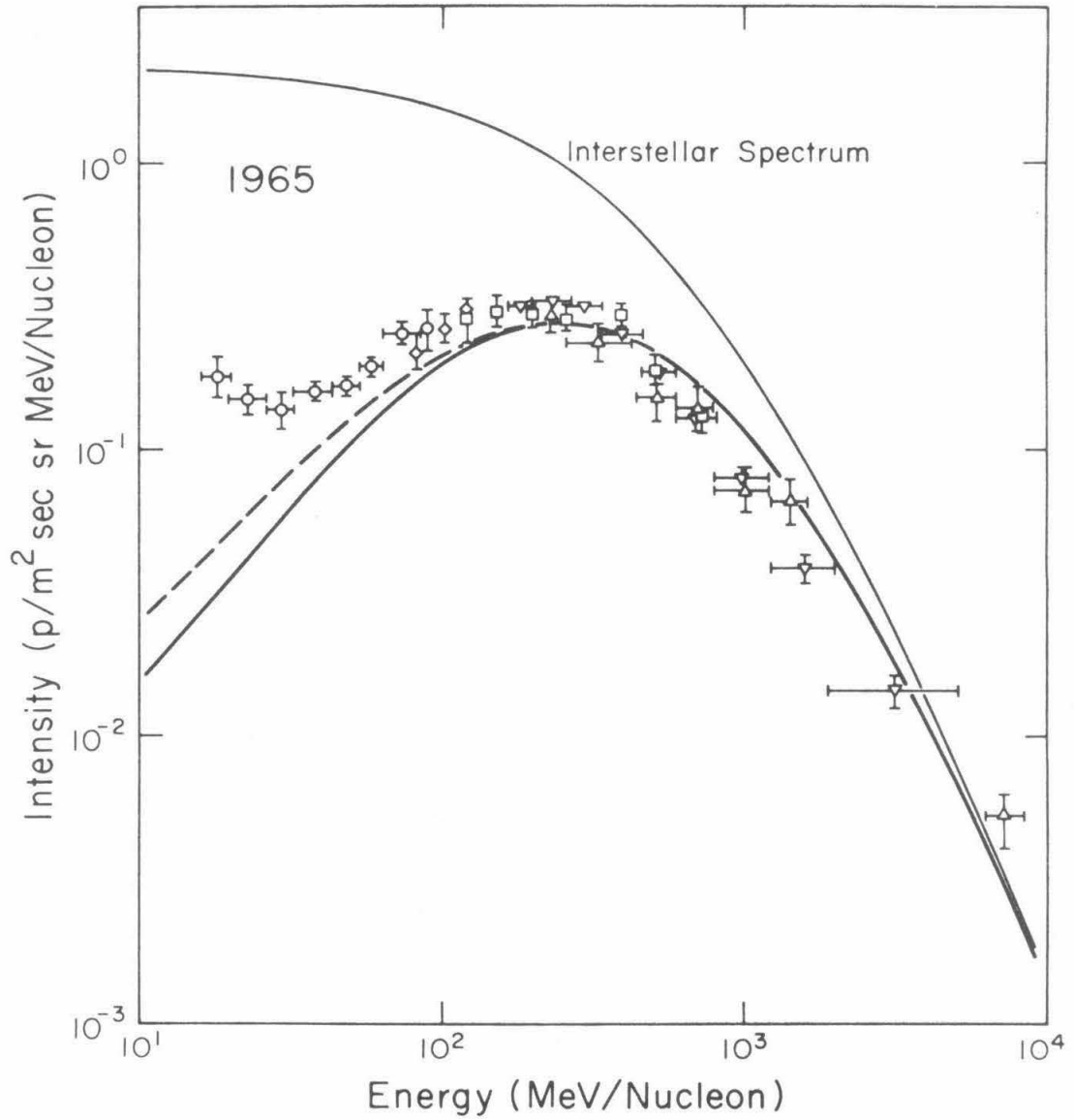
Figure **VI**-12a
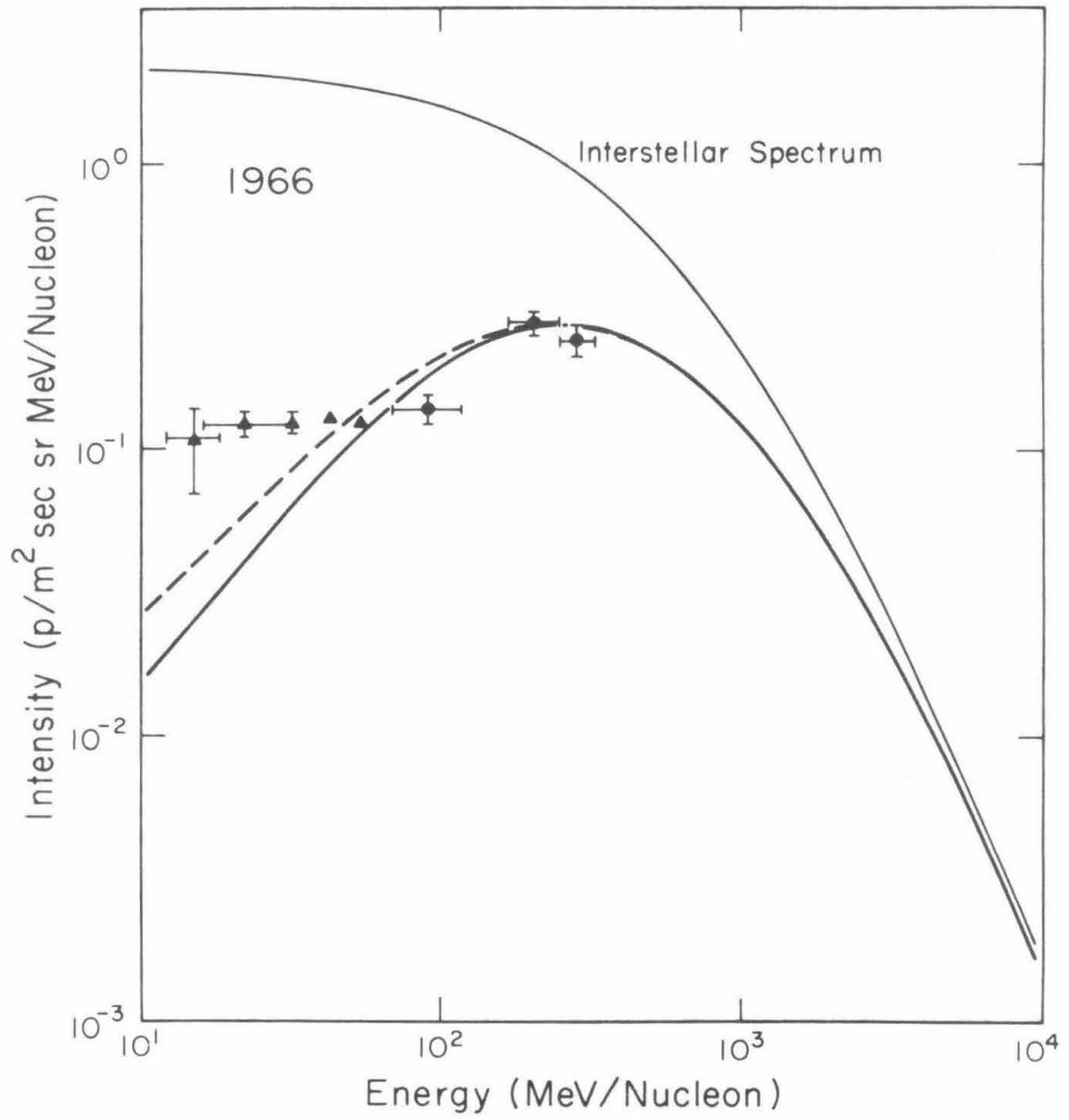
Figure VI-12b
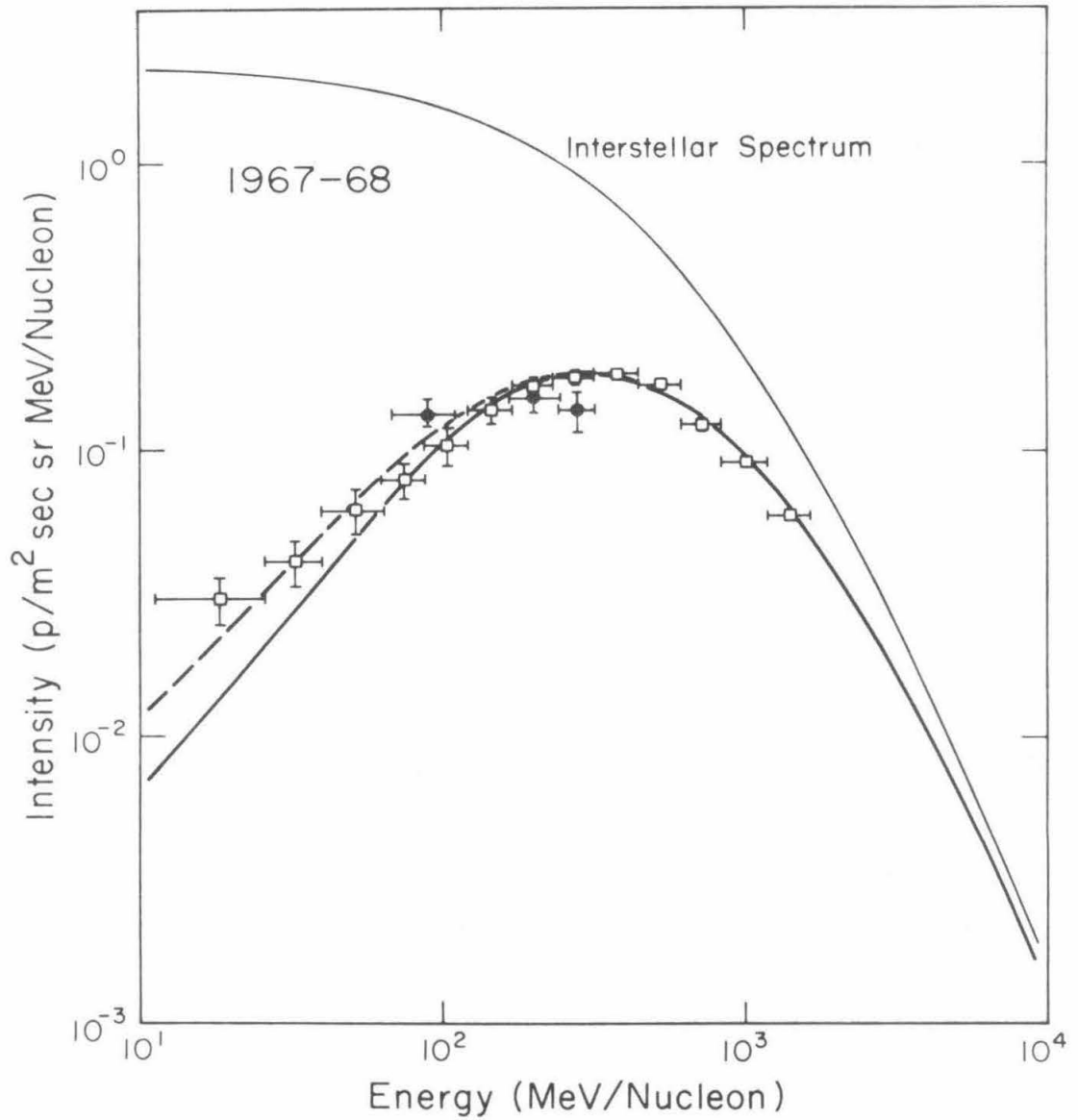
Figure VI-12c
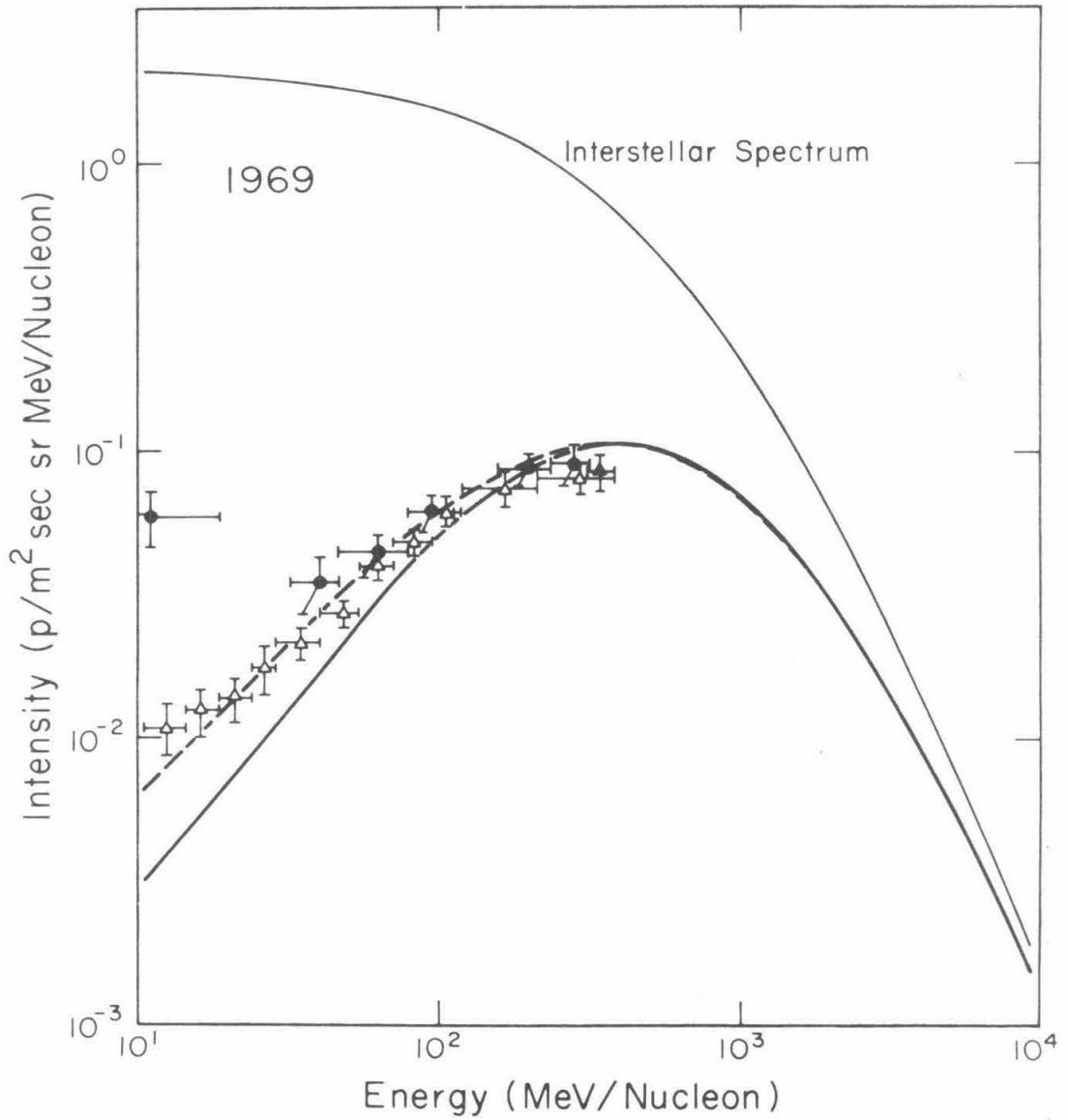
Figure VI-12d
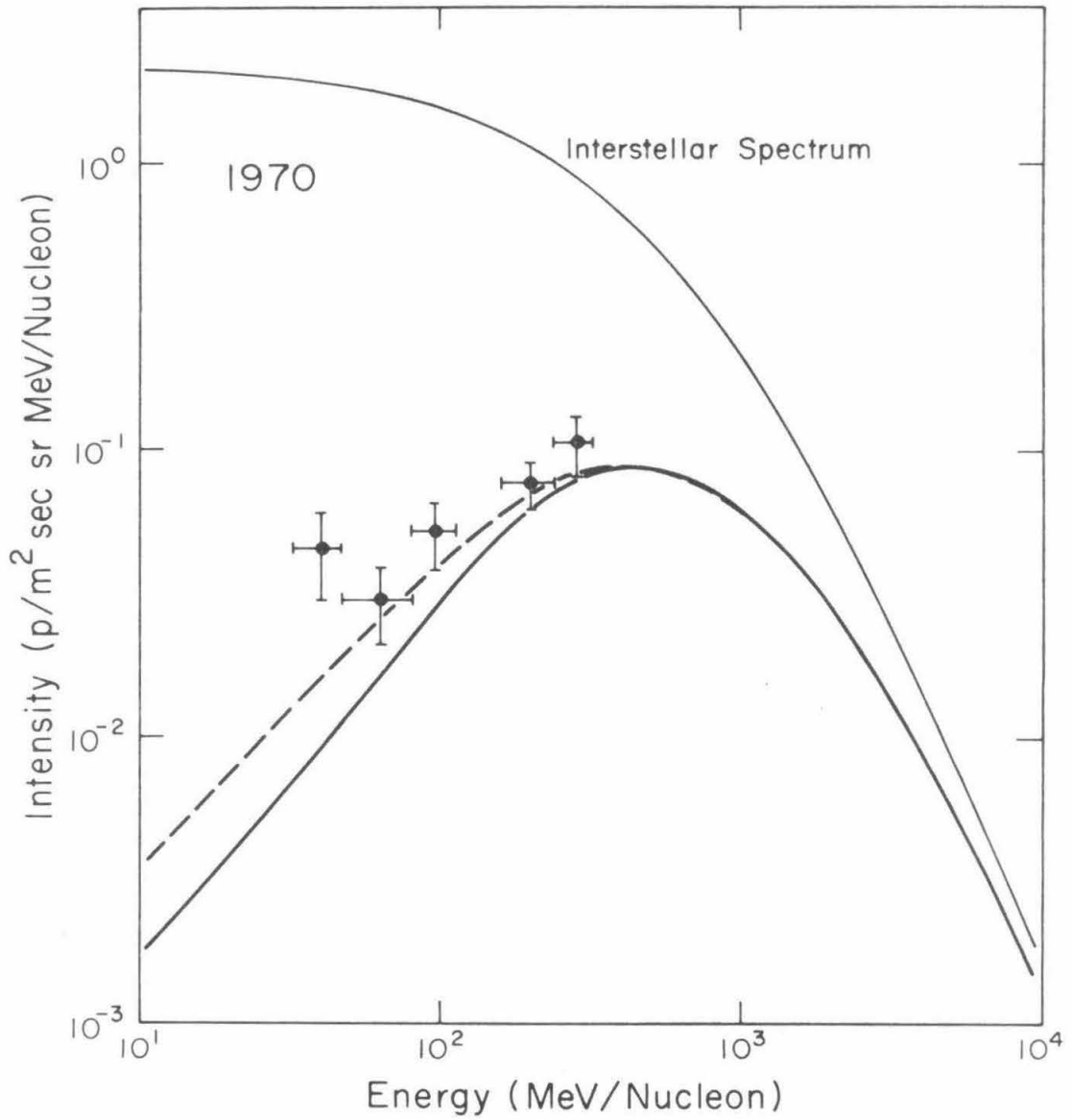
Figure VI-12e

Figure VI-13: Calculated and measured spectra of protons (a) and He nuclei (b) for 1965. Same as Figures VI-11a and VI-12a except that entry number 1 from Table VI-1 has been used for the calculation.
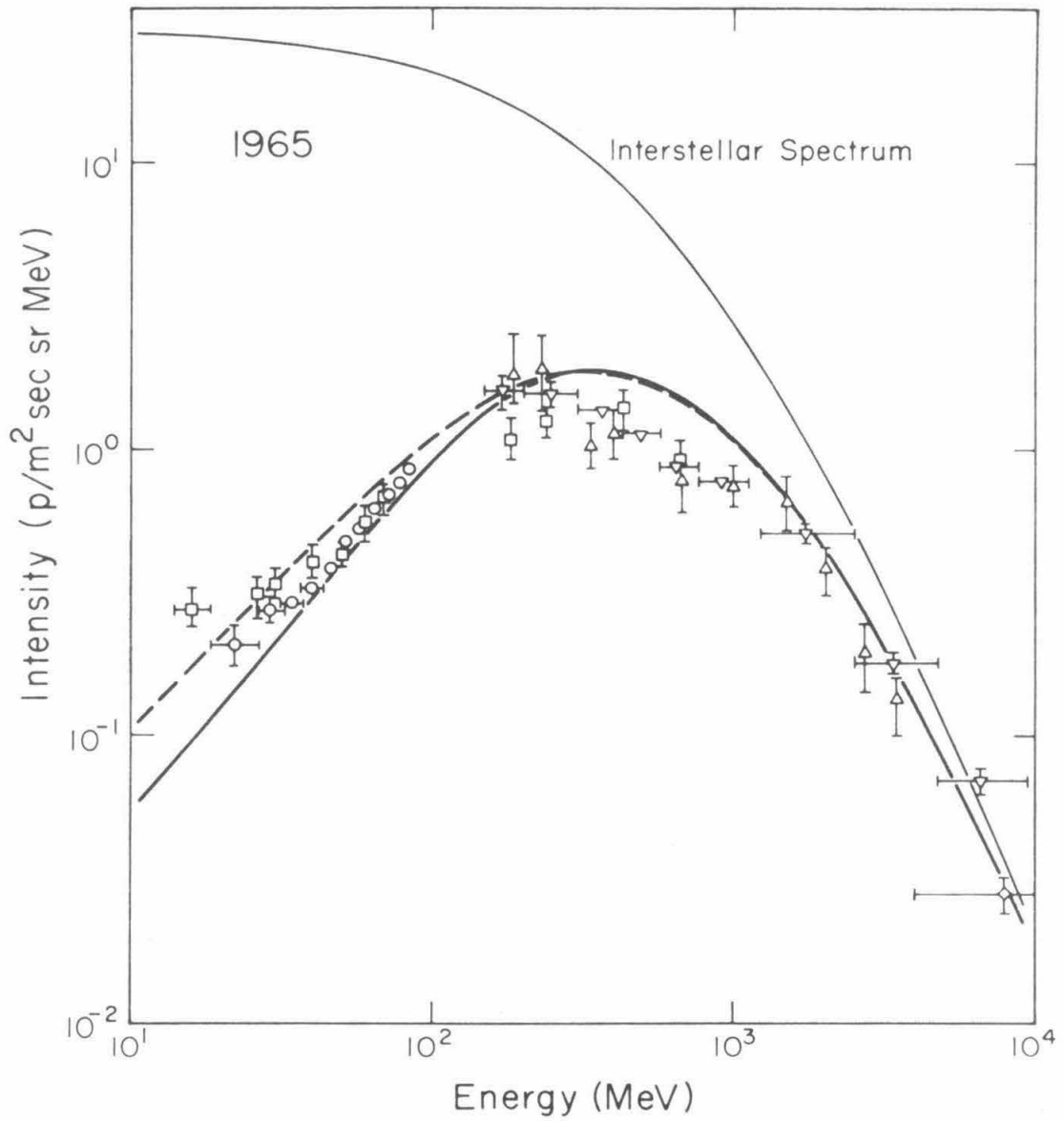
Figure VI-13a
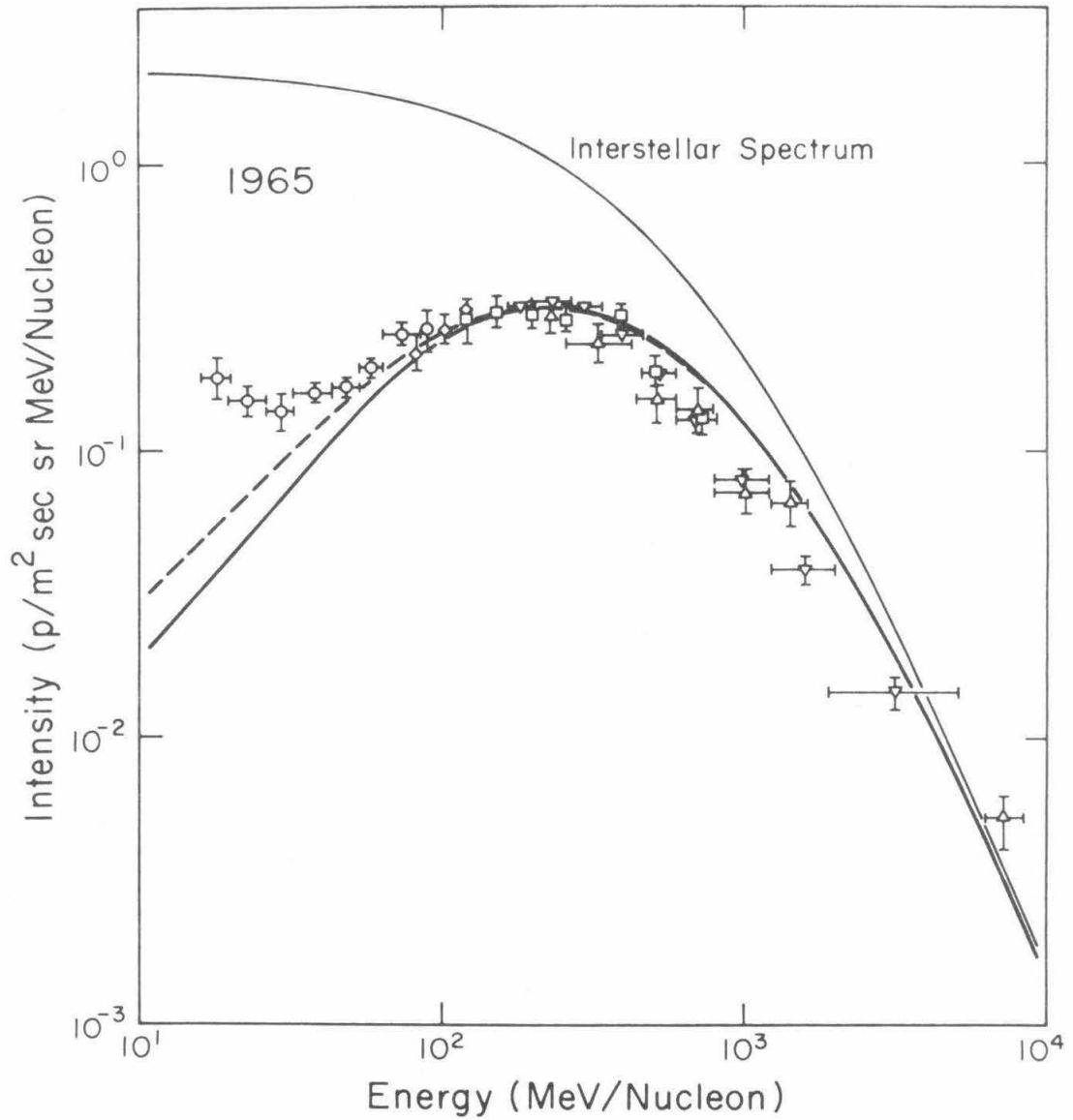
Figure VI-13b
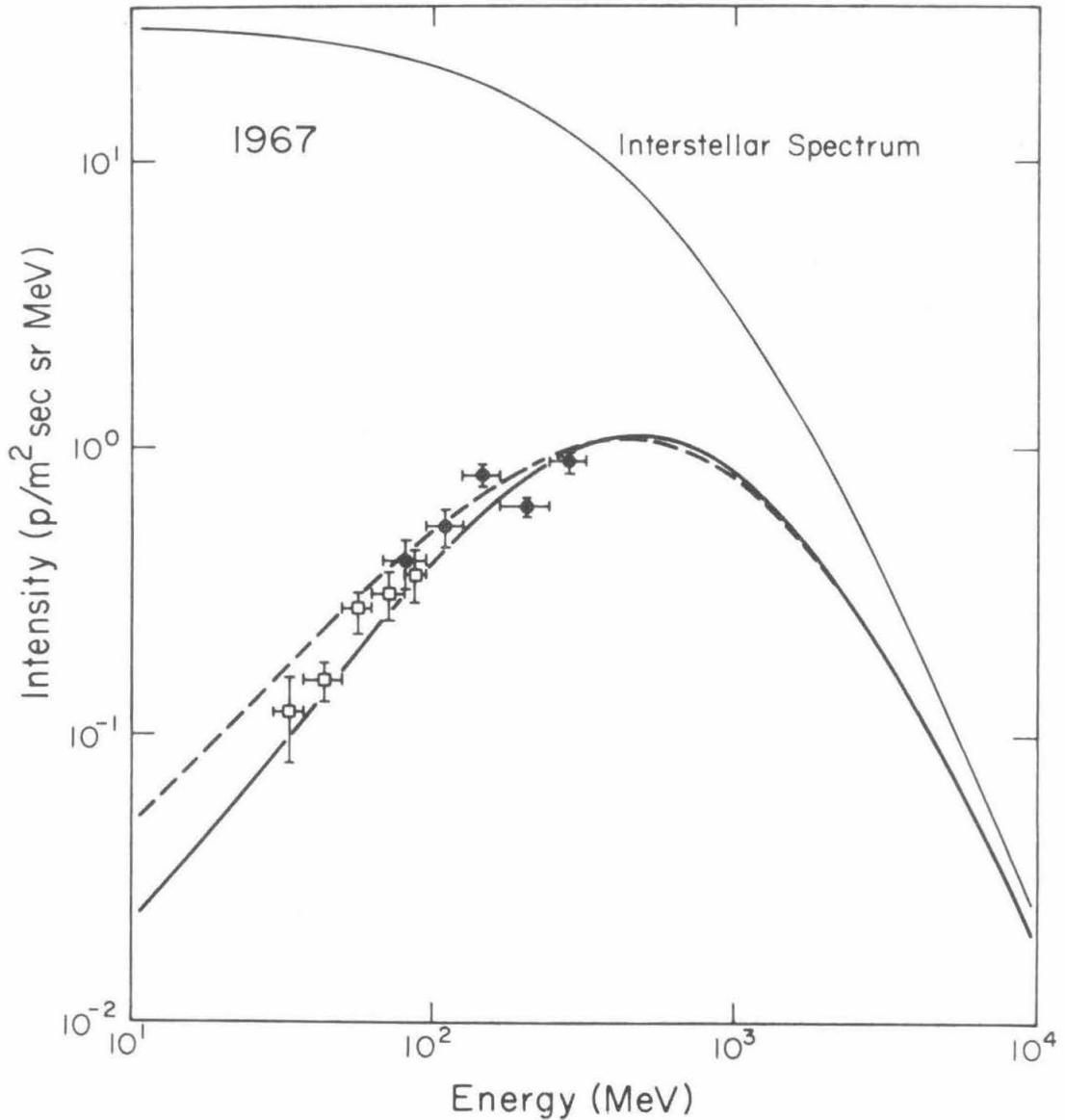
Figure VI-14

Calculated and measured proton spectra for 1967. Same as Figure VI-11c except that entry number 3 from Table VI-1 has been used for the calculation.

Figure VI-15: Calculated and measured proton spectra for 1969. The calculated spectra are intermediate to those presented in Figure VI-11 for 1969 and 1970 and assume a boundary distance of 9.5 A.U. The numbers 6 and 7 associated with the curve refer to the entry numbers in Table VI-1. The squares represent the difference between the measured spectrum and the upper calculated spectrum (labeled number 6). The power-law curve drawn through the low-energy points is intended to emphasize the fact that the spectrum flattens at about 10 MeV.
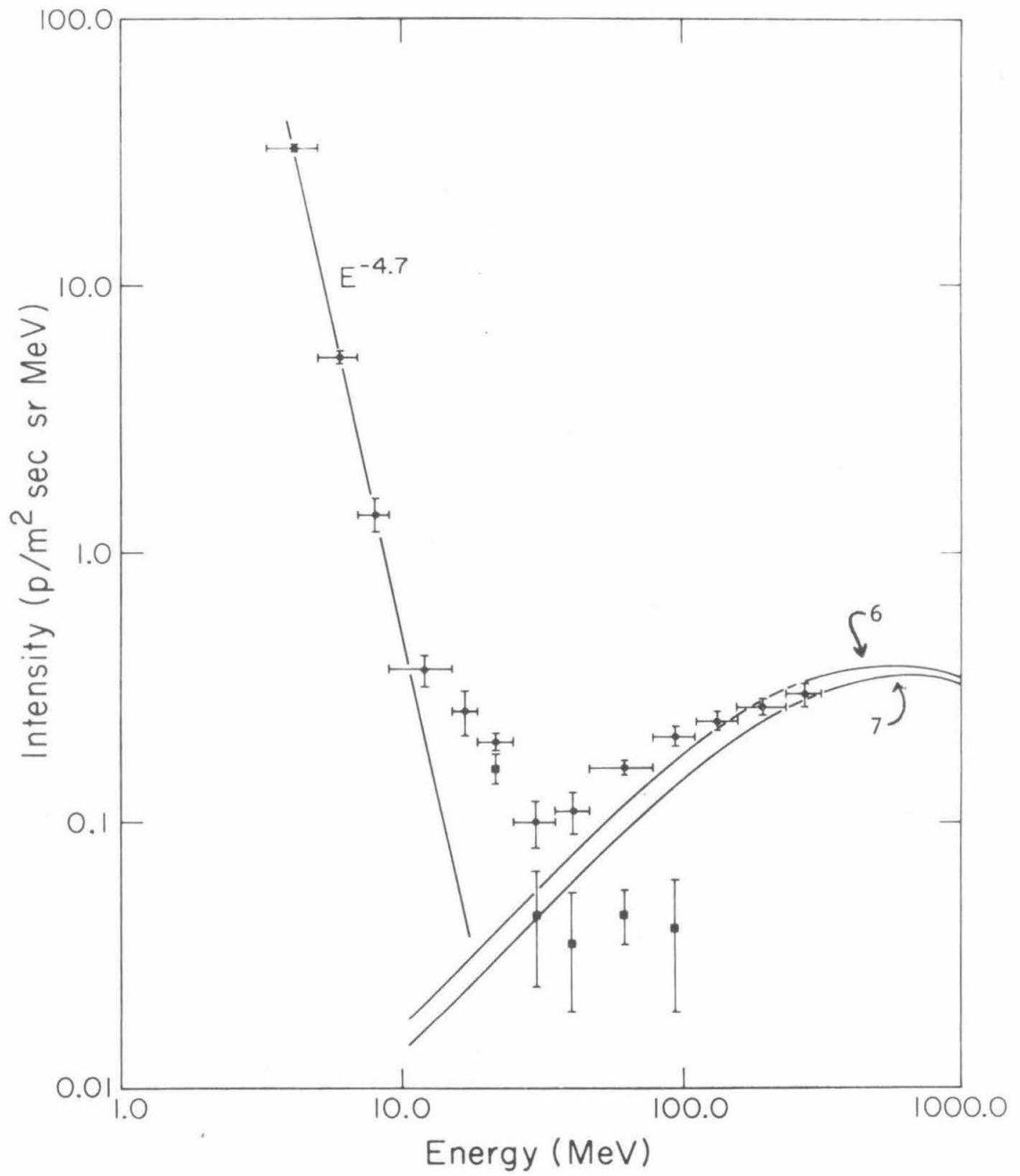
Figure VI-15
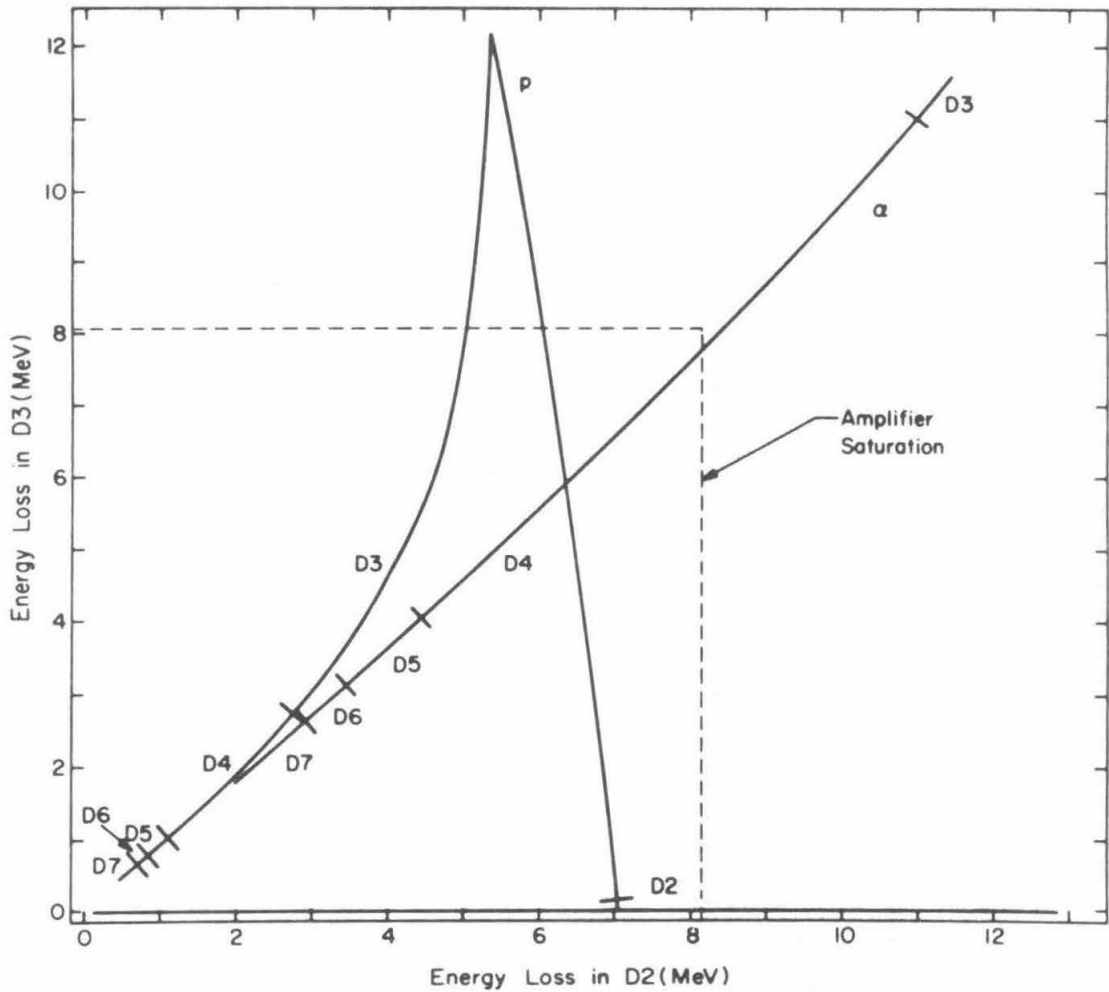
Figure A1-1

Average energy loss in D2 versus average energy loss in D3 for protons and alpha particles. The deepest detector penetrated is marked along the curve.

Figure A1-2: Number of events with specified energy loss in D2 and D3 for 21 days of OGO-6 data. The channel numbers have been pseudo-logarithmically compressed for plotting purposes. The line segments inside the bins correspond to the segments in Figure A1-1 which are marked "D5" as explained in the text. The bins are calculated to contain about 90% of the stopping particles and about 50% of the interacting particles. The excess of events with channel numbers less than about 6 is due to electrons.
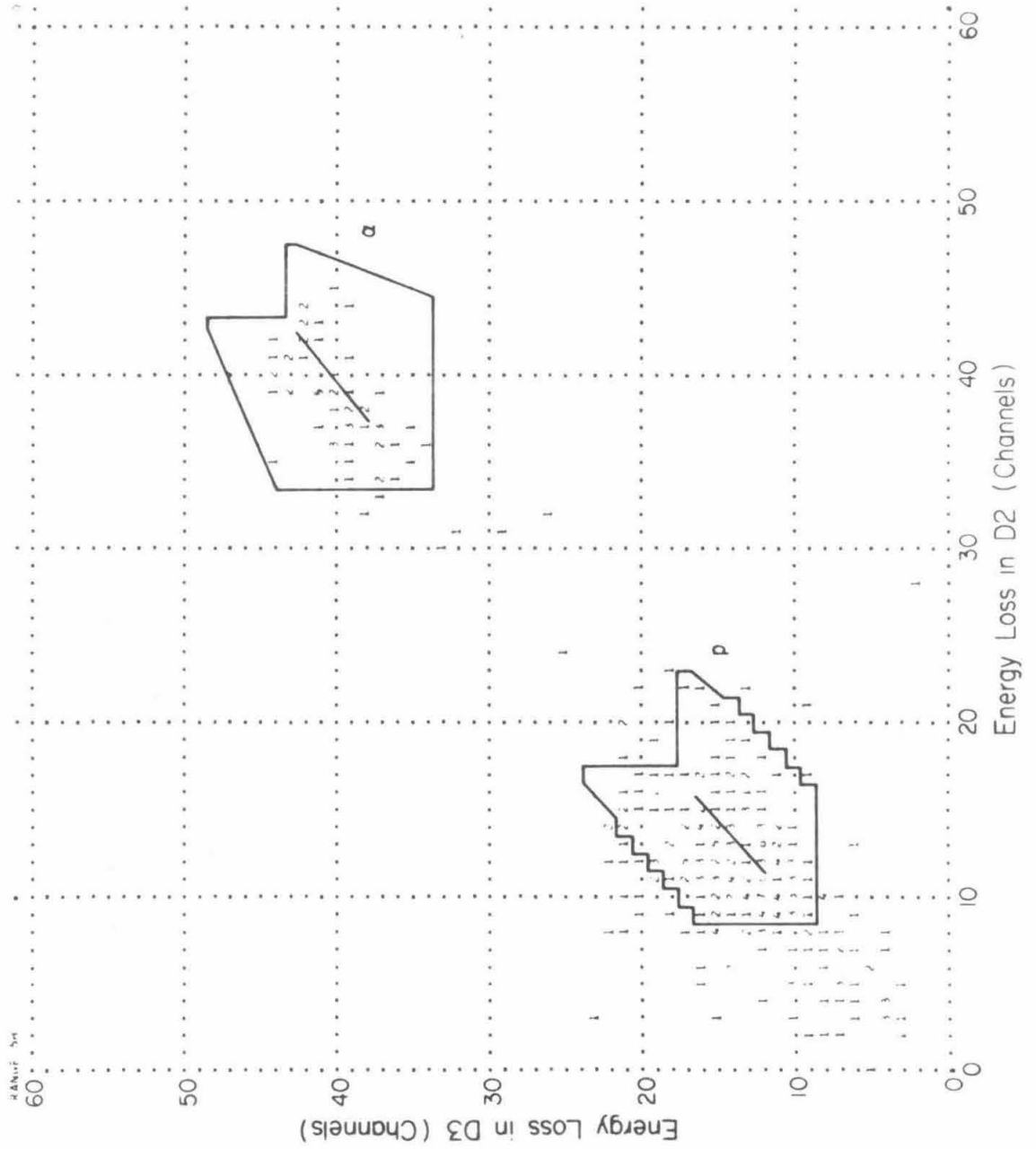
Figure A1-2
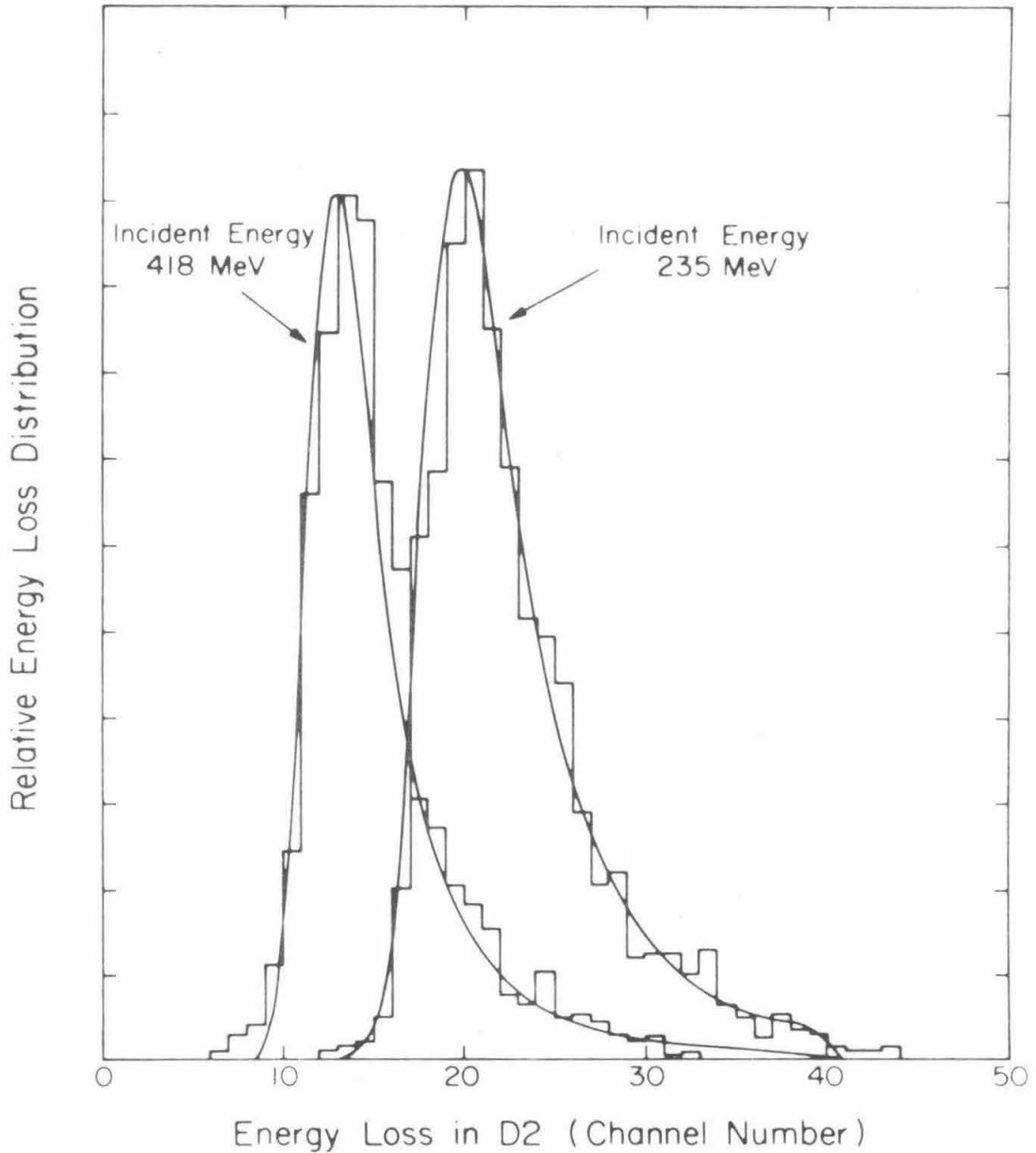
Figure A1-3

Two examples of calculated (smooth curve) and measured (histogram) energy loss distributions in pαe detector D2 for a monoenergetic proton beam of the indicated energy. The curves are normalized to peak height rather than area.

Figure A1-4: Calculated (smooth curves) and measured (histogram) diagonal channel distributions. The dashed curve is the calculated distribution of stopping protons, the dotted curve is for interacting protons, and the solid curve is their sum. The areas are normalized. The measured data are from flights 67C1P and 67C3P. The minimum or diagonal channel convention is discussed in the text.

p α e R5 Events

Percent of Events in Minimum D2D3 Channel

Minimum D2D3 Channel

Figure A1-4

201
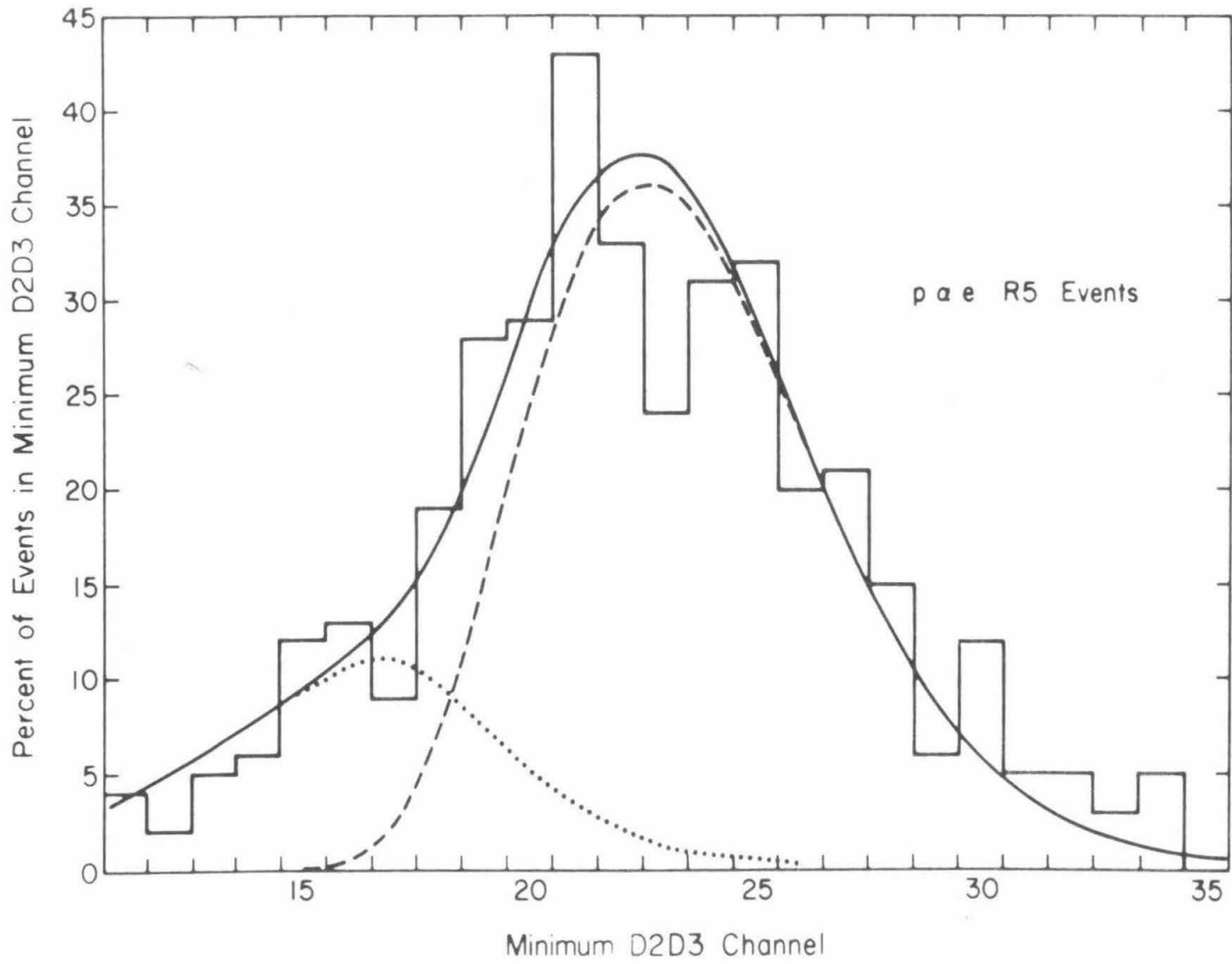
Figure A1-5

Schematic illustration of some types of nuclear-interaction events considered in making corrections to the data. These events are discussed in the text.
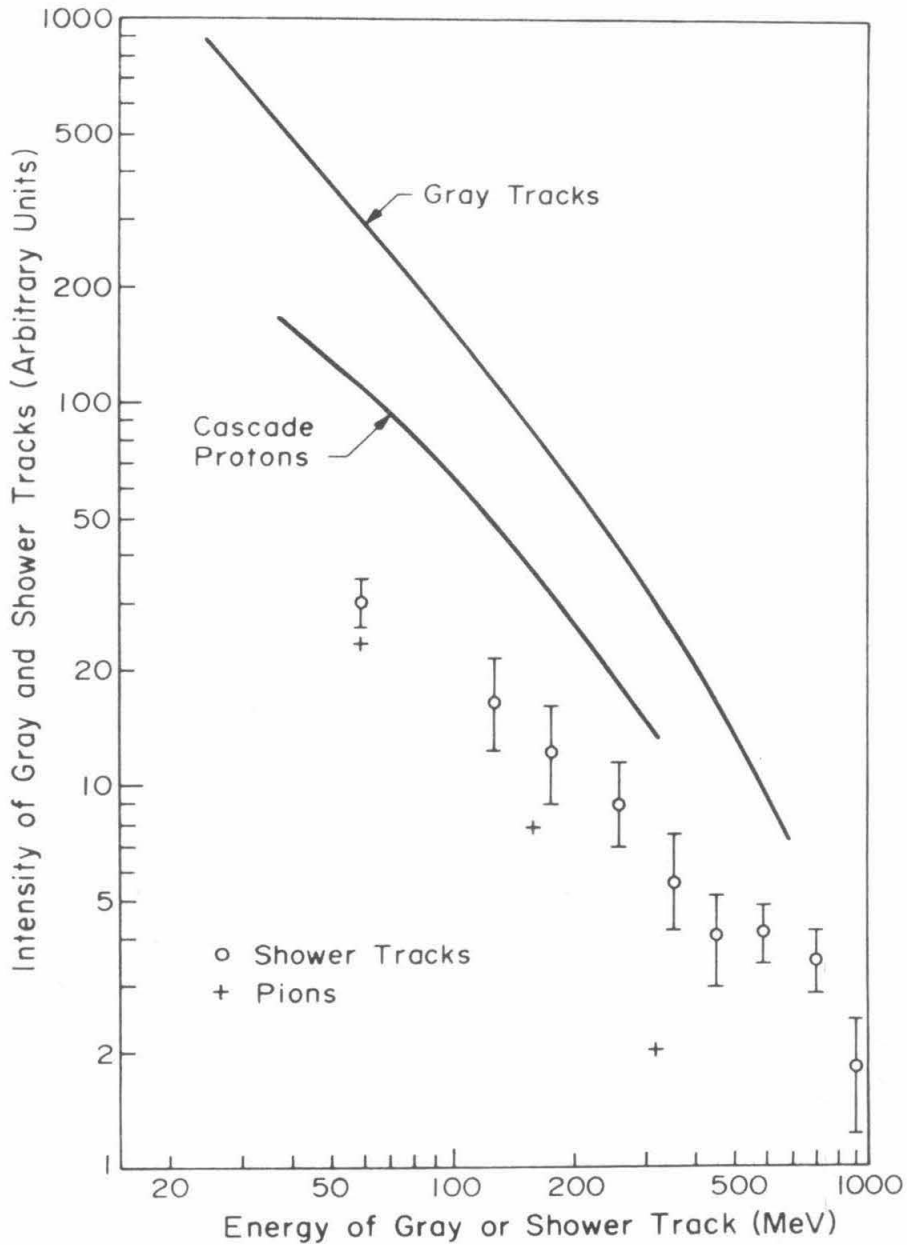
Figure A1-6

Spectra of gray and shower tracks. The smooth curve labeled "Gray Tracks" is the spectrum of gray tracks measured in emulsions exposed to cosmic rays by Camerini et al. (1950). The "Cascade Protons" as calculated by Metroplis et al. (1958b) should be comparable. The Cascade proton curve was calculated for the reaction $p + U^{238} \rightarrow p +$ (other particles) at 460 MeV. The open circles represent the emulsion data for shower tracks (Camerini et al., 1950) and the crosses represent the calculated spectrum of pions from the reaction $p + Pb^{207} \rightarrow \pi +$ (other particles) at 750 MeV. (Bertini, 1967).

Figure A1-7: Calculated (curves) and measured (points) probability
that a proton will stop in a given range with and without triggering
D8. The statistical error in the points is given by the size of the
point and the statistical error in the curves is typically slightly
larger.

Figure A1-7

204
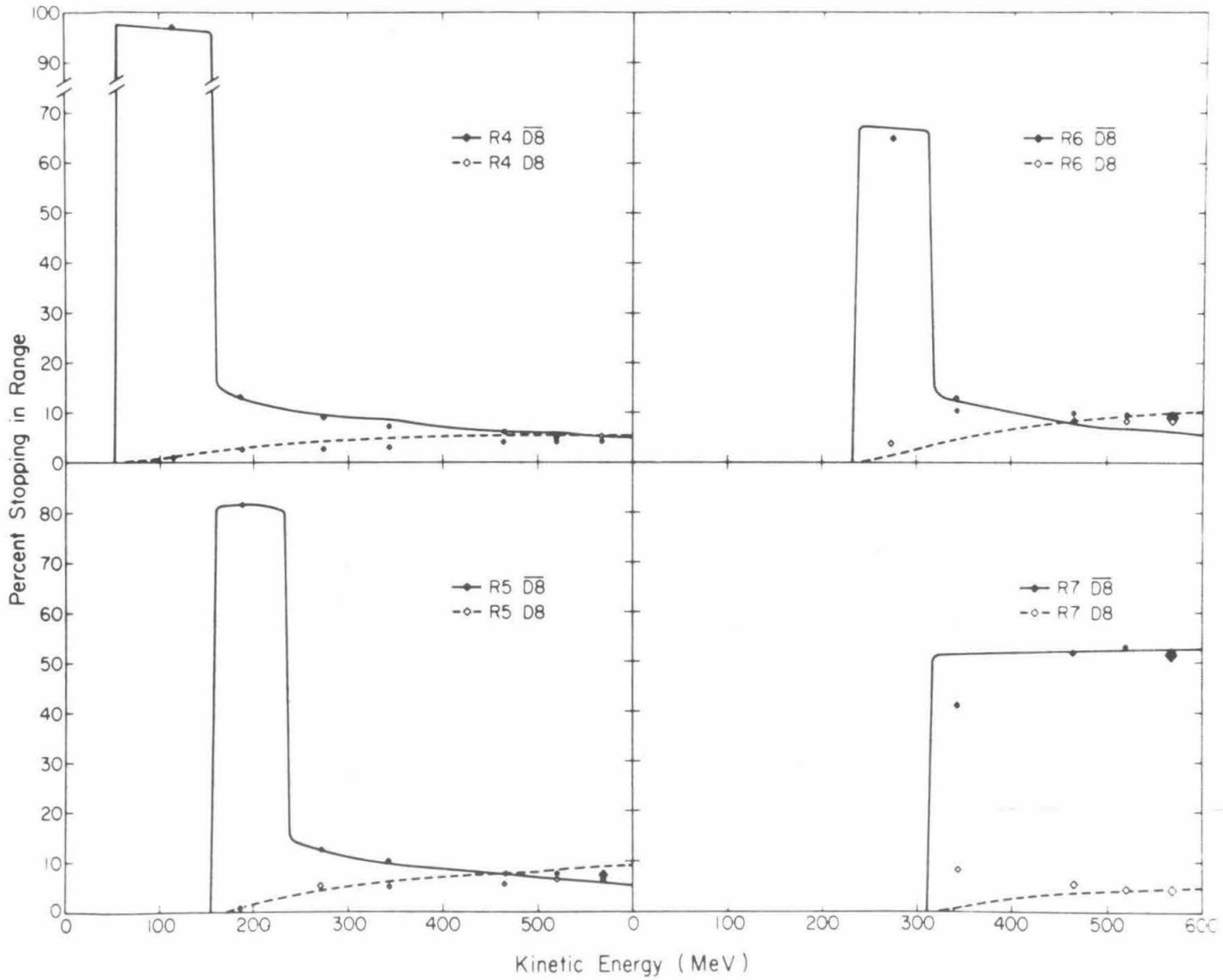
Figure A1-8: Same as Figure A1-7 but for alpha particles. Note that these curves have tails both below and above the peak because of the "straight-on particles."

Figure A1-8

207
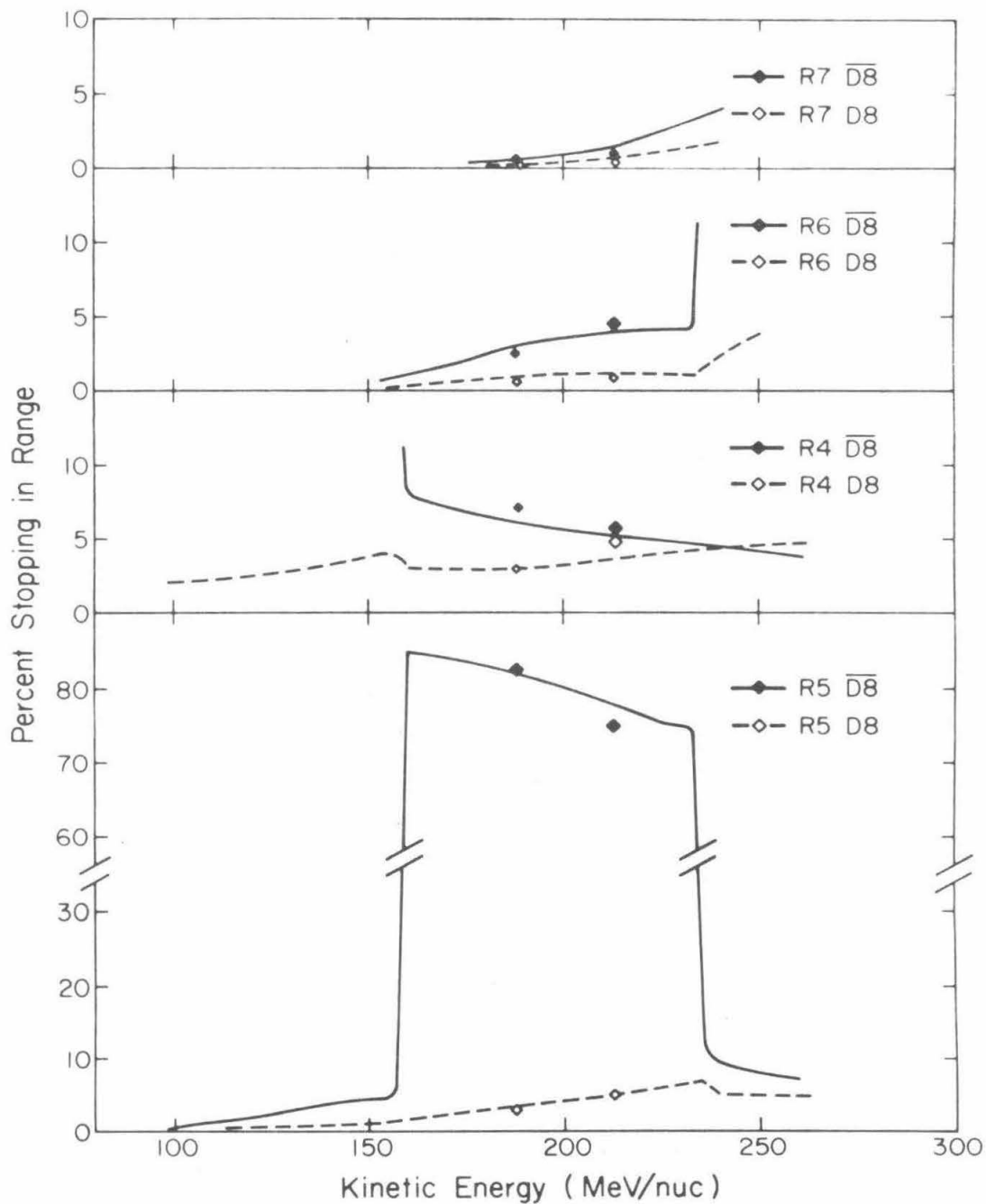
Figure A1-9: Schematic of the accelerator version of the range tele-
scope.   The D8 anticoincidence "cup" is enlarged and separated into
two pieces to allow space for the light pipes, but it still subtends
the same angles.
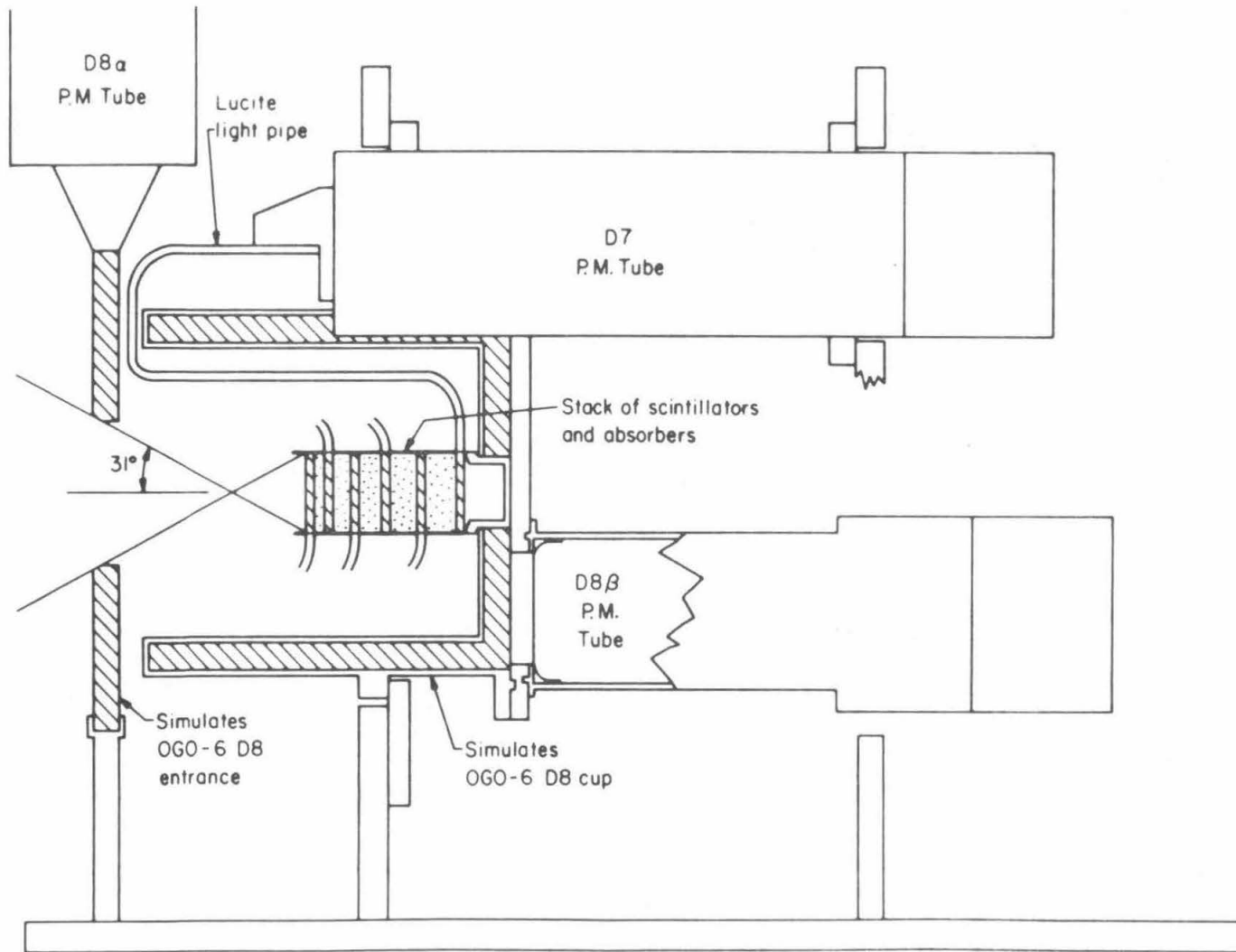
Figure A1-9

Figure A1-10: Schematic illustration of the beam layout for the accel-
erator calibrations and the electronic logic and data recording system.
Details are given in the text.

Figure Al-10

211
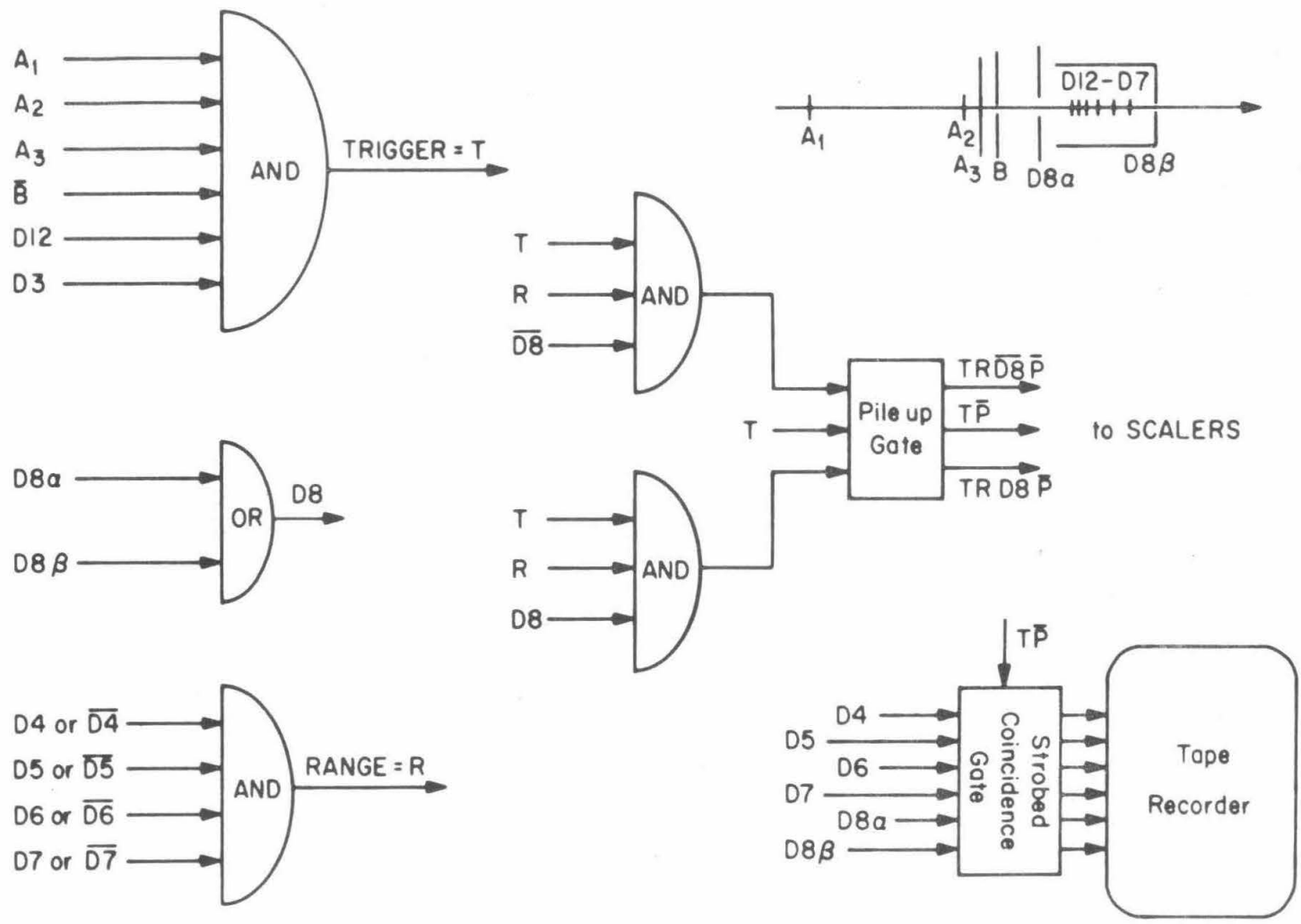
Figure A2-1: Schematic of model atmosphere and interactions. Solid lines are charged particles, dotted lines are neutrons. The circled numbers indicate the "order" of the particle -- primary, secondary, etc. Note that the α particle has a straight-on secondary.
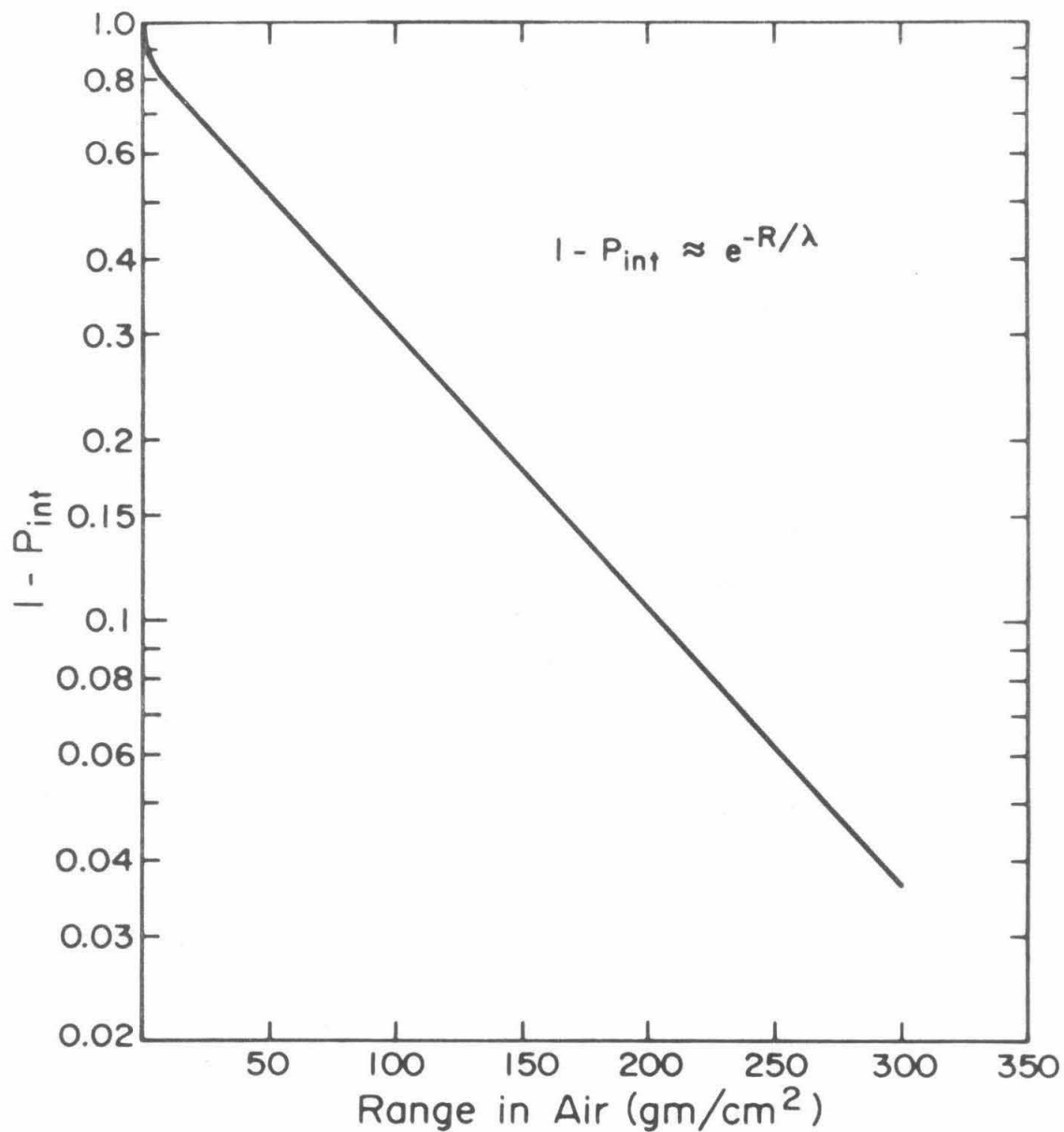
212
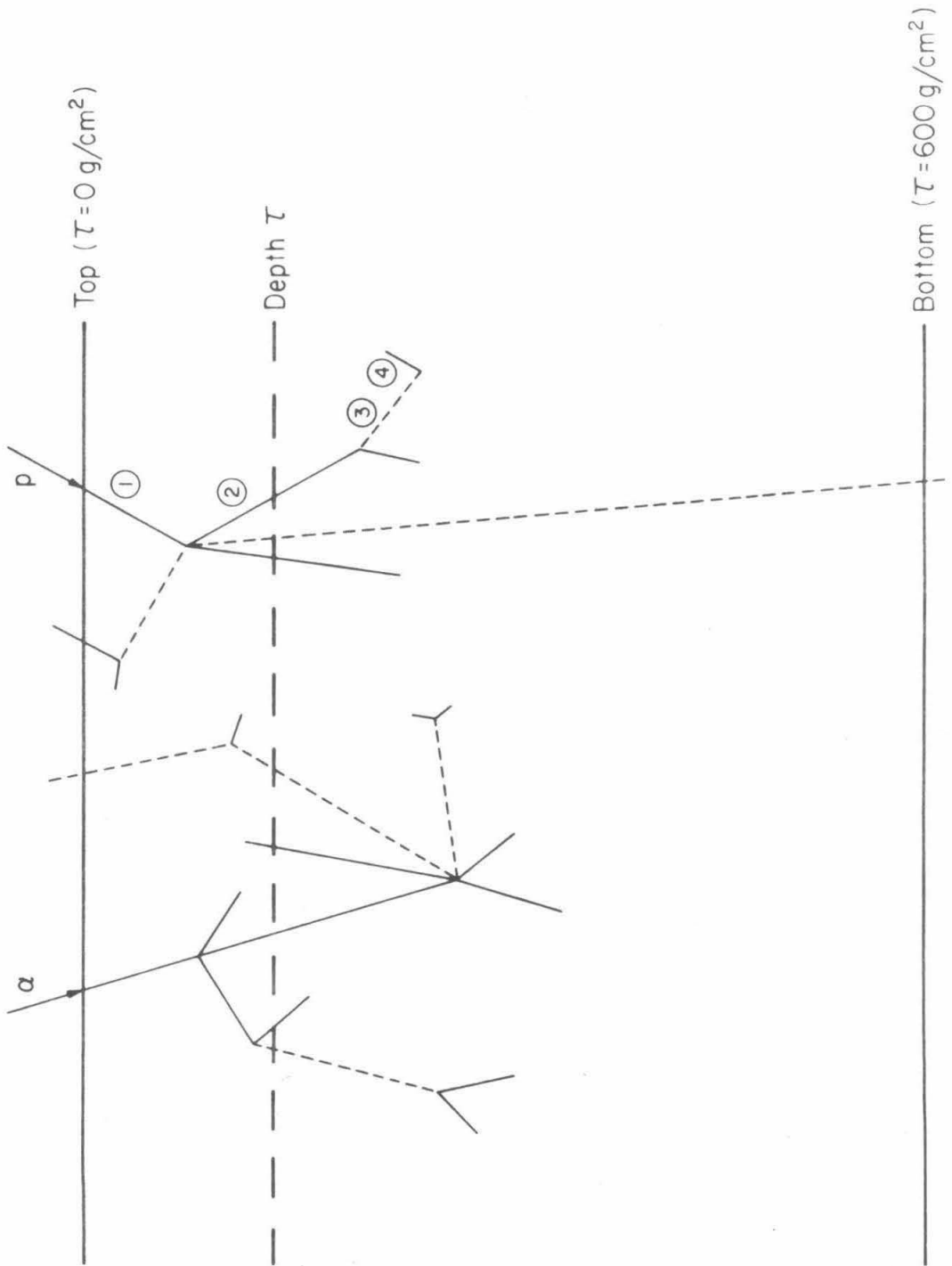
Figure A2-1

Figure A2-2

The quantity $1 - P_{int}(E_o)$ is plotted versus range (at E_o) for protons. Both quantities are from Janni (1964).

Figure A2-3: Secondary proton multiplicities determined by several
investigators for various materials. The heavy curve (Bertini, 1966;
1967) is for O^{16}, all the others are for heavy elements. There is
clearly an important difference. The curves labeled n_g and $n_g + n_s$
are multiplicities of gray tracks and gray + shower tracks in emulsions
(Powell et al., 1969). The curves with points are after Metropolis et
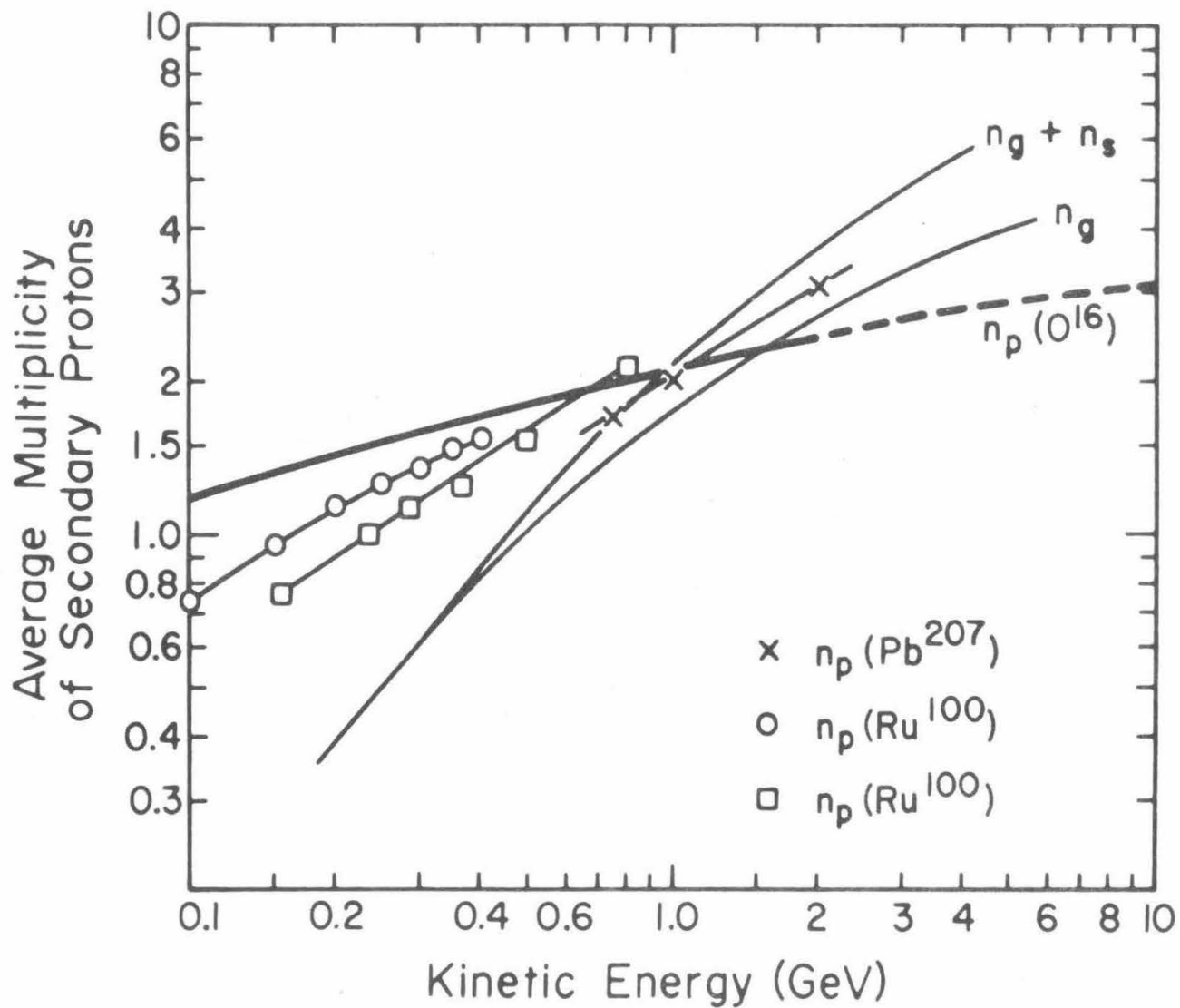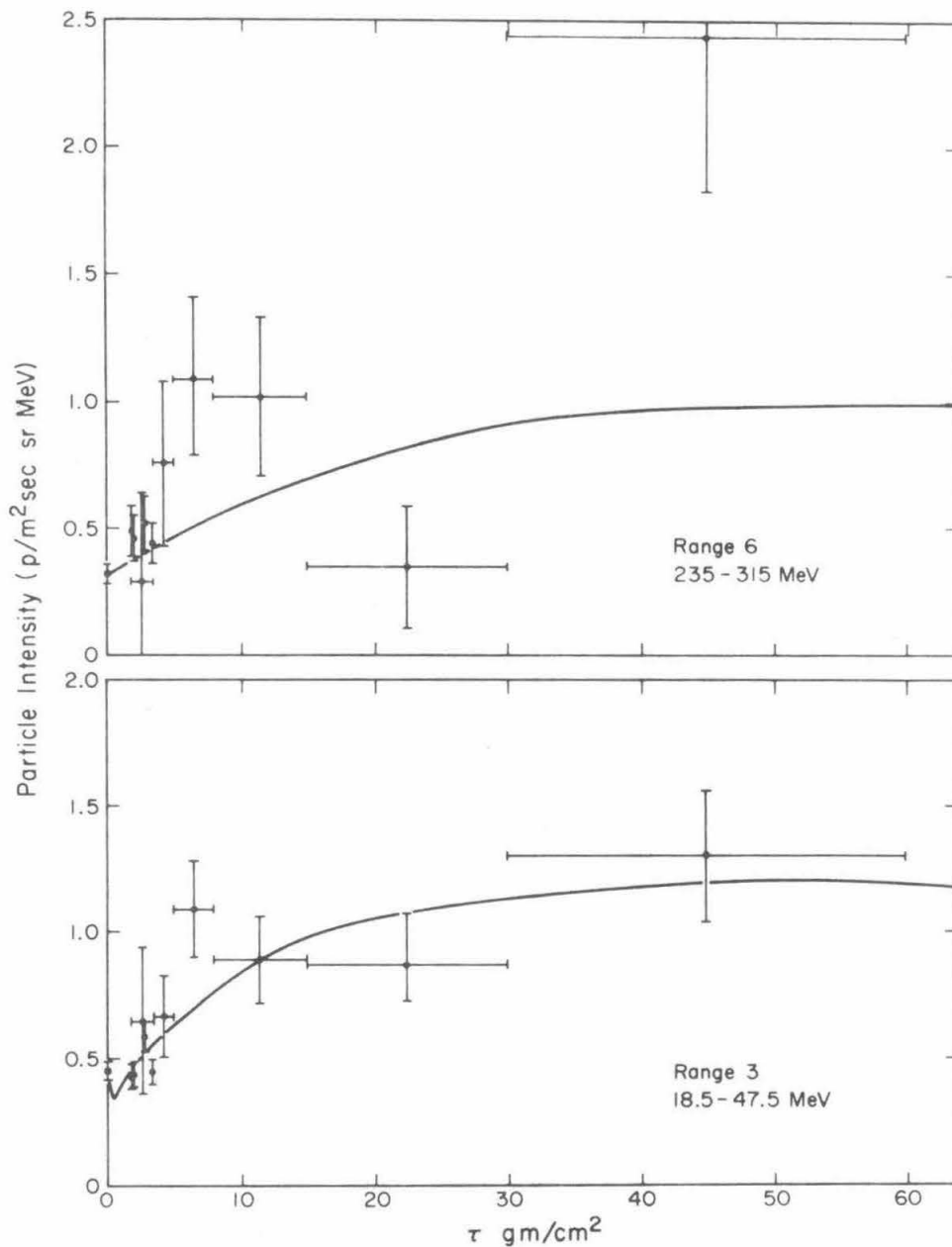al. (1958a; b) (Ru) and Bertini (1967) (Pb).

Figure A2-3

Figure A2-4

Proton intensity is plotted as a function of pressure altitude in the atmosphere. The curves are calculated. The points were measured simultaneously with the pαe and OGO-6 systems in 1969.
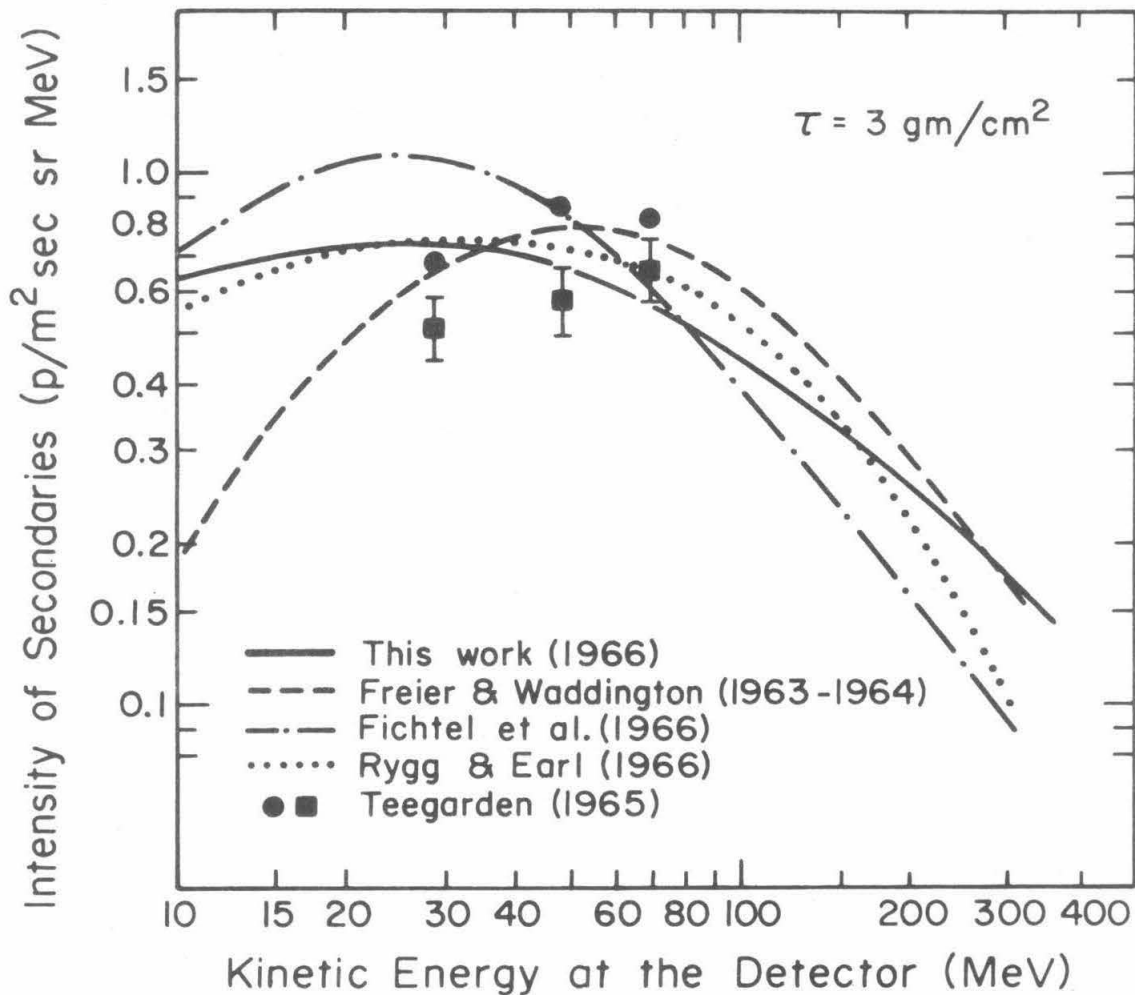
Figure A2-5

Intensity of secondaries at an altitude of 3 gm/cm^2 as determined by
several investigators. --- (Freier and Waddington, 1968), ... (Rygg
and Earl, 1971), ■ protons, ● protons + deuterons, (Teegarden, 1967a),
-·-See text.